UNIVERSITY OF PRETORIA

UNIVERSITEIT VAN PRETORIA
UNIVERSITY OF PRETORIA
YUNIBESITHI YA PRETORIA

DOCTORAL THESIS

Local spectroscopic properties of certain plasmonic and plexcitonic systems

Author:
LUKE C. UGWUOKE

Supervisors:
PROF. TJAART KRÜGER
PROF. TOMÁŠ MANČAL

A thesis submitted in partial fulfilment of the requirements
for the degree of Doctor of Philosophy
in the

Faculty of Natural and Agricultural Sciences
Department of Physics

December 6th, 2020

DECLARATION

I, Luke C. Ugwuoke declare that the thesis, which I hereby submit for the degree of Doctor of Philosophy (PhD) in Physics at the University of Pretoria, is my own work and has not previously been submitted by me for a degree at this or any other tertiary institution.

Parts of this thesis have been published as:

L. C. Ugwuoke, T. Mančal, and T. P. J. Krüger, *Localized surface plasmon resonances of simple tunable plasmonic nanostructures*, Plasmonics, 15: 189 – 200 (2020),

L. C. Ugwuoke, T. Mančal, and T. P. J. Krüger, *Plasmonic quantum yield enhancement of a single molecule near a nanoegg*, J. Appl. Phys., 127: 203103 (2020), (**Editor's Pick**),

L. C. Ugwuoke, T. Mančal, and T. P. J. Krüger, *Optical properties of a nanoegg-nanorod heterodimer: a quasi-static analysis*, J. Opt. Soc. Am. B, 37: A293 – A303, 2020,

and presented as:

L. C. Ugwuoke, T. Mančal, and T. P. J. Krüger, *Mode-Mixing in nanoeggs*, 64th SAIP Conference, 2019, Track G: Theoretical and Computational Physics, (Oral presentation)

L. C. Ugwuoke, F. Kyeyune, T. Mančal, and T. P. J. Krüger, *Fluorescence enhancement of a single light-harvesting complex near a gold nanorod: theory and experiment*, 25th International Workshop on Single Molecule Spectroscopy and Super-Resolution Microscopy in the Life Sciences, 2019. (Poster presentation)

Signed:————————————————————————————-

Date:————————————————————————————-

ABSTRACT

In the framework of the quasi-static approximation (QSA), some theoretical studies were conducted within the local response approximation (LRA). In these studies, certain plasmonic and plexcitonic systems were proposed, and their spectroscopic properties investigated. The QSA allows us to study metal nanoparticles (MNPs) and inter-particle distances that are small compared to the wavelength of light in the medium surrounding the MNPs, while the LRA enables us to utilize the bulk dielectric response of the metal in consideration. We have studied the following properties in detail: localized surface plasmon resonances (LSPRs), plasmon-induced transparency (PIT), and plasmon-enhanced fluorescence (PEF), while exciton-induced transparency (EIT) has only been partly studied. LSPR and PIT are properties of plasmonic systems while PEF and EIT are properties of plexcitonic systems. Both PIT and EIT are forms of electromagnetically-induced transparency.

We started by constructing a geometry-based theoretical model that predicts the LSPR formula of any member of a certain group of single MNPs, using the LSPR for the most complex MNP geometry in the group. The model shows that from the LSPR of a nanorice, one could predict the LSPRs of concentric nanoshells, solid and cavity nanorods and nanodisks, respectively, and solid and cavity nanospheres. These formulae serve as quick references for predicting LSPRs since they can easily be compared to LSPRs obtained from spectral analysis. Likewise, we studied LSPR in addition to PIT in a nanoegg-nanorod dimer. We proposed this dimer in order to investigate how the interplay between plasmon coupling and MNP sizes affects PIT in complex geometries such as nanoeggs. Our result shows that the formation of PIT dips — regions in the dimer spectra where little or no incident radiation is absorbed by the dimer — are strongly-dependent on the nanorod size, due to the dependence of the plasmon coupling strength on the half-length of the nanorod.

We investigated the phenomenon of PEF using a nanoegg-emitter system and a nanorod-emitter system, respectively. Emitters are organic or inorganic materials whose radiative decay rates increase dramatically when placed near a MNP subjected to plasmon excitation. Our theoretical results show that the choice of the MNP-emitter system to use depends on both the intrinsic quantum yield of the emitter and the antenna efficiency of the MNP. Theory shows that PEF is more substantial when the former is very low, and it will always occur if the latter is greater than the former. A nanorod-emitter system should serve as the preferred choice, due to the relatively easier synthesis of nanorods compared to nanoeggs, and the large longitudinal polarizability of nanorods as a result of the *lightning rod effect*. However, our theoretical model also shows that a nanoegg-emitter system can rival the PEF parameters obtained in a nanorod-emitter system, due to an increase in the Purcell factor of the emitter with increasing core-offset of the nanoegg, resulting from the presence of *dipole-active modes* in the nanoegg.

ACKNOWLEDGEMENT

I will start by thanking my supervisor, Prof. Tjaart Krüger, who not only accepted me to work in his Biophysics and Photonics research group, at the Department of Physics, University of Pretoria, but also assisted me in applying for funding opportunities which were paramount to the success of my research projects and my general well-being during my studies.

I am grateful for the research visit I underwent at the Faculty of Mathematics and Physics, Charles University, Prague, Czech Republic, which was organised by my co-supervisor, Prof. Tomáš Mančal. The visit introduced me to the various theoretical methods used in the quantum description of the spectroscopy of molecular systems, for which I realized that I still have so much to learn in that area.

I am grateful to both by supervisors for editing my research proposals, posters, presentation slides, manuscripts, and my thesis, and offering numerous suggestions on the theoretical models in my research projects. These were very helpful, especially on how they contributed to the positive reviews I received from accepted manuscripts.

I thank both the National Research Foundation (NRF) and University of Pretoria, for their financial assistance throughout the period of my studies. I am also grateful to Prof. Mark Tame, who is currently assisting me (during a research visit at Stellenbosch University, by the time of finishing this thesis) to learn how to do electrodynamic simulations in Comsol Multiphysics, via the RF and Wave Optics Modules.

Finally, I thank everyone at the Biophysics and Photonics research group, for their warm welcome when I joined the research group, and for assisting me in one way or another when I needed help academically or otherwise, throughout the period of the doctoral program.

CONTENTS

1

INTRODUCTION

1.1 OVERVIEW OF CLASSICAL PLASMONICS

Plasmonics can be described as the study of the spectroscopic properties of metal-dielectric nanostructures upon their interaction with electromagnetic radiation of certain wavelength.[1–3] Though such nanostructures usually contain noble metals,[1,4] plasmonic behaviour has also been reported in other transition metals and their oxides,[2] and in alkali metals.[3] Metal nanoparticles (MNPs) are known to support localized surface plasmons – collective oscillations of confined conduction electrons at the metal-dielectric interface, in the ultraviolet,[5] visible,[1,4] and near-infrared regions[1] of the electromagnetic spectrum. MNPs display size-dependent characteristic colours upon exposure to diffused light (Fig. 1.1(a)), due to excitation near their localized surface plasmon resonance (LSPR). The colour displayed is due to the scattered component of the visible light region. For a solution of gold nanospheres,[6] the colour undergoes a blueshift, i.e., from brick red to light blue (Fig. 1.1(a)), as the particle sizes increase from 20 nm to 60 nm in diameter. However, in asymmetric MNPs — such as nanodisks[7,8]

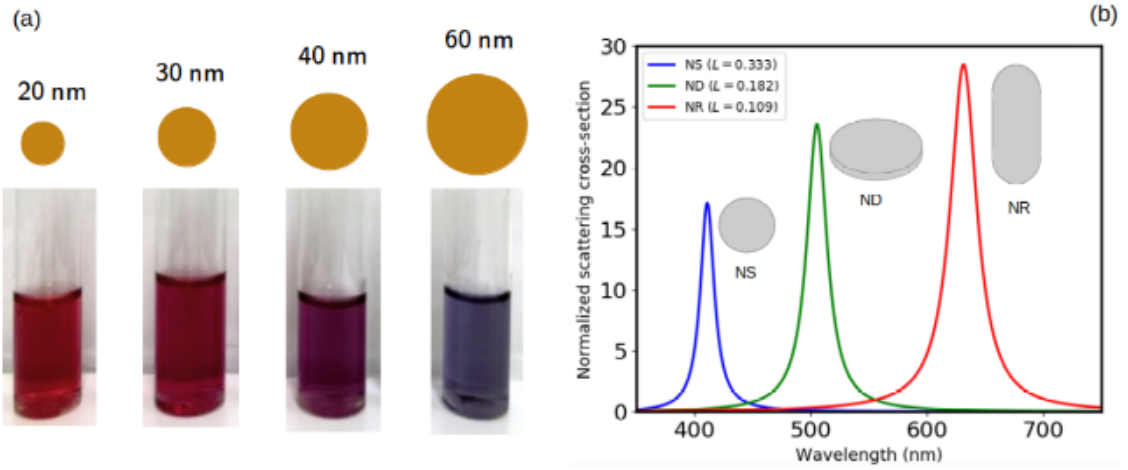

Figure 1.1: (a) Size-dependent characteristic colours of colloidal solutions of spherical gold nanoparticles. (Adapted from Ref.[6]) (b) Shape-dependent scattering cross-sections of single silver nanostructures of same volume: a nanosphere (NS), a nanodisk (ND), and a nanorod (NR) embedded in water, showing the positions of their dipolar LSPR. (Reproduced from Ref.[7])

(oblate spheroidal nanostructures), nanorods[9–12] (circular cylindrical nanostructures with two hemispherical caps on its opposite ends), nanoeggs[13–15] (core-shell nanostructures with off-centre dielectric or metallic cores), nanocups[15] (core-shell nanostructures with off-centre dielectric or metallic cores in contact with the host

medium), and nanocaps (core-shell nanostructures with incomplete dielectric or metallic shells),[16] and in dimers[17–19] and aggregates[20] — the polarization of the incident light affects their LSPR. As shown in Fig. 1.1(b), the spectral peak positions of the nanostructures, i.e., their LSPR, are shape-dependent. Their dependence on the polarization of the incident field will be discussed in Chapter 2. For single silver nanoparticles, their LSPR shifts from the blue to the red region of the visible light spectrum as the shape changes from a sphere to a rod. This is due to a decrease in the geometric factor, L, of the MNP, i.e., from $L = 0.333$ to $L = 0.109$, as shown in Fig. 1.1(b). The geometric factor, also known as shape factor,[7,21] is a dimensionless geometric parameter that arises from the shape-induced dipole field due to the response of the nanostructure to an incident field. This determines the particle's polarizability, i.e., the ease at which the surface charges are polarized upon excitation by light, and the corresponding spectral properties. For instance, in Fig. 1.1(b), the decrease in L is also responsible for the increase in the scattering cross-section. Thus, for the same MNP volume, large polarizabilities and redshifted spectra, are mostly associated with MNPs that possess elongated shapes,[7,22] as well as those with sharp or pointed edges, due to their ability to induce high surface charges.[23,24] The spectroscopic properties of interest are primarily absorption, scattering, and extinction of the incident radiation. However, when MNPs are used as optical nanoantennas,[25,26,66,89] several other properties are worth considering, namely: sensitivity of the LSPR — a measure of the ease at which the LSPR changes with a change in the refractive index of the host medium,[69] quality factor — a ratio of the LSPR to the corresponding resonance linewidth,[33] figure of merit — a ratio of the sensitivity to the resonance linewidth,[66] antenna efficiency — the quantum yield of the MNP,[26,52] local field enhancement factor — a measure of the enhancement of the incident electric field due to the scattered field by the MNP,[9,99] and so on. All these properties are affected by the shape and size of the MNP, the material composition, and its dielectric environment.

Wet chemistry methods[11,27] and lithographic techniques[28] remain the dominant approaches to nanofabrication of MNPs, while classical electrodynamics is the predominant tool utilized in theoretical studies of plasmonic behaviour.[3,21] However, nanostructurization has also been reported via optical heating.[29] On the other hand, theoretical studies have become inter-disciplinary in recent years, borrowing from classical mechanics,[14,30] and circuit theory.[31–33] These approaches have led to the birth of other sub-fields, namely: plasphonics[34,35] — which investigates the interaction between surface plasmons and phonons, thermoplasmonics[29,36] — which deals with the thermal effect of plasmon excitation, magnetoplasmonics[37,38] — which looks at the effects of external magnetic fields on plasmonic behaviour as well as the effect of plasmon excitation on optomagnetic properties, molecular plasmonics[39] — which investigates plasmonic behaviour in nanostructured aggregates of certain molecular dyes,[28,40] and the interaction between surface plasmons and molecular excitons — plexcitonics.[41–43] While new applications of plasmonics are emerging gradually, such as the recently proposed plasmon-enhanced fluorescence (PEF)-based smartphone microscopy,[25] major advances have been made in the applications of plasmonics

to solar cells,[44–46] light-emitting diodes,[47,48] waveguides,[20] biosensors,[49] and nanocircuits.[33,50] Fig. 1.2(a) shows a series RLC circuit model of the optical

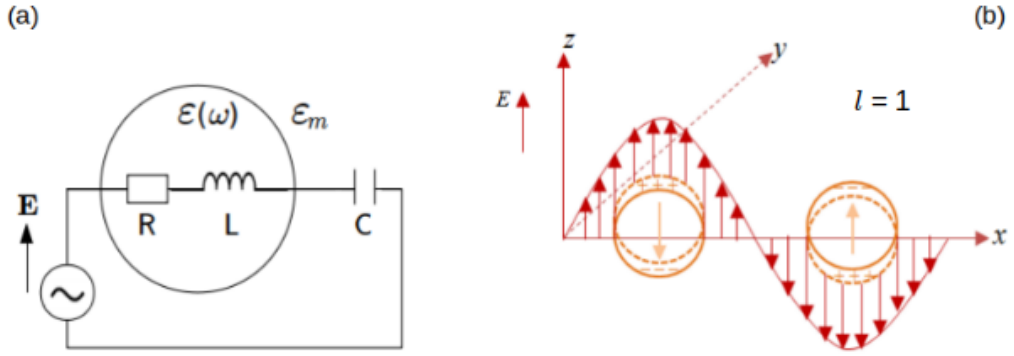

Figure 1.2: (a) Equivalent circuit model of a metallic nanosphere of dielectric constant $\varepsilon(\omega)$, embedded in a homogeneous medium of dielectric constant ε_m, in the presence of a uniform electric field **E** of frequency ω. (Adapted from Ref.[33]) (b) A complete cycle of dipole mode (with angular momentum number, $l = 1$) of the harmonic oscillation of the surface charges on the nanosphere upon plasmon excitation. (Adapted from Ref.[61])

response of a spherical MNP upon interaction with an incident field. A capacitor with capacitance C, models the dielectric response of the host medium, the incident electric field on the MNP is represented by the sinusoidal voltage source, while both an inductor and a resistor are used to model the optical response of the MNP. The resistance R of the resistor represents all the plasmon damping channels in the nanosphere, i.e., free and bound electron decay rates arising from electron scattering as well as radiation and size-dependent damping. Fig. 1.1(b) shows the oscillation of surface charges on the MNP upon excitation near its LSPR. As indicated by the arrows, the electron cloud oscillates in the opposite direction to the alternating field, leading to one complete cycle of the dipole mode. However, in the quadrupole mode ($l = 2$), half of the electron cloud oscillates in the opposite direction to the alternating field while the other half oscillates in the same direction to the field.[61] Hence, the displacement current outside the MNP flows in the opposite direction to the electric current inside it. This behaviour is modelled via the inductance L of the inductor.[2] Ref.[33] has shown that the Fröhlich condition for a metal sphere ($\Re[\varepsilon(\omega)] = -2\varepsilon_m$), is needed to satisfy the resonance condition in the circuit, via the following model parameters: $\mathrm{R} = 4\Im[\varepsilon(\omega)]/3\pi r\wp\omega$, $\mathrm{L} = 4(\varepsilon_m - \Re[\varepsilon(\omega)])/3\pi r\wp\omega^2$, $\mathrm{C} = \pi r\wp/4\varepsilon_m$, where $\wp = |\varepsilon(\omega)|^2 + \varepsilon_m^2 - 2\varepsilon_m\Re[\varepsilon(\omega)]$, and r is the sphere radius. This model effectively captures the $1/r$ dependence of the plasmon damping in nanospheres,[3,51] and the intrinsic dependence of non-radiative losses on the imaginary part of the dielectric function.[52] Such circuit models provide valuable insights for the design of plasmon circuits.[50]

Classical plasmonics uses theoretical concepts of classical physics, such as the macroscopic Maxwell's equations, to describe the optical response of plasmonic nanostructures. It is confronted by at least two challenges: the issue of gap distance-dependent electron tunnelling in dimer gaps[53] and size-dependent

electron damping in MNP sizes within the quasi-static approximation (QSA). In the QSA, the former is avoided by considering gap distances within the classical regime (Fig. 1.3(b)), where the electron tunnelling probability is negligible,[17] while the latter has only been clearly resolved in spherical MNPs.[51] The afore-

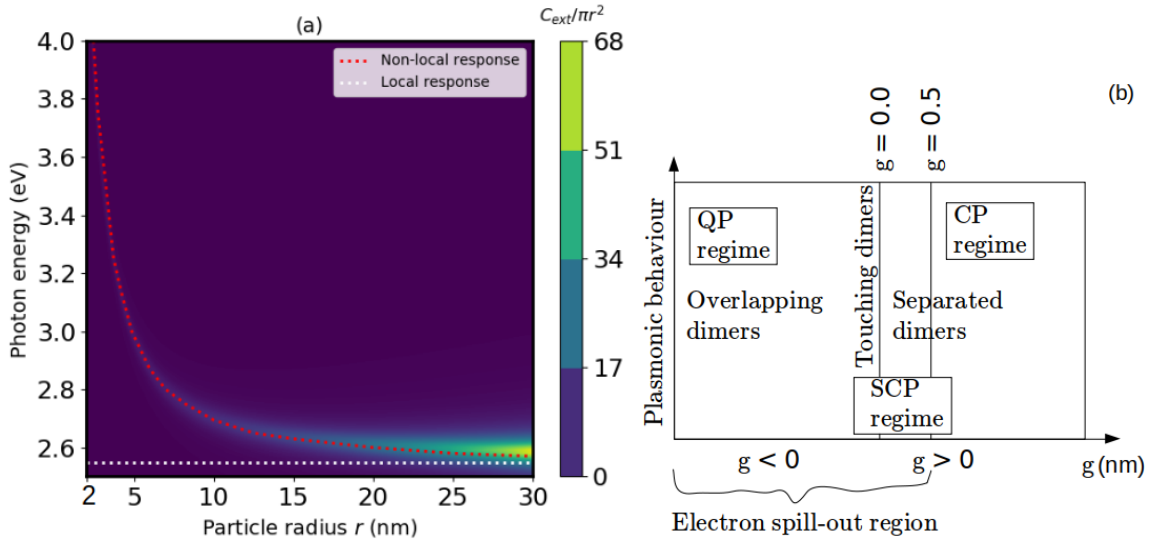

Figure 1.3: (a) Contour plot of the normalized extinction cross-section, $C_{ext}/\pi r^2$, of a spherical gold nanoparticle of radius r embedded in water, as a function of the photon energy and the particle radius for both local and non-local response. (Reproduced for gold from Ref.[3]) (b) Regimes of quantum plasmonics (QP), semi-classical plasmonics (SCP), and classical plasmonics (CP) in nanoparticle dimers as a function of the dimer gap g. (Figure was drawn based on data from Refs.[3,53])

mentioned challenges are due to non-local effects. A decrease in the MNP size causes these effects to arise from the smearing of the induced surface charges over a finite space into the MNP, and electron scattering at the MNP surface. However, in touching and overlapping dimers, non-local effects are due to electron spill-out.[3,53] As predicted by semi-classical approaches,[3,51,53,54] size-dependent damping causes both a size-dependent LSPR shift and broadening of the plasmon linewidth (Fig. 1.3(a)), while electron tunnelling leads to a non-singular response in the limit of touching dimers,[3] in agreement with experiments. Fig. 1.3(a) shows that while the local response approximation (LRA) predicts no size-dependent LSPR shift i.e 2.54 eV for all nanosphere sizes, the non-local response predicts a blueshift in the LSPR with decrease in the nanosphere radius i.e approximately 2.58 eV at 30 nm to 4.00 eV at $r = 2$ nm. However, the non-local results approach those of the local response at large r, as shown in Fig. 1.3(a). In addition, the plasmon linewidths i.e the smearing around the dashed line plot in non-local response in Fig. 1.3(a), broaden gradually with increase in particle radius. These results were obtained by including some correction terms to the local dielectric function of the metal. For instance, in Ref.,[53] a fictitious dielectric was added to the Drude model to account for the electron tunnelling probability within the gap of a nanosphere dimer, and in Refs.,[3,54] the Drude model, the continuity equation, and some part of Maxwell's equations were modified, in

order to account for non-local effects. Non-local response manifests itself through the presence of longitudinal waves.[3] As such, the local dielectric function is corrected by taking the longitudinal wavevector of the incident electric field into consideration.[3,54,55] This causes a spatial variation in the dielectric response of the metal.[54,55] Non-local response is characterized by both a pressure-driven convective flow and an entropy-driven diffusive flow of the induced charges.[54] In addition to conduction currents - which are accounted for in the local Drude model[1,3] (discussed in Section 1.2), the non-local models take the convection and diffusion of the induced surface charges into account. This leads to additional induced current densities in the Maxwell's equations.[3,54]

On the other hand, quantum plasmonics tackles these issues through several electron density-functional theories,[56,57] which have been proposed over the years. For MNP sizes below 10 nm, Ref.[3] has shown that semi-classical and quantum methods are the preferred choice, since the optical response of the MNPs is dominated by non-local effects at such sizes (Fig. 1.3(a)). However, for MNP sizes greater than 10 nm, classical plasmonics remains the preferred choice, due to its straightforwardness and the ability to account for retardation effects[3,22] (discussed in Section 1.3) - radiation reaction and dynamic depolarization of the induced field, in contrast to quantum mechanical approaches.[56,57] As shown in Fig. 1.3(b), quantum plasmonics is the preferred choice when dimer gaps approach the electron spill-out regime, while semi-classical approaches bridge the method gap between classical and quantum plasmonics.

1.2 THE LOCAL RESPONSE APPROXIMATION

The optical response of MNPs to an applied electric field of frequency ω is non-local i.e it varies spatially with the size of the metal. It is described through the constitutive equation:[1,3]

$$\mathbf{D}(r,\omega) = \varepsilon_o \int \varepsilon(r-r',\omega)\mathbf{E}(r',\omega)dr' \tag{1.1}$$

which relates the displacement field $\mathbf{D}$ to the electric field $\mathbf{E}$. $\varepsilon(r-r',\omega)$ is the non-local dielectric function of the metal and ε_o is the free space permittivity. In the local response approximation, $\varepsilon(r-r',\omega)$ has a non-zero value only at $r'=r$ described via the delta function:[1,3]

$$\varepsilon(r-r',\omega) = \delta(r'-r)\varepsilon(\omega). \tag{1.2}$$

With this approximation, Eq. (1.1) becomes

$$\mathbf{D}(r,\omega) = \varepsilon_o \int \delta(r'-r)\varepsilon(\omega)\mathbf{E}(r',\omega)dr' = \varepsilon_o\varepsilon(\omega)\mathbf{E}(r,\omega). \tag{1.3}$$

Eq. (1.3) is said to be local, since it connects $\mathbf{D}$ and $\mathbf{E}$ to the same point r in space.

When retardation and non-local effects are negligible, the optical response of MNPs is largely due to local effects. These effects arise from a short-wavelength dielectric response — due to the polarization of the positive ion core in the metal,

$\mathbf{P}_\infty$, intraband transitions at long wavelengths — due to the polarization of the free electrons, $\mathbf{P}_f$, and interband transitions at short wavelengths — due to the polarization of the bound electrons in the metal, $\mathbf{P}_b$. In order to find the local dielectric function $\varepsilon(\omega)$ in Eq. (1.3), we consider the following displacement field proposed by Drude and Lorentz:[1]

$$\mathbf{D}(r,\omega) = \varepsilon_o \left(1 + \frac{\mathbf{P}_\infty}{\varepsilon_o \mathbf{E}(r,\omega)} + \frac{\mathbf{P}_f}{\varepsilon_o \mathbf{E}(r,\omega)} + \frac{\mathbf{P}_b}{\varepsilon_o \mathbf{E}(r,\omega)}\right) \mathbf{E}(r,\omega), \tag{1.4}$$

with

$$\frac{\mathbf{P}_\infty}{\varepsilon_o \mathbf{E}(r,\omega)} = (\varepsilon_\infty - 1), \tag{1.5}$$

where ε_∞ is the short-wavelength dielectric constant of the metal.

To find $\mathbf{P}_f$, Drude considered a damped plasma model for the free electron gas under the influence of an applied electric field, according to the equation of motion:[1]

$$m\ddot{x}_f + m\gamma_f \dot{x}_f = -e\mathbf{E}(t). \tag{1.6}$$

Fourier transformation of Eq. (1.6) leads to $x_f = e\mathbf{E}(\omega)/m\omega(\omega + i\gamma_f)$, so that

$$\frac{\mathbf{P}_f}{\varepsilon_o \mathbf{E}(\omega)} = -\frac{n_f e x_f(\omega)}{\varepsilon_o \mathbf{E}(\omega)} = -\frac{\omega_f^2}{\omega(\omega + i\gamma_f)}, \tag{1.7}$$

where $\omega_f^2 = n_f e^2/m\varepsilon_o$, ω_f is the plasma frequency of the free electrons, n_f is the free-electron density, e and m are the electronic charge and mass respectively, and γ_f is the damping rate of the free electrons.

To account for interband transitions at short wavelengths, Lorentz modelled the oscillating bound electrons under the influence of the applied field, as a damped harmonic oscillator, with the equation of motion:[1,58]

$$m\ddot{x}_b + m\gamma_b \dot{x}_b + m\omega_b^2 x_b = -e\mathbf{E}(t). \tag{1.8}$$

Fourier transformation of Eq. (1.8) leads to $x_b = e\mathbf{E}(\omega)/m(\omega^2 - \omega_b^2 + i\omega\gamma_b)$. Hence

$$\frac{\mathbf{P}_b}{\varepsilon_o \mathbf{E}(\omega)} = -\frac{n_b e x_b(\omega)}{\varepsilon_o \mathbf{E}(\omega)} = -\frac{s\omega_b^2}{\omega^2 - \omega_b^2 + i\omega\gamma_b}, \tag{1.9}$$

where $\omega_b^2 = n_b e^2/sm\varepsilon_o$, ω_b is the bound-electron plasma frequency, γ_b is the damping rate of the bound electrons, n_b is the bound-electron density, and s is the oscillator strength.

Substituting Eqs. (1.5), (1.7), and (1.9), into Eq. (1.4), and comparing the result to Eq. (1.3), leads to

$$\varepsilon(\omega) = \varepsilon_\infty - \frac{\omega_f^2}{\omega^2 + i\omega\gamma_f} - \frac{s\omega_b^2}{\omega^2 - \omega_b^2 + i\omega\gamma_b}. \tag{1.10}$$

Eq. (1.10) is the local Drude-Lorentz model of the dielectric response of metals. It reduces to the local Drude model when $s = 0$.

Metal	ε_∞	s	ω_f (eV)	ω_b (eV)	γ_f (eV)	γ_b (eV)	Validity region
Au	5.9673	1.09	8.7411	2.6885	0.0658	0.4337	500 nm - 1000 nm
Ag	0.1148	3.63	8.7272	10.4074	0.0464	0.0689	400 nm - 800 nm
Au	9.07	-	8.92	-	0.076	-	700 nm - 1000 nm
Ag	4.00	-	8.79	-	0.056	-	400 nm - 800 nm

Table 1: List of fitting parameters of the Drude-Lorentz model (top) and Drude model (bottom) for the local dielectric response of gold (Au)[58] and silver (Ag),[59] and their respective validity regions.

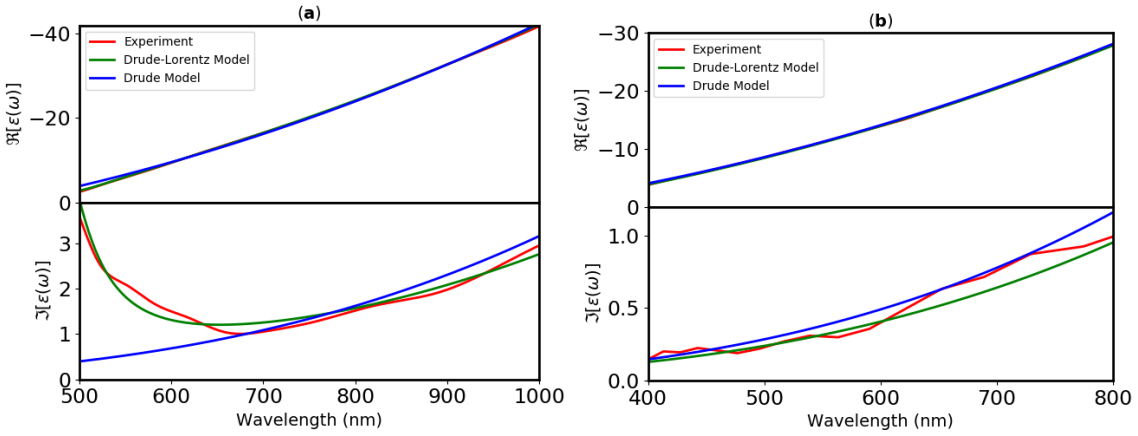

Figure 1.4: The dielectric functions of: (a) gold and (b) silver, based on the local Drude-Lorentz model (Theory) and experimental data (Experiment). Top: real parts, and bottom: imaginary parts of the dielectric functions, respectively. (Reproduced from Refs.[58,59])

We will limit our discussions of the local dielectric function to wavelengths in the range of 400 nm to 800 nm for silver[59] and 500 nm to 1000 nm for gold,[58] as shown in table 1. These correspond to the visible and infra-red regions of the electromagnetic spectrum, where most plasmonics studies are carried out.[21,24,60] At wavelengths below the optical band edge threshold in metals, incident photons can induce transitions between electronic bands by exciting electrons from the filled band below the Fermi surface (bound electrons) to an upper band.[1] As mentioned earlier, the motion of these electrons is accompanied by an additional damping term, γ_b. As shown in table 1, γ_b for gold is about six times its value in silver, and affects mostly the imaginary part, $\Im[\varepsilon(\omega)]$, of the dielectric function (Fig. 1.4). Fig. 1.4(a) shows that the onset of these interband transitions is around 700 nm for gold i.e at the overlap between the infra-red and the visible light regions. At this point, the Drude model fails to account for $\Im[\varepsilon(\omega)]$ for gold (Fig. 1.4(a), bottom plot). However, due to the low value of γ_b for silver compared to its value for gold, both the Drude and the Drude-Lorentz models are in good agreement in describing $\Im[\varepsilon(\omega)]$ for silver (Fig. 1.4(b), bottom plot), when compared to experimental data. In both metals, the models are in good agreement in describing $\Im[\varepsilon(\omega)]$, when compared to experiment data within the validity regions indicated in table 1.

However, in predicting the real part of the dielectric function, $\Re[\varepsilon(\omega)]$, the models agree quite well with the experimental data for gold, and excellent for silver (Fig. 1.4, top plots). These metals have very high negative values of $\Re[\varepsilon(\omega)]$ (Fig. 1.4, top plots) and small positive values of $\Im[\varepsilon(\omega)]$ (Fig. 1.4, bottom plots), at visible wavelengths. This material property is an essential component of high quality-low loss plasmonic materials.[2] The negative permittivity is responsible for the harmonic motion of conduction electrons at the metal-dielectric interface, upon excitation near the surface plasmon frequency. It causes the induced field outside the MNP to flow in the opposite direction to the applied field inside the MNP (Fig. 1.2(b)). Hence, $\Re[\varepsilon(\omega)]$ determines resonance oscillations in excited MNPs. On the other hand, the positive permittivity is responsible for non-radiative losses via plasmon decay.[1,52] Though both $\Re[\varepsilon(\omega)]$ and $\Im[\varepsilon(\omega)]$ contribute to radiative losses, these losses are MNP geometry-dependent while non-radiative losses are intrinsic.[52] As shown in Fig. 1.4 (bottom plots), $\Im[\varepsilon(\omega)]$ is smaller in silver compared to gold, which makes silver nanoparticles more efficient plasmonic nanoantennas compared to their gold counterparts, at the same wavelengths. However, the applicability of gold nanoparticles is less hindered by photo-oxidation compared to their silver counterparts.[4]

1.3 RETARDATION EFFECTS: THE ROLE OF MNP SIZE

Retardation effects are usually observed in electrodynamic calculations[3,21,61] and in experiments[2,10] involving MNPs of a few nanometres. They manifest themselves through both a size-dependent LSPR shift and broadening of the plasmon linewidth. They include: radiation damping and dynamic depolarization.[21,22] The polarization of the electron cloud by an incident electric field causes the MNP to acquire an induced dipole moment (Fig. 1.2(b)). Radiation damping is due to a self-reaction field produced by the induced dipole moment.[22,61,62] This reaction field acts to depolarize the MNP via the spontaneous emission of radiation by the induced dipole.[1,61,63] On the other hand, dynamic depolarization is due to the non-locality of the scattering process in time — as a result of the polarization of different parts of the MNP at different times, causing induced surface charges to oscillate in phases.[22,63]

Authors usually report the range of MNP sizes within which retardation effects are negligible to be between 20 nm - 60 nm in diameter for nanospheres.[7,61] The lower limit is such that non-local effects are negligible,[3,62] while the upper limit is such that retardation effects can be ignored.[7,22] Ford and Weber[62] have suggested that particle sizes within one-tenth of the wavelength of light in the medium can be studied with the QSA, provided that radiation damping is considered. In this section, we will look into these MNP size regimes within which the QSA is valid, for spherical and prolate spheroidal MNPs, respectively.

The effect of retardation on the dipolar LSPR of MNPs can be accounted for within the QSA by taking into account the first-order corrections due to the full retarded field.[61,62] We consider a solid nanosphere, and a solid prolate spheroid (which is usually a good approximation of a nanorod for analytical

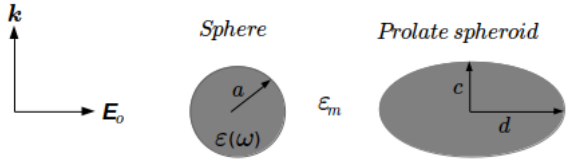

Figure 1.5: Common MNP geometries usually studied within the QSA. Each consist of a metal with a local dielectric function $\varepsilon(\omega)$, embedded in a medium of dielectric constant ε_m.

calculations[8,12]), in the presence of a uniform electric field E_o applied parallel to the long axis of the spheroid, as shown in Fig. 1.5. The induced dipole moment p_{ind} on the spheroid produces a radiation reaction field E_{rr}, which is in anti-phase with the induced field and proportional to p_{ind}. In addition, a dynamic depolarization field E_{dp}, also proportional to p_{ind}, acts in phase to the radiation reaction field. The effective induced dipole moment can therefore be re-written as[61,62]

$$p_{ind} = \alpha_s(\omega)(E_o + E_{rr} + E_{dp}), \tag{1.11}$$

where[12,22]

$$\alpha_s(\omega) = \frac{V}{4\pi}\frac{\varepsilon(\omega) - \varepsilon_m}{\varepsilon_m + L_s[\varepsilon(\omega) - \varepsilon_m]} \tag{1.12}$$

is the static longitudinal dipole polarizability of the spheroid. $\varepsilon(\omega)$ is the dielectric function of the material of the spheroid, ε_m is the dielectric constant of the host medium, V is the volume of the spheroid, and L_s is its longitudinal static geometric factor.

First-order corrections report $E_{rr} = i2k_m^3 p_{ind}/3$[22,61,62] and $E_{dp} = k_m^2 L_d p_{ind}/l$,[22] respectively, where $k_m = 2\pi\sqrt{\varepsilon_m}/\lambda$ is the wave number of light in the medium, λ is the wavelength, l is the half-length of the spheroid, and L_d is its longitudinal dynamic geometric factor. Substituting these two expressions into Eq. (1.11) leads to the dynamic longitudinal dipole polarizability of the spheroid:

$$\alpha_d(\omega) = \frac{\alpha_s(\omega)}{1 - \frac{k_m^2 L_d}{l}\alpha_s(\omega) - \frac{i2k_m^3}{3}\alpha_s(\omega)}, \tag{1.13}$$

which reduces to the static response when $k_m = 0$. The shape-dependent parameters include:[12,22]

$$\begin{cases} L_s = [(v\coth^{-1} v) - 1](v^2 - 1), & v = d/f,\ d > c,\ l = d, \\ L_d = \frac{3}{4}[1 + L_s(v^2+1)(v^2-1)^{-1}], & f = \sqrt{d^2 - c^2},\ \text{(Prolate spheroid)} \\ L_s = 1/3,\ L_d = 1, & l = a\ \ \text{(Sphere)}, \end{cases} \tag{1.14}$$

where d and c are the half-length and half-width of the spheroid, respectively, f is the focal distance of the spheroid, v is its radial coordinate, and a is the sphere radius. Here, Eq. (1.13) shows that the radiation reaction term changes the real part of $\alpha_s(\omega)$ into a complex value and the imaginary part into a real value, while the dynamic depolarization term contributes equally to both the

real and imaginary parts of $\alpha_s(\omega)$ without interchanging their roles. Hence, radiation damping introduces size-dependent radiative losses in the extinction cross-section of the MNP, by reducing the dipole polarizability, resulting in a size-dependent broadening of the plasmon linewidth.[1,61] On the other hand, dynamic depolarization introduces a change in the effective polarization, resulting in a size-dependent shift of the dipolar LSPR of the MNP.[61,63]

The extinction cross-section of each of the above MNP geometries, which originates from both the radiative (scattered) and non-radiative (absorbed) powers, due to interaction with the incident field, is calculated using Eq. (1.13) as[7,8]

$$C_{ext} = C_{sca} + C_{abs}, \tag{1.15a}$$

$$C_{sca} = \frac{k_m^4}{6\pi}|\alpha_d(\omega)|^2, \;\; C_{abs} = k_m \Im[\alpha_d(\omega)], \tag{1.15b}$$

where C_{sca} and C_{abs} are the scattering and absorption cross-sections, respectively. In the following contour plots, Figs. 1.6 and 1.7 (Here, we focus only on the size-induced resonance shifts in the spectra, so that colour bars are not shown.), we consider the effects of retardation on the dipolar LSPR of spheres and prolate spheroids, respectively. We restrict the lower bound of MNP size to 10 nm, below which non-local effects dominate.[3] Fig. 1.6(a) and Fig. 1.6(c) are the contour plots of the extinction cross-sections of gold and silver nanospheres, respectively, without retardation effects. In Fig. 1.6(a) and Fig. 1.6(c), the QSA does not lead to any size-dependent LSPR shift as the radii of the nanospheres (NS) are varied from 10 nm to 50 nm. It predicts approximately 525 nm as the dipolar LSPR of the gold NS (Fig. 1.6(a)), and approximately 398 nm as the dipolar LSPR of the silver NS (Fig. 1.6(c)), regardless of MNP size.

Fig. 1.6(b) and Fig. 1.6(d) are the contour plots of the extinction cross-sections of gold and silver nanospheres, respectively, with retardation effects. In contrary to the plots without retardation effects, discussed above, Fig. 1.6(b) and Fig. 1.6(d) show a redshift of the dipolar plasmon peak position as the radii of the NS increase from 10 nm to 50 nm. However, the redshift is more pronounced in silver NS (Fig. 1.6(d)) than in gold NS (Fig. 1.6(c)), due to a strong dependence of the retardation terms on short wavelengths, and on material properties. In Fig. 1.6(b), no significant redshift in the dipolar LSPR is observed from a radius of 10 nm to around 25 nm, beyond which a noticeable redshift begins to occur, reaching nearly 600 nm at 50 nm radius. However, in Fig. 1.6(d), a noticeable redshift in the dipolar LSPR from 398 nm to 400 nm has already taken place at 10 nm radius, which further approaches 550 nm at 50 nm. Fig. 1.6(b) and Fig. 1.6(d), respectively, also feature size-dependent broadening of the plasmon linewidths — which are noticeable from the increased spread of the contours in Fig. 1.6(b) and Fig. 1.6(d) compared to those in Fig. 1.6(a) and Fig. 1.6(c). Therefore, the MNP size regime where the validity of the QSA is not questionable is likely between 20 and 50 nm in diameter for gold NS, and less than 20 nm for silver NS.

Fig. 1.7(a) and Fig. 1.7(c) are the contour plots of the extinction cross-sections of gold prolate spheroids, at constant half-widths and half-lengths, respectively, without retardation effects. Fig. 1.7(a) and Fig. 1.7(c), shows the QSA results for the size-dependence of the longitudinal dipolar LSPR in prolate spheroids.

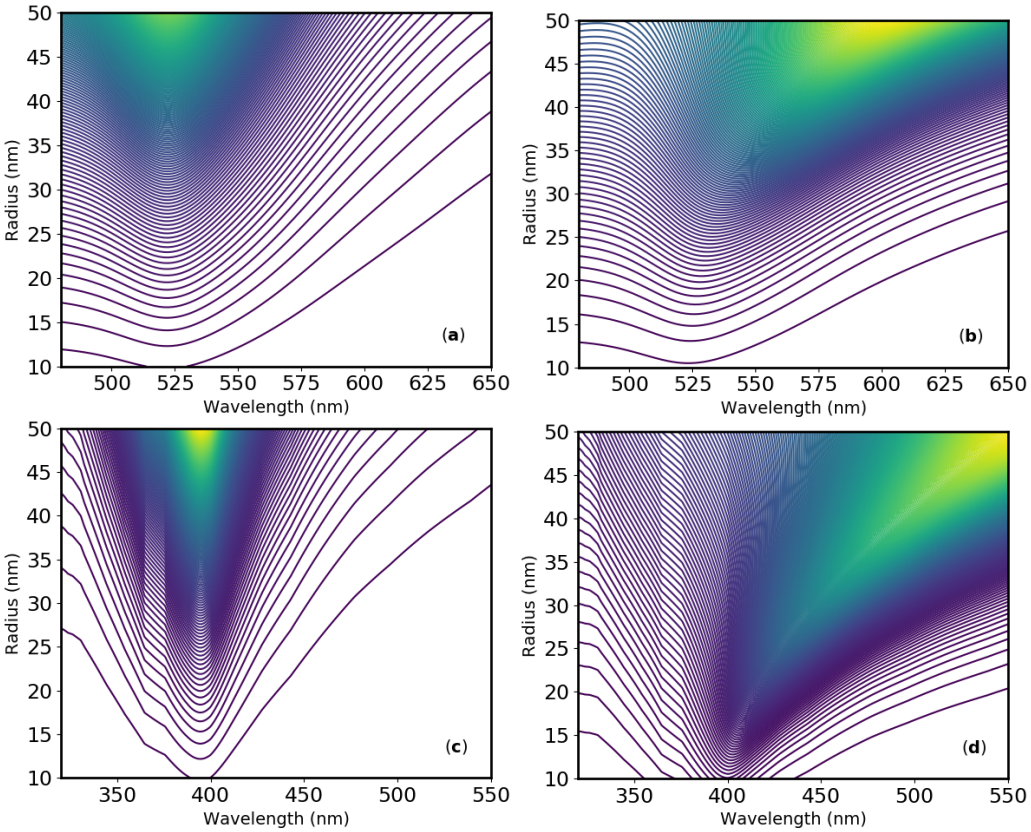

Figure 1.6: Contour plots of the extinction cross-sections of single gold nanospheres (top) and silver nanospheres (bottom) embedded in water, as a function of the particle radius and wavelength. (a) and (c): without retardation effects. (b) and (d): with retardation effects.

Fig. 1.7(a) shows a redshift in the dipolar LSPR as the half-length is increased at constant half-width while Fig. 1.7(c) shows a redshift in the dipolar LSPR as the half-width is decreased at constant half-length. In either case, the aspect ratio of the spheroid is increasing. However, there is an underlying flaw in these predictions, i.e., both Fig. 1.7(a) and Fig. 1.7(c) show that two different prolate spheroids with the same aspect ratio will have the same dipolar LSPR.

Fig. 1.7(b) and Fig. 1.7(d) are the contour plots of the extinction cross-sections of gold prolate spheroids, at constant half-widths and half-lengths, respectively, with retardation effects. As revealed by retardation effects via Fig. 1.7(b) and Fig. 1.7(d), when two different prolate spheroids have the same aspect ratio, the dipolar LSPR of the spheroid with a longer half-length will be more redshifted compared to the spheroid with a shorter half-length. For instance, let us consider two prolate spheroids with half-lengths of 25 nm and 50 nm, and half-widths of 10 nm and 20 nm, respectively. The aspect ratio of both spheroids is 2.5. Fig. 1.7(a) and Fig. 1.7(c) predict the dipolar LSPR of both spheroids as 560 nm, approximately. According to Fig. 1.7(b), the dipolar LSPR of the 25 nm by 10 nm spheroid is around 565 nm, while Fig. 1.7(d) predicts the dipolar LSPR of the 50 nm by 20 nm spheroid as 595 nm, approximately. As shown in Fig. 1.7(a) and Fig. 1.7(b), the MNP size regime within which the QSA is valid is very narrow

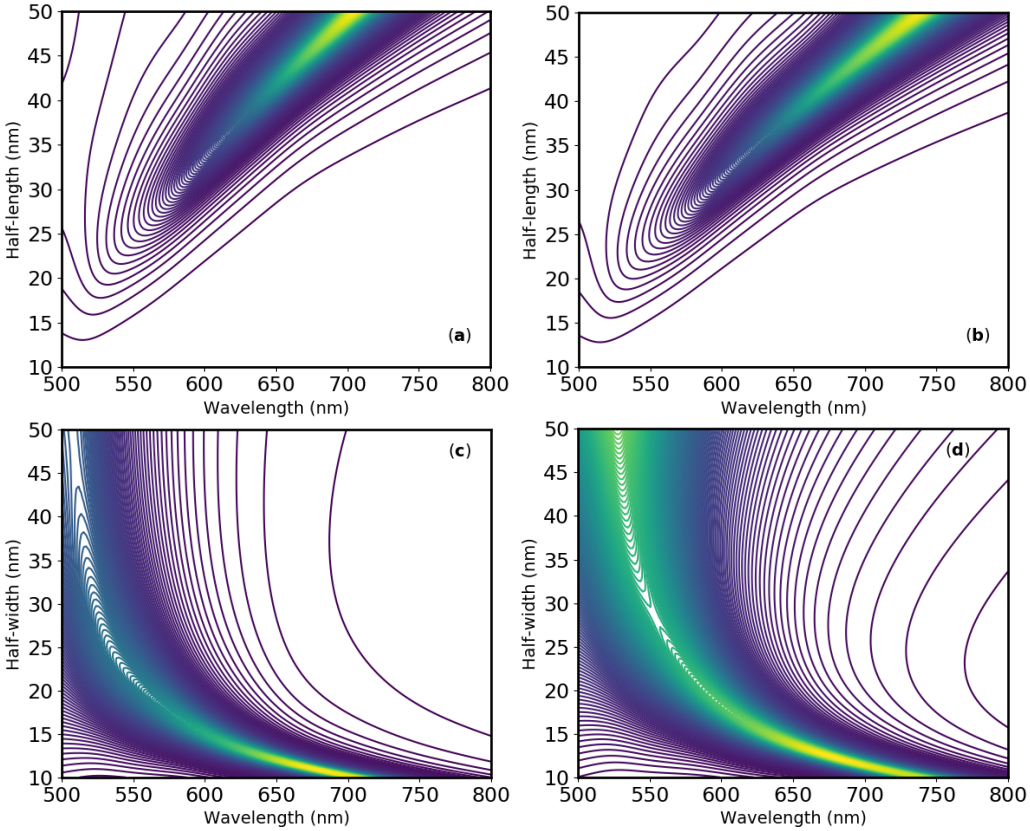

Figure 1.7: Contour plots of the extinction cross-sections of single gold prolate spheroids embedded in air, as a function of the spheroid size and wavelength. Top: half-length varied at constant half-width of 10 nm. Bottom: half-width varied at constant half-length of 50 nm. (a) and (c): without retardation effects. (b) and (d): with retardation effects.

for spheroids, i.e., less than 25 nm of the half-length for a constant half-width of 10 nm. The validity region is further compromised when the half-length is longer than 25 nm, irrespective of the half-width, as shown in Fig. 1.7(c) and Fig. 1.7(d).

1.4 THESIS OUTLINE

This thesis presents a theoretical study of the following phenomena: localized surface plasmon resonance (LSPR), plasmon-induced transparency (PIT), plasmon-enhanced fluorescence (PEF), and exciton-induced transparency (EIT). The first two occur in plasmonic nanostructures or in a system of such nanostructures, i.e., dimers, while the latter two occur in plexcitonic systems, such as hybrid metal-molecule nanostructures. LSPR has been introduced in Chapter 1, and will be discussed in more detail, alongside PIT, in Chapter 2. PEF will be discussed in Chapters 3 and 4, while EIT is discussed in Chapter 4. Applications will be mentioned in passing while we focus on our theoretical results limited to single metal nanoparticles (MNPs) and dimers. The thesis concludes in Chapter 5 with the summary of the major findings of the research projects presented in previous Chapters, as well as perspectives on an on-going work.

The theoretical approach we adopted is the quasi-static theory. It is well within the framework of classical electrodynamics when retardation effects are negligible. As such, it is an approximate theory, better referred to as the quasi-static approximation (QSA) or the non-retarded field limit.[1,21] The QSA has been shown to agree with experiments involving MNP sizes and inter-particle distances that are small compared to the wavelength of light in the medium: the so-called Rayleigh regime. It has also been shown to agree with other theoretical methods such as the plasmon hybridization theory,[14,64] and transformation optics,[65,66] within the local response approximation (LRA).

Our discussions will not be complete without mentioning the pioneers of the QSA — theorists whom we have either borrowed directly from or modified a few of their formulations to suit ours. They include: Rayleigh — who laid the theoretical foundation of the QSA, Laplace — whose equation is indispensable in potential theory, Fröhlich — who defined the LSPR condition, Gersten and Nitzan and Ford and Weber — who independently developed the theory of PEF within the QSA. We must also mention that what makes the QSA very relevant is its intuitive simplicity, made possible by the existence of orthogonal series expansion of electrostatic potentials in almost any coordinate system. For instance, some authors have noted that a Mie expansion is not possible for scattering by spheroids, since such expansion of electrodynamic potentials is not available in a spheroidal basis.[67]

All major derivations are relegated to the appendix sections, while final results such as polarizabilities, and so on, will be presented in the main body of the thesis. We have used Python for translating formulae to visualizable data.

2

SURFACE PLASMONS AND PLASMON COUPLING

2.1 PROPAGATING SURFACE PLASMONS

In planar nanostructures consisting of one or more metal-dielectric interface, excitations formed via the interaction between an incident electromagnetic field and the conduction electrons in the metal, propagate at the interface. These longitudinal excitations are bounded perpendicularly to the interface, and decay over a finite distance along it, as shown in Fig. 2.1(a). They are known as *propagating surface plasmons* (PSPs) or surface plasmon polaritons,[21,68] with the plasmon resonance frequency:[68]

$$\omega_{psp} = \frac{\omega_p}{\sqrt{\varepsilon_\infty + \frac{\varepsilon_m}{1-(k_m/\kappa)^2}}}. \tag{2.1}$$

Here, $k_m = k_o\sqrt{\varepsilon_m}$ is the wavenumber of light in the medium, k_o is the free-space wavenumber, κ is the complex propagation constant given by:[68] $\kappa = k_m\sqrt{\varepsilon(\omega)\varepsilon_m/[\varepsilon_m + \varepsilon(\omega)]}$, with $\varepsilon(\omega)$ as the dielectric function of the metal, and ε_m as the dielectric constant of the medium. Therefore, κ is always greater than k_m, so that in practice, special phase-matching techniques are needed to excite PSPs,[1] since their dispersion lies outside (for example, on the right side of the light line in Fig. 2.1(c) i.e the lower branch) the light cone of the dielectric. For instance, using a glass prism coupling, PSPs between the light lines of glass and air, can be excited, as shown in Ref.[1] For lossless metals, κ becomes real, since $\Im[\varepsilon(\omega)]$ vanishes.

Fig. 2.1(a) also shows that PSPs are formed at the interface between two materials with opposite signs of the real parts of their dielectric functions i.e $\varepsilon_m > 0$ for the dielectric medium, and $\Re[\varepsilon(\omega)] < 0$ for the metal. PSPs will only propagate at the interface in the presence of a transverse-magnetic (TM) polarized incident field (Fig. 2.1(a)) i.e $E_x \neq E_z \neq H_y \neq 0$ and $H_x = H_z = E_y = 0$, where **E** and **H** are the electric and magnetic fields, and the subscripts denote the field components, respectively. The evanescent fields propagate at different lengths into the metal and the dielectric, respectively, as shown by sketches of the magnitude of the z-component of the electric field ($|\mathbf{E_z}|$) in each region (Fig. 2.1(a)). The differences in propagation lengths between the metal and the dielectric are due to the penetration depths, which are in the range of μm in the dielectric and nm in the metal.[1]

As shown in Fig. 2.1(a), as well as in Eq. (2.1), these evanescent excitations modify the free-electron plasma frequency of the metal, ω_p (here we use ω_p for ω_f) into a surface plasmon frequency, ω_{psp}. Due to the quadratic dependence of ω_{psp} on κ (Eq. (2.1)), the bounded surface waves have two branches (Fig. 2.1(c)). The lower branch, which exists on the right side of the light line ($\omega = ck_o$,

where c is the speed of light in free-space), bounded at $\omega_p > \omega < \omega_{sp}$, are the PSPs,[68] while the upper branch, which exists at small propagation constants (for example, in Fig. 2.1(c), at $0 < \kappa \leq 18 \times 10^{-3}$ nm^{-1}), bounded at $\omega > \omega_p$, on the left side of the light line, are referred to as *Sommerfield-Zenneck waves*.[1] PSPs become quasi-static at large propagation constants. For example, in Fig. 2.1(c), when $\kappa > 30 \times 10^{-3}$ nm^{-1}, ω_{psp} approaches ω_{sp}. In this limit, they become non-propagating, and are simply called *surface plasmons*.[1,68] The characteristic surface plasmon resonance frequency is obtained from Eq. (2.1) when $\kappa \longrightarrow \infty$ or $k_m \longrightarrow 0$ (static limit) as:

$$\omega_{sp} = \frac{\omega_p}{\sqrt{\varepsilon_\infty + \varepsilon_m}}. \tag{2.2}$$

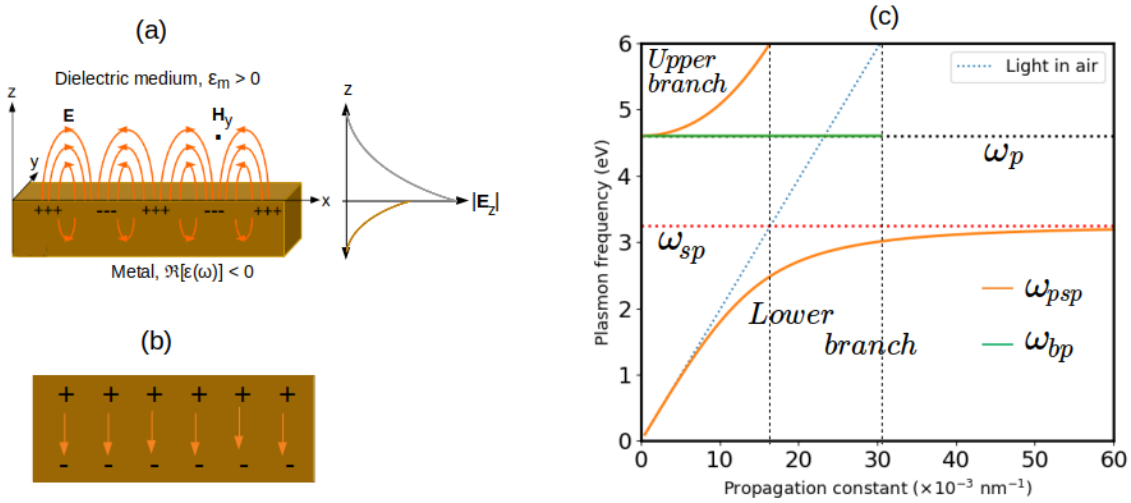

Figure 2.1: (a) Surface charge propagation at the interface between a metal layer and air, when TM polarized light is applied at the metal-air interface. Appended to the right side of the figure are sketches of the z-component of the evanescent electric field in each region, respectively. (b) Distribution of charges inside the metal. (c) Dispersion relation of bulk and surface plasmons of a metal-insulator geometry (Reproduced from Ref.[68] based on a lossless Drude model for gold, using $\omega_p = 4.6$ eV, $\varepsilon_\infty = 1$, with air, $\varepsilon_m = 1$, as the insulating medium). Here, ω_p is the free-electron plasma frequency of the metal, ω_{psp} is the resonance frequency of the propagating surface plasmons, ω_{sp} is the resonance frequency of the surface plasmons, and ω_{bp} is the resonance frequency of the bulk plasmons.

In bulk metals, longitudinal collective oscillations of free electrons also occur inside the metal (Fig. 2.1(b)). These excitations do not couple to electromagnetic radiation, and are usually formed via ion impact.[1] They are caused by radiation into the metal, which occurs at $\omega > \omega_p$, as shown in Fig. 2.1(c). They are observed at finite wave vectors (for example, Fig. 2.1(c), at $\kappa \leq 30 \times 10^{-3}$ nm^{-1}), and are known as *volume plasmons* or *bulk plasmons*,[1,4] with the bulk plasmon resonance frequency:[1]

$$\omega_{bp} = \sqrt{\omega_p^2 + \frac{3}{5} v_F^2 k_m^2}, \tag{2.3}$$

where v_F is the Fermi velocity of the free electrons in the metal.

In-between the bulk plasmons and the surface plasmons i.e at $\omega_{bp} > \omega > \omega_{sp}$ in Fig. 2.1(c), is a frequency gap, where there is no plasmon propagation. The plasma dispersion in this region (not shown in Fig. 2.1(c)) is due to the imaginary part of the complex propagation wavevector in lossy metals, as shown in Refs.[1,68]

2.2 LOCALIZED SURFACE PLASMONS [1]

In MNPs, incident electromagnetic fields interact with conduction electrons to form non-propagating excitations called *localized surface plasmons* (LSPs).[1,21] These particle-confined excitations are due to resonant oscillation of the electron cloud, as a result of a harmonic force exerted by the particle shape. The frequencies of the normal modes of these oscillations correspond to their LSPR. For an arbitrary MNP geometry, these modes can be investigated by solving the scattering problem of the particle in a uniform electromagnetic field.[1,8] For MNP sizes small compared to the wavelength of light in the medium, Refs.[1,8] have shown that the induced field on the MNP is dominated by the electric field component, and that the magnetic field component approaches zero in the static limit. This is called the *Rayleigh approximation* or the *quasi-static approximation*. In this regime, LSPs can be investigated by solving the scattering problem of a particle in a uniform electrostatic field.[1,4,8]

Here, we report the LSPR of single MNPs which we have studied within the QSA. Single particle studies have identified a number of unique plasmonic behaviour in MNPs. Such as: plasmon hybridization of solid and cavity plasmons in nanoshells,[57,64,69] mode-mixing in nanoeggs[13,14] and nanocups,[15] incident field polarization-dependent LSPR in nanorods,[1,8] as well as *dark modes* (multipolar modes) in silver nanodisks,[70] and so on.

In the Rayleigh limit, the dipolar mode, also known as the *bright mode*,[71] contributes most to the absorption cross-section of the MNP. This is because the electron cloud undergoes an intense polarization in the dipolar mode compared to higher-order modes.[21] The LSPR of the dipolor mode manifests itself as the position of absorption maximum,[61] and reveals a lot of detail pertaining to the size and shape dependence of plasmonic behaviour in single MNPs. This has led to both theoretical and experimental studies of a myriad of particle sizes of various shapes. Such as: nanocavities,[1] concentric nanoshells,[64] and MNPs with smooth edges; spheres,[7,61] spheroids,[22,61] and ellipsoids[8] or with sharp edges; nanoprisms,[21] nanostars,[24] and nanocubes,[2,21] and so on. Though difficult to fabricate, reduced-symmetry MNPs; nanoeggs,[14,66,71] nanocups,[15] and nanocaps,[16] are also studied in plasmonics literature. MNPs with sharp edges and reduced-symmetry feature mostly redshifted spectra,[15,24] accompanied by intense local field enhancements,[21,71] compared to their counterparts.

Single MNPs have been shown to display some common trends in their plasmonic behaviour, despite their differences in shape. For example, plasmon hybridization of solid and void plasmons, and the presence of symmetric and

[1] some part of this section has been published in plasmonics (see pp. i) .

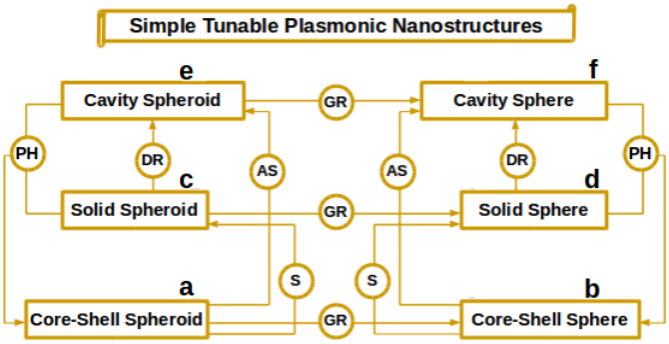

Figure 2.2: A tree diagram illustrating the relationships between the LSPR of the nanostructures we have studied in this section. **PH**, Plasmon Hybridization, **DR**, Dielectric Reversal, **GR**, Geometric Reduction, **S**, Symmetrization, and **AS**, Anti-Symmetrization.

asymmetric modes in nanoshells,[64] nanorice,[69] and so on. We took this further by exploring other possible relationships among the members of a group of tunable plasmonic nanostructures which we have categorized as *simple*. This classification is based on three typical properties: their dipolar LSPR can be expressed analytically via certain formulas, the MNPs have smooth edges, and some relationships exist among them according to Fig. 2.2. Our main objective is to derive the multipolar and dipolar LSPR of a nanorice (a core-shell prolate spheroid), and show that using these relationships, the multipolar and dipolar LSPR of a concentric nanoshell (a core-shell sphere), and those of other nanostructures in Fig. 2.2, can be derived, straightforwardly. These derivations will include dielectric effects. We conclude this section by presenting a simplified model of plasmon hybridization in the core-shell MNPs in Fig. 2.2 and Fig. 2.3.

Our theoretical approach relies on a series solution of the Laplace equation for the target MNP geometry, in order to obtain the static multipole polarizability.[72–74] Once the polarizability of the MNP is found, the LSPR can be derived using a combination of the Drude model, and the LSPR condition, also called the Fröhlich condition.[7,21] The polarizability is a complex quantity that determines the ease at which the electron cloud is polarized upon the application of an electric field. It depends on shape, size, material composition, and dielectric environment of the MNP, as well as on the frequency of the incident radiation, ω. Given some multipole polarizability $\alpha_{lm}(\omega)$ (where the angular momentum number l indicates the number of multipoles, and the azimuthal number m indicates either a perpendicular ($m = \pm 1$) or parallel polarization ($m = 0$) of the incident electric field), the LSPR is found via the poles of $\alpha_{lm}(\omega)$. The Fröhlich condition states that at resonance: $\omega \approx \omega_r$, the real part of ω_r gives the LSPR while the imaginary part corresponds to the plasmon linewidth.[1,3,21] Hence, an expression for $\varepsilon(\omega_r)$ is needed from the denominator of $\alpha_{lm}(\omega_r)$ to solve for ω_r via the Drude model. If damping is ignored, then $\Re[\varepsilon(\omega_r)] = \varepsilon(\omega_r)$, allowing one to obtain only the LSPR. To obtain $\alpha_{lm}(\omega)$, the amplitude of the electric potential induced on a given MNP (also referred to as the amplitude of the scattered potential[73]) is expressed in terms of the amplitude of the external potential.

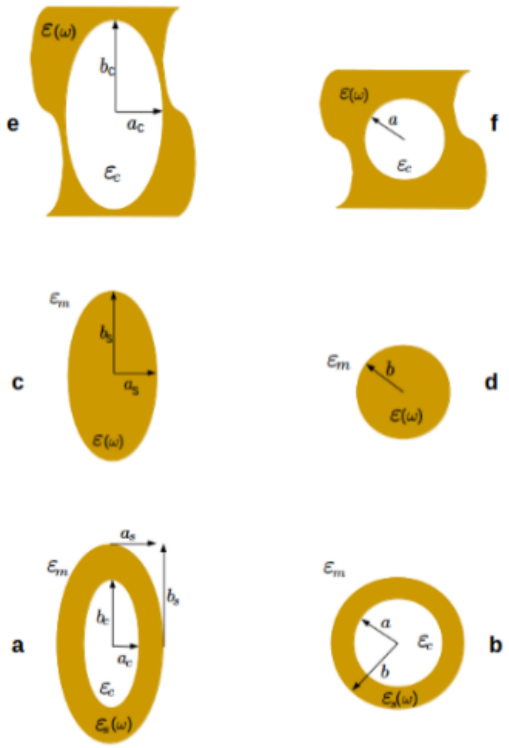

Figure 2.3: Model geometries of the MNPs we have classified as *simple*. (a) A core-shell prolate spheroid of aspect ratio $q_s = b_s/a_s$, with a shell of non-uniform thickness and a confocal core of aspect ratio $q_c = b_c/a_c$. (b) A core-shell sphere of aspect ratio a/b, with a shell of uniform thickness and a concentric core. Each core-shell nanostructure is embedded in a homogeneous dielectric medium of dielectric constant ε_m. The shell consists of a metal of dielectric function $\varepsilon_s(\omega)$, and the core is filled with a dielectric of dielectric constant ε_c. (c) A solid prolate spheroid of aspect ratio b_s/a_s. (d) An isotropic solid sphere of radius b. Each solid nanostructure consists of a metal of dielectric function $\varepsilon(\omega)$, embedded in a homogeneous dielectric medium of dielectric constant ε_m. (e) A prolate spheroidal cavity of aspect ratio b_c/a_c. (f) An isotropic spherical cavity of radius a. Each cavity is formed in a homogeneous infinite metallic background of dielectric function $\varepsilon(\omega)$, and filled with a dielectric of dielectric constant ε_c.

Upon resonant excitation, one obtains ω_r from the real part of Eq. (1.10) (at $s = 0$, with ω_f replaced with ω_p) as:

$$\omega_r = \frac{\omega_p}{\sqrt{\varepsilon_\infty - \Re[\varepsilon(\omega_r)]}}, \tag{2.4}$$

where the damping rate of the free electrons, γ_f, has been ignored, following the approach of Wu et al.[14] This involves the use of a renormalized value of ω_p, with $\varepsilon_\infty = 1$, without considering free-electron damping. It reproduces observed values of the LSPR of spherical gold nanoshells over a wide range of aspect ratios.[14] Therefore, we have chosen to consider gold MNPs only, with $\omega_p = 4.6$ eV (the renormalized value of ω_p reported in Ref.[14] for gold). For convenience, the subscript "r" in Eq. (2.4) will be dropped. The symbol $|A|$ denotes the determinant of A, wherever it appears.

2.2.1 *Hybrid Plasmons*

In this section, we will report the multipolar and dipolar LSPR of a nanorice, which we have obtained with the inclusion of the dielectric constants $\varepsilon_\infty, \varepsilon_c$ and ε_m. The MNPs considered include a nanorice (Fig. 2.3(a)) and a concentric nanoshell (Fig. 2.3(b)). We will then derive the multipolar LSPR of the nanoshell from that of a nanorice using Geometric Reduction (**GR**). The plasmon modes of these core-shell MNPs can be referred to as the *hybrid plasmon modes*, since they are formed via hybridization of the fundamental plasmon modes.[64,69] We will discuss the hybridization of plasmons in these nanoshells in Subseection 2.2.3.

Following the approach described in Section 2.2, the poles of the multipole polarizability $\alpha_{lm}(\omega)$ of a nanorice, i.e., a core-shell prolate spheroid (Fig. 2.3(a)) (see Appendix F) are:

$$\Re[\varepsilon_s(\omega_r)] = \frac{-[\beta+\zeta-\Omega(\varepsilon_c+\varepsilon_m)] \pm \sqrt{\begin{vmatrix} [\beta+\zeta-\Omega(\varepsilon_c+\varepsilon_m)] & 4(\Omega-\Delta) \\ (\varepsilon_c\varepsilon_m\Omega-\Lambda) & [\beta+\zeta-\Omega(\varepsilon_c+\varepsilon_m)] \end{vmatrix}}}{2(\Omega-\Delta)}, \tag{2.5}$$

where

$$\Lambda \equiv \varepsilon_m\varepsilon_c \frac{Q'_{lm}(v_s)Q_{lm}(v_c)P_{lm}(v_s)}{P_{lm}(v_c)}, \Delta \equiv \frac{Q_{lm}(v_s)Q'_{lm}(v_c)P'_{lm}(v_s)}{P'_{lm}(v_c)}, \tag{2.6a}$$

$$\frac{\beta}{\varepsilon_m} \equiv \frac{Q'_{lm}(v_s)Q'_{lm}(v_c)P_{lm}(v_s)}{P'_{lm}(v_c)}, \frac{\zeta}{\varepsilon_c} \equiv \frac{Q_{lm}(v_s)Q_{lm}(v_c)P'_{lm}(v_s)}{P_{lm}(v_c)}, \tag{2.6b}$$

$$\text{and } \Omega \equiv Q_{lm}(v_s)Q'_{lm}(v_s). \tag{2.6c}$$

Here, $P_{lm}(v_c)$ and $Q_{lm}(v_c)$ are the associated Legendre functions of the first and second kind, respectively, evaluated at the core surface: $v = v_c = a_c/f$; $P_{lm}(v_s)$ and $Q_{lm}(v_s)$ are similar functions evaluated at the shell surface: $v = v_s = a_s/f$; v is the radial coordinate of the spheroid; and f is the focal length of the spheroid (which is the same for the core and the core-shell for confocal spheroids[73,74]). The primes denote derivatives with respect to the radial coordinate at the corresponding surfaces.

Substituting Eq. (2.5) for $\Re[\varepsilon(\omega_r)]$ in Eq. (2.4), we obtain the multipolar LSPR of the nanorice:[12]

$$\omega_{lm}^{\pm} = \frac{\omega_p}{\sqrt{2}} \sqrt{\frac{\begin{vmatrix} 2\varepsilon_\infty & -1 \\ [\beta+\zeta-\Omega(\varepsilon_c+\varepsilon_m)] & (\Omega-\Delta) \end{vmatrix} \pm \sqrt{\begin{vmatrix} \beta & 1 \\ \zeta & 1 \end{vmatrix}^2 + \begin{vmatrix} \varepsilon_m\Omega(1+\varepsilon_c) & -4 \\ [\Lambda\Omega-\varepsilon_c\varepsilon_m\Omega(\Omega-\Delta)] & [\varepsilon_m\Omega(1+\varepsilon_c)-2(\beta+\zeta)] \end{vmatrix}}}{\begin{vmatrix} [\varepsilon_\infty^2(\Omega-\Delta)+(\varepsilon_c\varepsilon_m\Omega-\Lambda)] & -\varepsilon_\infty \\ [\beta+\zeta-\Omega(\varepsilon_c+\varepsilon_m)] & 1 \end{vmatrix}}}, \tag{2.7}$$

where $\omega_{l0}^{\pm}$ is the longitudinal LSPR (LLSPR) and $\omega_{l1}^{\pm}$ is the transverse LSPR (TLSPR). The former is due to the incident field polarization along the long axis of the spheroid, while the latter is due to polarization along its short axis. The higher-energy LSPR ω_{lm}^{+}, are due to antisymmetric hybridization of solid and cavity (void) plasmons of the nanorice, i.e., modes from Fig. 2.3(c) and Fig. 2.3(e) of equivalent dimensions. while the lower-energy LSPR ω_{lm}^{-}, are

due to symmetric hybridization.[12,69] For a core-shell oblate spheroid, the LSPR are calculated by making the transformations: $v_c \to iv_c$ and $v_s \to iv_s$, in the Legendre functions.[72,74]

In the dipole limit $l = 1$, with Eqs. (2.6a) - (2.6c), the terms in Eq. (2.7) simplify to the following:

$$f(v_c, v_s) = v_c(v_c^2 - 1)(v_s^2 - 1), \tag{2.8a}$$

$$\beta - \zeta = \frac{1}{f(v_c, v_s)} \begin{vmatrix} \varepsilon_m(1 - L_c^m) & \varepsilon_c L_c^m L_s^m \\ 1 & (1 - L_s^m) \end{vmatrix}, \tag{2.8b}$$

$$\begin{vmatrix} 2\varepsilon_\infty & -1 \\ [\beta + \zeta - \Omega(\varepsilon_c + \varepsilon_m)] & (\Omega - \Delta) \end{vmatrix} = \frac{\begin{vmatrix} 2L_s^m\varepsilon_\infty + \varepsilon_m(1 - L_c^m - L_s^m) & (\varepsilon_m + \varepsilon_c - 2\varepsilon_\infty) \\ -L_s^m[L_c^m + f_c(1 - L_s^m)] & 1 \end{vmatrix}}{f(v_c, v_s)}, \tag{2.9}$$

$$\begin{vmatrix} [\varepsilon_\infty^2(\Omega - \Delta) + (\varepsilon_c\varepsilon_m\Omega - \Lambda)] & -\varepsilon_\infty \\ [\beta + \zeta - \Omega(\varepsilon_c + \varepsilon_m)] & 1 \end{vmatrix} = \frac{\begin{vmatrix} [\varepsilon_m(1 - L_s^m) + \varepsilon_\infty L_s^m] & -f_c L_s^m(1 - L_s^m) \\ [\varepsilon_\infty(\varepsilon_m + \varepsilon_c - \varepsilon_\infty) - \varepsilon_m\varepsilon_c] & [\varepsilon_\infty(1 - L_c^m) + \varepsilon_c L_c^m] \end{vmatrix}}{f(v_c, v_s)}, \tag{2.10}$$

$$\begin{vmatrix} \varepsilon_m\Omega(1 + \varepsilon_c) & -4 \\ [\Lambda\Omega - \varepsilon_c\varepsilon_m\Omega(\Omega - \Delta)] & [\varepsilon_m\Omega(1 + \varepsilon_c) - 2(\beta + \zeta)] \end{vmatrix} = \frac{f_c L_s^m(1 - L_s^m)}{f(v_c, v_s)} \begin{vmatrix} L_s^m[2L_c^m + f_c(1 - L_s^m)] & -2\varepsilon_m \\ [\varepsilon_m + \varepsilon_c + (L_c^\parallel + L_s^m)(\varepsilon_c - \varepsilon_m)] & (\varepsilon_c - \varepsilon_m)^2 \end{vmatrix}. \tag{2.11}$$

Substituting Eqs. (2.8) - (2.11) into Eq. (2.7), we obtain the dipolar LSPR of the nanorice as:

$$\omega_{1m}^{\pm} = \frac{\omega_p}{\sqrt{2}} \sqrt{\frac{\begin{vmatrix} [2L_s^m\varepsilon_\infty + \varepsilon_m(1 - L_c^m - L_s^m)] & [-L_s^m[L_c^m + f_c(1 - L_s^m)]] \\ (\varepsilon_m + \varepsilon_c - 2\varepsilon_\infty) & 1 \end{vmatrix} \pm \sqrt{\begin{vmatrix} \varepsilon_m(1 - L_c^m) & \varepsilon_c L_c^m \\ L_s^m & 1 - L_s^m \end{vmatrix}^2 + f_c L_s^m(1 - L_s^m) \begin{vmatrix} L_s^m[2L_c^m + f_c(1 - L_s^m)] & -2\varepsilon_m \\ [\varepsilon_m + \varepsilon_c + (L_c^\parallel + L_s^m)(\varepsilon_c - \varepsilon_m)] & (\varepsilon_c - \varepsilon_m)^2 \end{vmatrix}}}{\begin{vmatrix} [\varepsilon_m(1 - L_s^m) + \varepsilon_\infty L_s^m] & -f_c L_s^m(1 - L_s^m) \\ [\varepsilon_\infty(\varepsilon_m + \varepsilon_c - \varepsilon_\infty) - \varepsilon_m\varepsilon_c] & [\varepsilon_\infty(1 - L_c^m) + \varepsilon_c L_c^m] \end{vmatrix}}}, \tag{2.12}$$

where

$$L^0 = [(v \coth^{-1} v) - 1](v^2 - 1),\ L^1 = \tfrac{1}{2}(1 - L^0),\ v = \tfrac{1}{\sqrt{1 - q^{-2}}},\ q > 1,\ f_c = \tfrac{v_c(v_c^2 - 1)}{v_s(v_s^2 - 1)} \quad \text{(Prolate)}, \tag{2.13}$$

$$L^0 = \tfrac{1}{2}[(v^2 + 1)(v \cot^{-1} v) - v^2],\ L^1 = \tfrac{1}{2}(1 - L^0),\ v = \tfrac{1}{\sqrt{q^2 - 1}},\ q > 1,\ f_c = \tfrac{v_c(v_c^2 + 1)}{v_s(v_s^2 + 1)} \quad \text{(Oblate)}. \tag{2.14}$$

Here, L^0 and L^1 are the longitudinal and transverse geometric factors of the spheroid, respectively, q is its aspect ratio, and f_c is the core-volume fraction of the core-shell spheroid. The aspect ratio is evaluated on the core and shell to obtain the values of L^0 and v on the core and shell, respectively, using

$$q_c = \frac{b_c}{a_c},\ b_c > a_c,\ q_s = \frac{b_s}{a_s},\ b_s > a_s,\ q_c > q_s \quad \text{(Prolate)}, \tag{2.15a}$$

$$q_c = \frac{a_c}{b_c},\ b_c < a_c,\ q_s = \frac{a_s}{b_s},\ b_s < a_s,\ q_c > q_s \quad \text{(Oblate)}. \tag{2.15b}$$

Fig. 2.4(a) shows that as the aspect ratio of the core increases, the symmetric (ω_{10}^-) and antisymmetric (ω_{10}^+) modes of the nanorice in the longitudinal polarization ($m = 0$) approach the LSPR of the solid, ω_{10}^s (Eq. (2.20) for $m = 0$), and cavity, ω_{10}^c (Eq. (2.22) for $m = 0$) prolate spheroid plasmons, respectively. The transverse modes ($m = 1$) show a similar trend (Fig. 2.4(b)), but the transverse

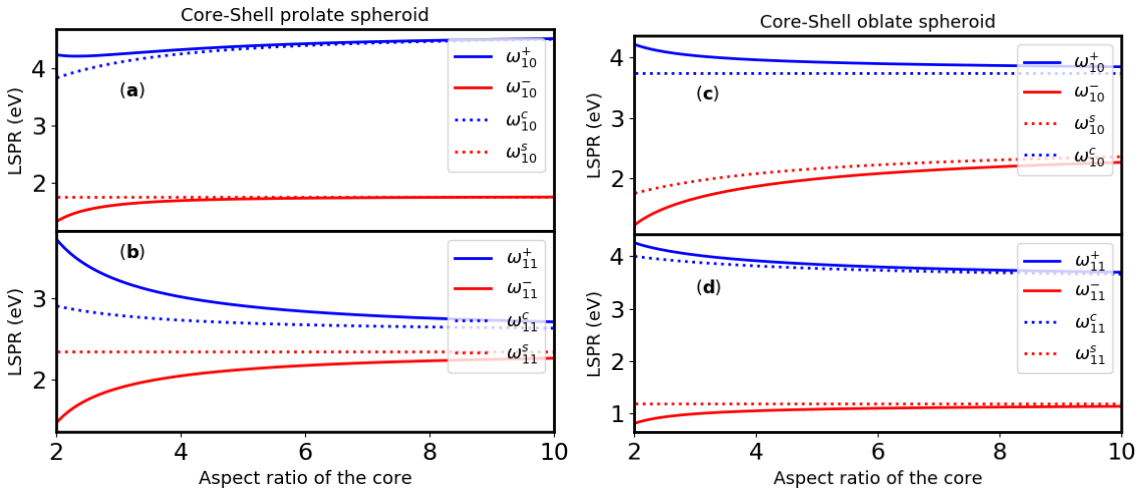

Figure 2.4: Dipolar (a) LLSPR and (b) TLSPR of a gold shell-silica core prolate spheroid, respectively, and dipolar (c) LLSPR and (d) TLSPR of a gold shell-silica core oblate spheroid, respectively, and those of their corresponding core and shell, respectively, using the following parameters: $\omega_p = 4.6$ eV, $\varepsilon_\infty = 1, \varepsilon_c = 2.13$ (silica core), $\varepsilon_m = 1.77$ (water), and $q_s = 1.5$.

symmetric mode (ω_{11}^{-}) is blueshifted from the longitudinal symmetric mode (ω_{10}^{-}) while the transverse antisymmetric mode (ω_{11}^{+}) is redshifted from the longitudinal antisymmetric mode (ω_{10}^{+}). This is because increasing q_c (increasing the prolateness of the core) at a constant q_s causes the core-volume fraction to decrease, i.e., the shells become thicker, and the nanorice plasmons will therefore de-couple into the fundamental plasmons. In a core-shell oblate spheroid, these trends are similar but the energy shifts between the respective modes are different from those of the nanorice, as shown in Fig. 2.4(c) and Fig. 2.4(d), respectively. In addition, as the aspect ratio of the core increases (increasing the oblateness of the core), the symmetric and antisymmetric modes approach the LSPR of the solid and cavity spheroid plasmons, respectively.

The multipolar LSPR of a concentric nanoshell (Fig. 2.3(b)) is obtained via **GR** of Eq. (2.7) by using the spherical limits of the following functions:[74]

$$\left.\frac{Q_{lm}(v)}{P_{lm}(v)}\right|_{v\longrightarrow\infty} = \frac{N_{lm}}{v^{2l+1}}, \qquad \left.\frac{Q'_{lm}(v)}{P'_{lm}(v)}\right|_{v\longrightarrow\infty} = -\frac{N_{lm}}{v^{2l+1}}\left(\frac{l+1}{l}\right), \tag{2.16}$$

where N_{lm} is a normalization constant which cancels out during the simplification of Eq. (2.7) using Eq. (2.16). Here, $v_c = a/f$ and $v_s = b/f$ in the sphere limit. Using these expressions, we obtain the m-independent multipole LSPR of the nanoshell as:

$$\omega_l^{\pm} = \frac{\omega_p}{\sqrt{2}}\sqrt{\frac{\begin{vmatrix} l(l+1) & -[l^2\varepsilon_c + (l+1)^2\varepsilon_m] \\ 1 & [2\varepsilon_\infty + q^{2l+1}(\varepsilon_m + \varepsilon_c - 2\varepsilon_\infty)] \end{vmatrix} \pm \sqrt{\begin{vmatrix} (l+1)^2 & \varepsilon_c \\ l^2 & \varepsilon_m \end{vmatrix}^2 + l(l+1)q^{2l+1}\begin{vmatrix} [l(l+1)q^{2l+1}(\varepsilon_c - \varepsilon_m)^2] & -2 \\ [l\varepsilon_c + (l+1)\varepsilon_m]^2 + \varepsilon_c\varepsilon_m(2l+1)^2 & 1 \end{vmatrix}}}{\begin{vmatrix} [(l+1)\varepsilon_m + l\varepsilon_\infty] & -l(l+1)q^{2l+1} \\ [\varepsilon_\infty(\varepsilon_m + \varepsilon_c - \varepsilon_\infty) - \varepsilon_m\varepsilon_c] & [l\varepsilon_c + (l+1)\varepsilon_\infty] \end{vmatrix}}}, \tag{2.17}$$

which reduces to

$$\omega_1^{\pm} = \frac{\omega_p}{\sqrt{2}} \sqrt{\frac{\begin{vmatrix} 3 & -(1+2f_c) \\ (\varepsilon_m+\varepsilon_c-2\varepsilon_\infty) & (\varepsilon_m+2\varepsilon_\infty) \end{vmatrix} \pm \sqrt{\begin{vmatrix} 4 & \varepsilon_c \\ 1 & \varepsilon_m \end{vmatrix}^2 + 4f_c \begin{vmatrix} (1+f_c) & -3\varepsilon_m \\ (\varepsilon_m+5\varepsilon_c) & (\varepsilon_c-\varepsilon_m)^2 \end{vmatrix}}}{\begin{vmatrix} (2\varepsilon_m+\varepsilon_\infty) & -2f_c \\ [\varepsilon_\infty(\varepsilon_m+\varepsilon_c-\varepsilon_\infty)-\varepsilon_m\varepsilon_c] & (\varepsilon_c+2\varepsilon_\infty) \end{vmatrix}}}, \tag{2.18}$$

in the dipole limit $l = 1$, where $q = a/b$ is its aspect ratio, and $f_c = q^3$ is the core-volume fraction. Eq. (2.18) can also be obtained via **GR** of Eq. (2.12) by setting $L_c^0 = L_s^0 = 1/3$, where $L = 1/3$ is the static geometric factor of an isotropic sphere.[8] Fig. 2.5 shows that an increase in the core aspect ratio q of a

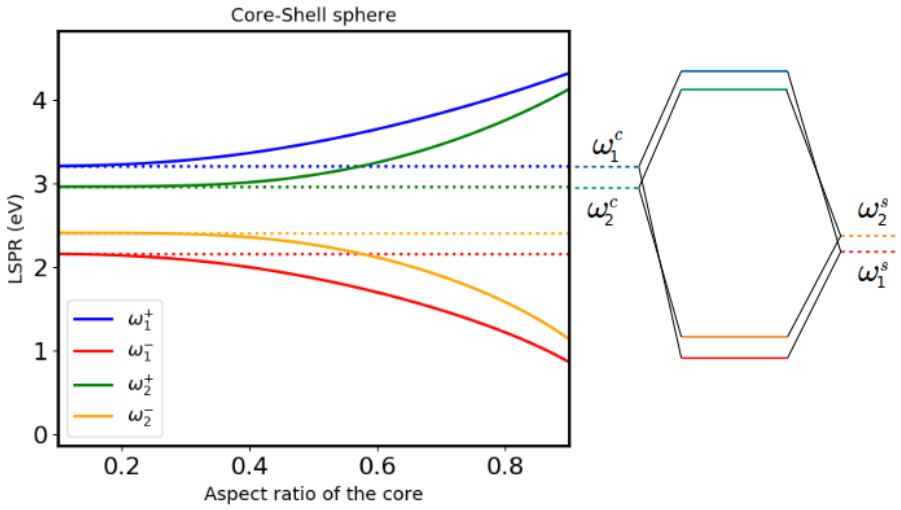

Figure 2.5: Dependence of the dipolar and quadrupolar LSPR of a concentric gold nanoshell on the aspect ratio of the core, using the following parameters: $\omega_p = 4.6$ eV, $\varepsilon_\infty = 1, \varepsilon_c = 2.13$ (silica core), $\varepsilon_m = 1.77$ (water). Dashed lines show the dipolar and quadrupolar LSPR of solid and cavity nanospheres, respectively. Appended to the right is the plasmon hybridization diagram of the dipolar ($l = 1$) and quadrupolar ($l = 2$) modes, respectively.

concentric nanoshell, i.e., thinning of the shells, causes a redshift in the symmetric modes (ω_l^-) and a blueshift in the antisymmetric modes (ω_l^+), while a decrease in the core aspect ratio, i.e., thickening of the shells, causes the hybrid modes to approach the LSPR of the corresponding solid (ω_l^s) and cavity (ω_l^c) sphere plasmons, respectively. For $l \geq 2$ (higher-order modes), ω_l^s and ω_l^- both undergo a blueshift, while ω_l^c and ω_l^+ both undergo a redshift, as q increases, with respect to the LSPR of the dipolar mode, as shown in Fig. 2.5. The plasmon hybridization diagram indicates the different energy shifts in the LSPR of the nanoshell, for the dipolar ($l = 1$) and the quadrupolar ($l = 2$) modes, respectively.

2.2.2 *Fundamental Plasmons*

In this section, we will derive the LSPR of solid and cavity spheroids (Figs. 2.3(c) and (e), respectively), as well as those of solid and cavity spheres (Figs. 2.3(d) and (f), respectively), from the LSPR of the core-shell MNPs, using the relationships in Fig. 2.2. Solid prolate spheroids are sometimes referred to as nanorods,[8,69] while solid oblate spheroids are also known as nanodisks[70] or platelets.[7] The plasmonic modes of these nanocavities and solid MNPs can be referred to as the *fundamental plasmon modes*, due to their role in plasmon hybridization.[64,69]

To obtain the LSPR of these fundamental plasmons from those of the corresponding core-shell geometries, we made use of the fact that in concentric/confocal core-shell MNPs,[64,69] the antisymmetric mode is formed from antisymmetric coupling of solid and cavity plasmons of the same angular momentum number l, while the symmetric mode is formed via symmetric coupling of similar solid and cavity plasmons. This is explained in detail in Section 2.2.3. Here, we show that an antisymmetric de-coupling of the symmetric and antisymmetric modes in the core-shell MNPs leads to the LSPR of the cavity or void plasmons, while a symmetric de-coupling of the symmetric and antisymmetric modes leads to the LSPR of the solid plasmons. We have chosen to refer to the latter as Symmetrization (**S**), and the former as Anti-Symmetrization (**AS**). The LSPR of these fundamental MNPs are well-known but we present them to show that they can alternatively be obtained using the relationships we proposed in Fig. 2.2.

To de-couple the hybrid plasmon modes, we need to find the coupling constants responsible for hybridization of the fundamental modes. We found that the quantity Ω, defined in Eq. (2.6c), plays the role of the coupling constant between the void and solid plasmons of the core-shell spheroid in the multipole limit. This is because it is proportional to the core-volume fraction of the spheroid. Thus, by setting $\Omega = 0$ in the symmetric mode (ω_{lm}^{-}) of Eq. (2.7), and making use of Eqs. (2.6a)–(2.6c), one obtains the multipole LSPR of the solid prolate spheroid (Fig. 1.10(c)) as:

$$\begin{aligned}\omega_{lm}^{s} &= \omega_{lm}^{-}(\Omega = 0) \\ &= \omega_p \sqrt{\frac{P'_{lm}(v_s)Q_{lm}(v_s)}{\varepsilon_\infty P'_{lm}(v_s)Q_{lm}(v_s) - \varepsilon_m P_{lm}(v_s)Q'_{lm}(v_s)}}.\end{aligned} \tag{2.19}$$

However, in the dipole limit, the core-volume fraction f_c plays the role of the coupling constant. This is because by setting $f_c = 0$ in the symmetric dipolar mode (ω_{1m}^{-}) of Eq. (2.12), the dipolar LSPR of the solid prolate spheroid (also the dipole limit of Eq. (2.19)) is found as:

$$\begin{aligned}\omega_{1m}^{s} &= \omega_{1m}^{-}(f_c = 0) \\ &= \omega_p \sqrt{\frac{L_s^m}{\varepsilon_\infty L_s^m + \varepsilon_m\left(1 - L_s^m\right)}}.\end{aligned} \tag{2.20}$$

These two processes correspond to **S**.

In the case of a cavity spheroid (Fig. 1.10(e)), **DR** can be used to obtain its LSPR.[1] To do this, the expression obtained for $\Re[\varepsilon(\omega_r)]$ in the case of a solid prolate spheroid is used, but the positions of the dielectric constants are reversed. Also, ε_m is replaced with ε_c, and v_s with v_c to obtain a new expression for $\Re[\varepsilon(\omega_r)]$ (see Appendix F), which is substituted in Eq. (2.4) to give the multipole LSPR of the cavity prolate spheroid, or via **AS** of Eq. (2.7), i.e, by setting $\Omega = 0$ in the antisymmetric mode (ω_{lm}^{+}) of Eq. (2.7), to obtain:

$$\begin{aligned}\omega_{lm}^{c} &= \omega_{lm}^{+}(\Omega = 0) \\ &= \omega_p \sqrt{\frac{P_{lm}(v_c)Q'_{lm}(v_c)}{\varepsilon_\infty P_{lm}(v_c)Q'_{lm}(v_c) - \varepsilon_c P'_{lm}(v_c)Q_{lm}(v_c)}}.\end{aligned} \tag{2.21}$$

The dipole limit of Eq. (2.21) can be obtained via **AS** of Eq. (2.12), i.e, by setting $f_c = 0$ in the antisymmetric mode (ω_{1m}^{+}) of Eq. (2.12), to obtain:

$$\begin{aligned}\omega_{1m}^{c} &= \omega_{1m}^{+}(f_c = 0) \\ &= \omega_p \sqrt{\frac{1 - L_c^m}{\varepsilon_\infty\left(1 - L_c^m\right) + \varepsilon_c L_c^m}}.\end{aligned} \tag{2.22}$$

For a solid sphere (Fig. 1.10(d)), we performed **S** on Eq. (2.17) to obtain its LSPR. In the multipole limit, the aspect ratio q of the nanoshell plays the role of the coupling constant between the solid and cavity sphere plasmons. Thus, by setting $q = 0$ in the symmetric mode (ω_l^{-}) of Eq. (2.17), the multipole LSPR of a solid sphere is found as:

$$\begin{aligned}\omega_l^{s} &= \omega_l^{-}(q = 0) \\ &= \omega_p \sqrt{\frac{l}{l\varepsilon_\infty + (l+1)\varepsilon_m}}.\end{aligned} \tag{2.23}$$

Here, Eq. (2.23) can also be obtained from the sphere limit of Eq. (2.19). The dipole limit of Eq. (2.23) can be obtained by simply setting $l = 1$ in Eq. (2.23), or by performing **S** on Eq. (2.18). Here, the core-volume fraction f_c, which plays the role of the coupling constant between the solid and cavity sphere plasmons, has to be set to zero. Also, **GR** can be used by setting $L_s^m = 1/3$ in Eq. (2.20), to obtain:

$$\begin{aligned}\omega_1^{s} &= \omega_1^{-}(f_c = 0) \\ &= \omega_p \sqrt{\frac{1}{\varepsilon_\infty + 2\varepsilon_m}}.\end{aligned} \tag{2.24}$$

Likewise, **DR** can be used to obtain the LSPR of a cavity sphere (Fig. 1.8(f)). To do this, the expression obtained for $\Re[\varepsilon(\omega_r)]$ in the case of a solid sphere is used, but the positions of the dielectric constants are reversed, and ε_m is replaced with ε_c, to yield an expression for $\Re[\varepsilon(\omega_r)]$ (see Appendix F), which is substituted

in Eq. (2.4), to obtain the multipole LSPR of the cavity sphere, or via the sphere limit of Eq. (2.21) to obtain:

$$\begin{aligned}\omega_l^c &= \omega_l^+(q=0)\\ &= \omega_p\sqrt{\frac{l+1}{l\varepsilon_c+(l+1)\varepsilon_\infty}}.\end{aligned} \tag{2.25}$$

However, Eq. (2.25) can also be obtained by performing **AS** on Eq. (2.17), i.e., by setting $q=0$ in the antisymmetric mode (ω_l^+) of Eq. (2.17). The dipole limit of Eq. (2.25) can be obtained by simply setting $l=1$, or by performing **AS** on Eq. (2.18), or by using **GR**, i.e., by setting $L_c^m = 1/3$ in Eq. (2.22), all giving:

$$\begin{aligned}\omega_1^c &= \omega_1^+(f_c=0)\\ &= \omega_p\sqrt{\frac{2}{\varepsilon_c+2\varepsilon_\infty}}.\end{aligned} \tag{2.26}$$

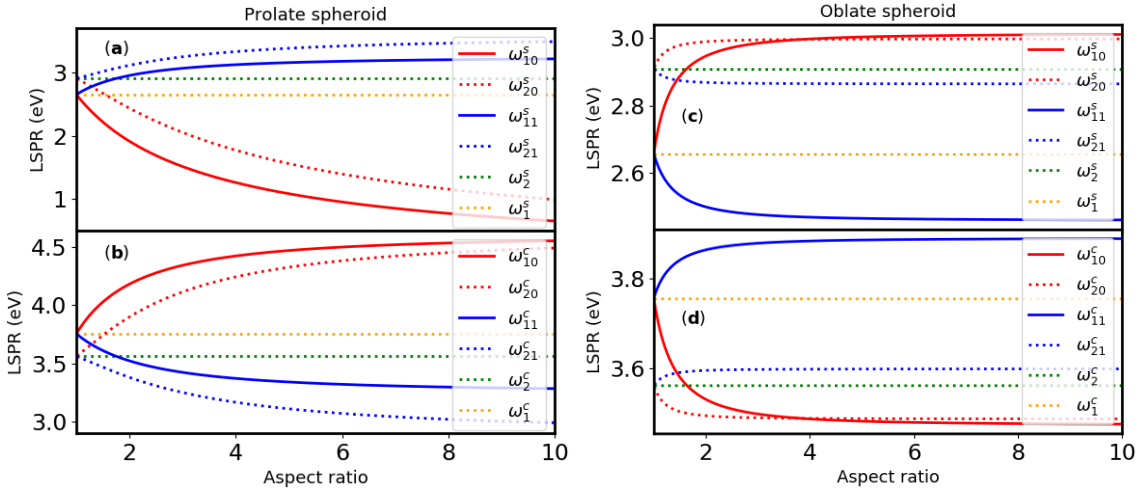

Figure 2.6: Dipolar and quadrupolar LSPR of: (a) solid and (b) cavity prolate gold spheroids, respectively, (c) solid and (d) cavity oblate gold spheroids, respectively, and those of solid and cavity gold spheres, using the following parameters: $\omega_p = 4.6$ eV, $\varepsilon_\infty = \varepsilon_c = \varepsilon_m = 1.0$.

In Fig. 2.6, increasing the aspect ratio of a prolate spheroid causes a redshift in both the longitudinal ($m=0$) dipolar ($l=1$) LSPR of the solid spheroid (ω_{10}^s, Fig. 2.6(a)) and the transverse ($m=1$) dipolar LSPR of the cavity spheroid (ω_{11}^c, Fig. 2.6(b)). Conversely, the transverse LSPR of the solid spheroid (ω_{11}^s, Fig. 2.6(a)) and the longitudinal LSPR of the cavity spheroid (ω_{10}^c, Fig. 2.6(b)) are both blueshifted. The LSPR of the quadrupolar modes ($l=2$) follow similar trends (Fig. 2.6(a) and Fig. 2.6(b), respectively). However, with respect to the dipolar modes, ω_{20}^s is blueshifted while ω_{20}^c is redshifted. On the other hand, ω_{21}^c is blueshifted while ω_{21}^s is redshifted, with respect to the dipolar modes. Fig. 2.6(c) and Fig. 2.6(d) show that these trend are reversed in an oblate spheroid, i.e., increasing the aspect ratio of the spheroid affects the longitudinal dipolar

LSPR of the solid spheroid (ω^s_{10}, Fig. 2.6(c)) and the transverse dipolar LSPR (ω^c_{11}, Fig. 2.6(c)) of the cavity spheroid in the same manner, (i.e., causing a blueshift), while the transverse LSPR of the solid spheroid (ω^s_{11}, Fig. 2.6(c)) and the longitudinal LSPR of the cavity spheroid (ω^c_{10}, Fig. 2.6(c)) are both redshifted. Quadrupolar modes ($l = 2$) follow similar trends, but as also shown in Fig. 2.6(c) and Fig. 2.6(d), the QSA fails to properly replicate the expected converse trends around $q \geq 4$, for the longitudinal solid and cavity oblate spheroids, respectively. However, as $q \longrightarrow 1$, the LSPR of the solid and cavity spheroids approach the LSPR of the solid (ω^s_1) and cavity (ω^c_1) sphere, respectively. A comparison of these plots (Figs. 2.6(a) and (b) and Figs. 2.6(c) and (d)) shows that the longitudinal LSPR of the solid oblate spheroid is blueshifted from that of the solid prolate spheroid, while the transverse LSPR of the solid oblate spheroid is redshifted from that of the solid prolate spheroid, as their aspect ratios increase. The LSPR of the cavity spheroids show a converse trend. In addition, the longitudinal LSPR of the spheroids (ω^s_{l0} and ω^c_{l0}) are more sensitive to changes in the aspect ratio compared to their transverse counterparts (ω^s_{l1} and ω^c_{l1}).

2.2.3 *Plasmon Hybridization in a Nanorice*

In this section, we constructed a simple model of plasmon hybridization in a nanorice, in the dipole limit. In core-shell MNPs, void plasmons couple to solid plasmons to form hybrid plasmons, through the core volume fraction f_c, which plays the role of the coupling constant in the dipole limit. This phenomenon is known as *plasmon hybridization*.[13,64] We used this model to justify the de-coupling of the hybrid plasmon modes through $f_c = 0$, to form the fundamental plasmon modes, as a part of the **S** and **AS** methods we have employed in Section 2.2.2. For brevity, we only considered the case: $\varepsilon_m = \varepsilon_c = \varepsilon_\infty = 1$. We started with a nanorice since it can be transformed to a core-shell oblate spheroid or reduced to a concentric nanoshell.

Consider a solid prolate spheroid and a cavity prolate spheroid with dimensions as given in Section 2.2.1, but with $q_c > q_s$. When these two nanostructures couple to form a nanorice, the core-volume fraction of the nanorice is f_c as given in Section 2.2.1. From Eq. (2.12), we obtain the following normal modes of the plasma oscillations in the nanorice:

$$\omega^2_\pm = \frac{1}{2}\left[(\omega^2_c + \omega^2_s) \pm (\omega^2_c - \omega^2_s)\sqrt{1 + \frac{4f_c L_s(1 - L_s)}{(1 - L_c - L_s)^2}}\right] \tag{2.27}$$

for the longitudinal polarization ($m = 0$), where ω_c and ω_s are the longitudinal dipolar LSPR of the cavity and solid prolate spheroid, respectively, and L_c and L_s are the longitudinal static geometric factors of evaluated at the core and at the shell surfaces, respectively, for which the superscript "0" has been dropped. We constructed a simple model of plasmon hybridization by assuming that the cavity plasmons couple weakly to the solid plasmons in the nanorice. This

weak-coupling regime corresponds to $f_c < (1 - L_c - L_s)^2/4L_s(1 - L_s)$, where the antisymmetric and symmetric modes are obtained from Eq. (2.27) as:

$$\omega_+^2 \approx \omega_c^2 + f_c \left(\frac{1-L_s}{1-L_c-L_s}\right)\left[\omega_s^2 - f_c\omega_c^2\left(\frac{L_s}{1-L_c-L_s}\sqrt{\frac{1-L_s}{1-L_c}}\right)^2\right] \tag{2.28}$$

and

$$\omega_-^2 \approx \omega_s^2 - f_c \left(\frac{1-L_s}{1-L_c-L_s}\right)\left[\omega_s^2 - f_c\omega_c^2\left(\frac{L_s}{1-L_c-L_s}\sqrt{\frac{1-L_s}{1-L_c}}\right)^2\right], \tag{2.29}$$

respectively, up to second order in f_c. We observe that the higher-energy antisymmetric plasmon mode ω_+, is formed via a blueshift in the cavity plasmon mode ω_c, as a result of coupling with the solid plasmon, while the lower-energy symmetric plasmon mode ω_-, is formed via a redshift in the solid plasmon mode ω_s, as a result of coupling with the cavity plasmon, as revealed by both Eq. (2.28) and Eq. (2.29), as well as the plasmon hybridization diagram in Fig. 2.7.

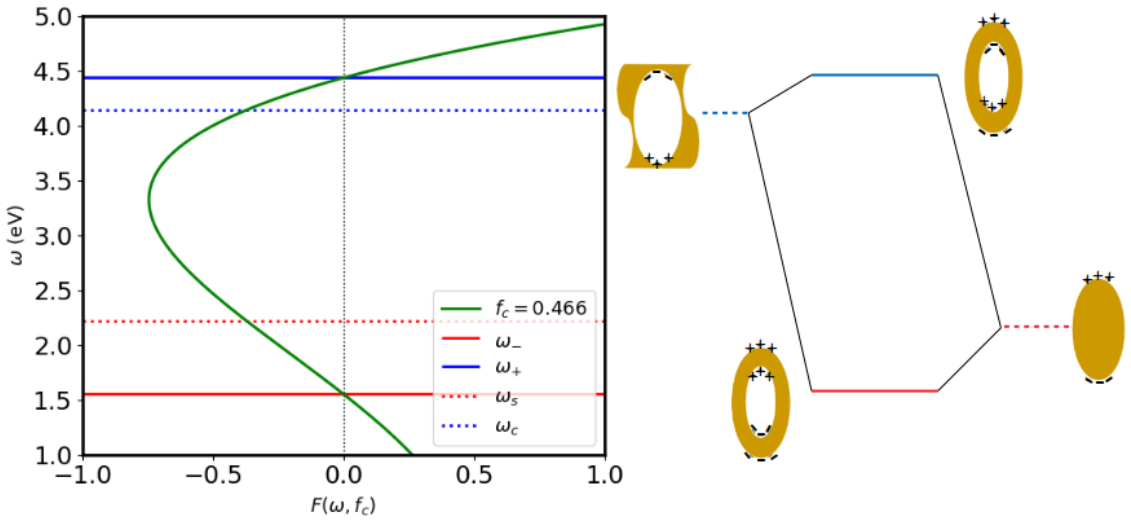

Figure 2.7: Graphical solution of the Fröhlich function $F(\omega, f_c)$, for a gold nanorice with dimensions: $q_s = 1.5$ and $q_c = 1.839$. The plasmon hybridization diagram and the distribution of surfaces charges for the different plasmon modes are shown on the right.

Using ω_+^2 and ω_+^2, we construct a function, $F(\omega, f_c) = \omega^4 - \omega^2(\omega_+^2 + \omega_-^2) + \omega_+^2\omega_-^2$, which we refer to as the "Fröhlich function", in order to better understand the weak coupling of fundamental plasmon modes in a nanorice. For a nanorice of aspect ratio $q_s = 1.5$, and core aspect ratio $q_c = 1.839$, we obtain an upper bound of $f_c = 0.466 = (1 - L_c - L_s)^2/4L_s(1 - L_s)$ in the weak-coupling regime ($f_c < 0.466$ for this nanorice geometry). The zeros of $F(\omega, 0.466)$ are $\omega_- = 1.53$ eV and $\omega_+ = 4.43$ eV at the LSPR ($F(\omega = \omega_r, f_c) = 0$), for the longitudinal polarization, $m = 0$. The function has a minimum at $\omega = \omega_p\sqrt{1 - L_c + L_s}/\sqrt{2}$. Here, Eqs. (2.28) and (2.29) predict $\omega_- = 1.62$ eV and $\omega_+ = 4.41$ eV, respectively. The zeros of $F(\omega, f_c < 0.466)$ will therefore approach ω_s and ω_c, respectively. The distribution of surface charges shown in the plasmon hybridization diagram

appended to Fig. 2.7, shows that surface charges align in the same direction in the solid and cavity plasmons to form the symmetric mode, while the reverse occurs in the case of the antisymmetric mode.

In the sphere limit, $L_c = L_s = 1/3 \Rightarrow f_c < 1/8$. Hence, when $\varepsilon_m = \varepsilon_c = \varepsilon_\infty = 1$, the coupling constant of solid and cavity plasmons in a concentric nanoshell has an upper bound that is independent of the aspect ratio of the nanoshell, below which the fundamental plasmons are weakly coupled. However, in core-shell spheroids, the weak coupling regime of solid and cavity plasmons has an upper bound that depends on the aspect ratios of the core and the core-shell, via L_c and L_s, respectively. However, this result is only valid for MNP sizes within the QSA, where the LSPR of solid and void sphere plasmons are independent of the sphere size, provided that the coupling constant is weak.

2.3 PLASMONIC DIMERS

Plasmonic dimers consist of two MNPs which interact with each other in the presence of an applied electromagnetic field to form hybrid plasmon modes.[18,19,75] The optical response of a MNP dimer can be investigated using a dipolar quasi-static approach, provided that the MNP sizes and the inter-particle distance are small compared to the wavelength of light in the medium.[19,76,77] The above conditions ensure that the contributions from higher-order modes are negligible, and can therefore be ignored. These conditions also one to ignore radiation damping, the spatial variation of the incident electric field, and the wavenumber-dependent terms in the induced field on each particle.[19,76] This approach has been shown to agree with experiments involving small MNPs less than 30 nm in radius.[19,65] Beyond such sizes, the quasi-static model is not valid.[8,65] The method also requires that the nanoparticles are such that the probability of electrons tunnelling through the dimer gap is zero. Esteban et al.[53] have shown that the probability for quantum tunnelling is negligible in dimer gaps greater than or equal to 0.5 nm (Fig. 1.3(b)), so that classical methods are valid in this regime. In addition, the local electric field, $\mathbf{E}_{loc}$, on each MNP in the dimer is represented as that of an induced electric dipole, $\mathbf{E}_{ind}$, at the centre of the other particle, and the external field, $\mathbf{E}_0$, applied to the dimer.[19] This is used to find the effective quasi-static dipole polarizability of the dimer for a given incident field polarization.[19,76]

The optical properties of MNP dimers, such as nanosphere (NS) dimers,[53,78–80] nanorod (NR) dimers,[75,80,81] concentric nanoshell dimers,[82,83] NS-concentric nanoshell dimers,[18,19] pairs of cavity resonance based plasmonic nanoantennas,[84] and nanowire dimers[65,85] have been widely studied in plasmonic literature. While significantly more strongly enhanced near-fields have been reported to exist in dimer gaps,[53,84,86,87] the spectra of dimers also differ from those of single nanoparticles, predominantly because they feature incident electric field polarization-dependent response, plasmon-induced resonance shifts, and plasmon-induced transparency (PIT) regions.[18,75,78] These dimers are generally classified as either homo– or heterodimers.

2.3.1 *Homo– and Heterodimers*

Homodimers are formed from two MNPs of the same size, geometry, orientation, and material composition.[21,65,75] For a given incident field polarization, the optical response of such dimers, usually features one dipolar plasmon bonding mode (within the dipole-dipole coupling limit), where plasmon coupling results in a shift in the dipolar LSPR of the MNP.[21] On the other hand, heterodimers are formed from two MNPs with different sizes,[18] geometry,[17] orientation,[80] and/or material composition.[19] Unlike homodimers, plasmon coupling in heterodimers can lead to the formation of one or more dipolar plasmon bonding modes,[17–19] for a given incident field polarization.

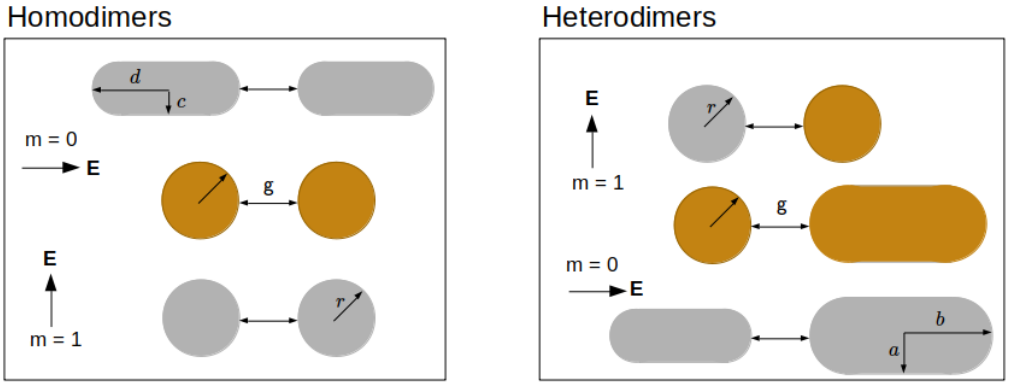

Figure 2.8: Examples of homo– and heterodimers of gold (golden) and silver (grey) nanospheres and nanorods.

Fig. 2.8 shows the arrangement of some common homo– and heterodimers. Let g denote the surface to surface distance between any pair of nanoparticles shown in Fig. 2.8, and let r denote the radius of the NS. Then the centre to centre distance is $l = g + 2r$. The longitudinal dipole polarizability (due to an incident field parallel to the dimer axis, $m = 0$) and the transverse dipole polarizability (due to an incident field perpendicular to the dimer axis, $m = 1$) of the dimer are respectively[21,76] (also see appendix F):

$$\alpha^m = 2\alpha_{ns} \frac{\left[1 + (\frac{-1}{2})^m \frac{\alpha_{ns}}{2\pi l^3}\right]}{1 - \left(\frac{\alpha_{ns}}{2^{m+1}\pi l^3}\right)^2}, \tag{2.30}$$

where $\alpha_{ns} = 4\pi r^3[\varepsilon(\omega) - \varepsilon_m]/[\varepsilon(\omega) + 2\varepsilon_m]$[19] is the static dipole polarizability of the NS. Applying the Fröhlich condition to Eq. (2.30) leads to $\alpha_{ns}/2^{m+1}\pi l^3 = \pm 1$, from which $\Re[\varepsilon(\omega)]$ is obtained. Let ω_m denote the LSPR of the homodimer. It is derived by substituting the expression for $\Re[\varepsilon(\omega)]$ into Eq. (2.4), to obtain:

$$\omega_m = \omega_s \sqrt{\frac{1 + \nu_m}{1 + \epsilon\nu_m}}, \quad \nu_m = \pm(2^{1-m})\left(\frac{r}{l}\right)^3, \tag{2.31}$$

where ω_s is the dipolar LSPR of the solid sphere (Eq. (2.24)), ν_m are the dipole orientation-dependent coupling constants of the solid sphere dipole plasmons,

and $\epsilon = (\varepsilon_\infty - \varepsilon_m)/(\varepsilon_\infty + 2\varepsilon_m)$. At constant values of r, $\nu_m \longrightarrow 0$ as $g \longrightarrow \infty$, so that Eq. (2.31) reduces to Eq. (2.24).

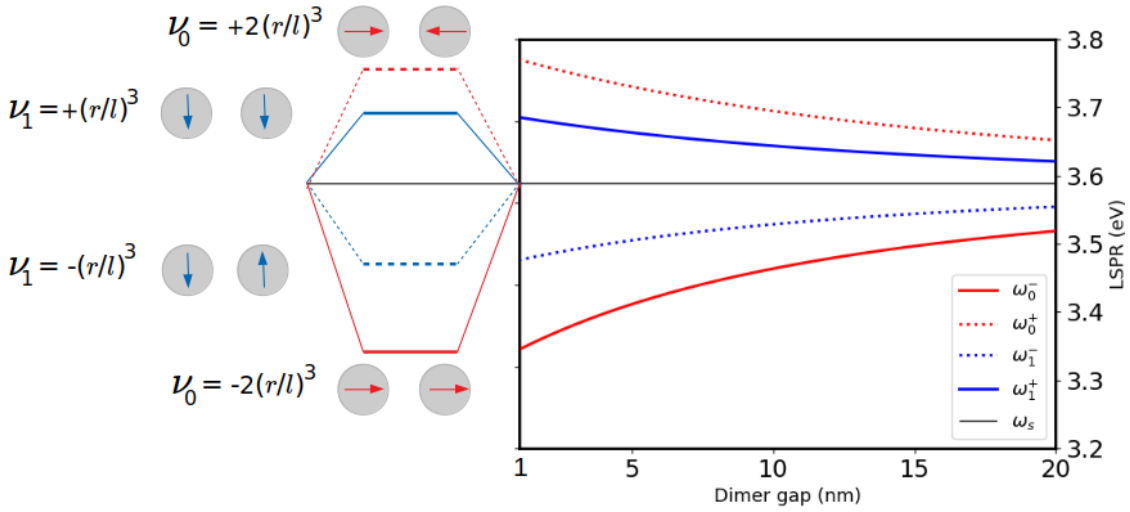

Figure 2.9: Dependence of the LSPR of a silver NS homodimer on the dimer gap. On the left is the plasmon hybridization diagram showing the positions of the LSPR, the coupling constants, and the direction of the induced dipole field in each NS (as indicated by the arrows). (Reproduced for silver from Ref.[21] based on the Drude model, with $r = 20$ nm, and $\varepsilon_m = 1$.)

In Fig. 2.9, dipolar solid plasmons of the NS align in different directions to form new dipolar modes. Plasmon coupling in the NS homodimer depends on the coupling constant, ν_m. When the direction of the induced dipole field in each NS is the same, dipoles parallel to the dimer axis form a lower-energy hybrid plasmon mode (ω_0^-), due to a decrease in the coupling constant, while dipoles perpendicular to the dimer axis form a higher-energy hybrid plasmon mode (ω_1^+), due to an increase in the coupling constant (Fig. 2.9). Here, we represent these modes with solid lines, since the extinction spectra of the dimer usually feature these two configurations (Fig. 2.10(a)), as demonstrated experimentally in Ref.[18,19] The other two configurations, which are not so common experimentally, involve induced dipole fields in opposite directions (Fig. 2.9, dashed lines). In this case, dipoles parallel to the dimer axis form a higher-energy hybrid plasmon mode (ω_0^+), due to an increase in the coupling constant, while dipoles perpendicular to the dimer axis form a lower-energy hybrid plasmon mode (ω_1^-), due to a decrease in the coupling constant (Fig. 2.9). The respective hybrid modes approach that of the NS (ω_s) at large values of r, as a result of weak coupling.

Let d and c denote the half-length and half-width of a prolate spheroid, respectively, and let b and a denote the half-length and half-width of a nearby prolate spheroid, respectively, as shown in Fig. 2.8. If we approximate each

spheroid to a NR, then the effective longitudinal dipole polarizability of the NR dimer is (see Appendix F):

$$\alpha_{eff} = \frac{\alpha_1 + \alpha_2 + \frac{3\alpha_1\alpha_2}{4\pi l}\left[\frac{1-L_{\mu 1}}{(l^2-f_1^2)} + \frac{1-L_{\mu 2}}{(l^2-f_2^2)}\right]}{1 - \frac{9\alpha_1\alpha_2(1-L_{\mu 1})(1-L_{\mu 2})}{(4\pi l)^2(l^2-f_1^2)(l^2-f_2^2)}}, \tag{2.32}$$

where $f_1^2 = d^2 - c^2$ and $f_2^2 = b^2 - a^2$ are the squares of the focal lengths of the first and second NR, respectively, $l = d + g + b$ is the centre to centre distance, $L_{\mu 1}$ is the longitudinal static geometric factor of the dimer due to the first NR, L_{v2} is the longitudinal static geometric factor of the dimer due to the second NR, $\mu_1 = l/f_1$ and $\mu_2 = l/f_2$ are the corresponding radial coordinates of the dimer, α_1 and α_2 are respectively the static dipole polarizabilities of the first and second NR. Here, $\alpha_i = V_i[\varepsilon(\omega) - \varepsilon_m]/[\varepsilon_m + L_i[\varepsilon(\omega) - \varepsilon_m]]$, with $V_1 = 4\pi dc^2/3$ and $V_2 = 4\pi ba^2/3$, L_1 and L_2 are the longitudinal static geometric factors of the first and second NR, respectively. If the nearby spheroid is replaced by a NS of radius r, the effective longitudinal dipole polarizability of the NS-NR dimer becomes:

$$\alpha_{eff} = \frac{\alpha_{ns} + \alpha_{nr} + \alpha_{ns}\alpha_{nr}\left[\frac{1}{2\pi l^3} + \frac{3(1-L_l)}{4\pi l(l^2-f^2)}\right]}{1 - \frac{3\alpha_{ns}\alpha_{nr}(1-L_l)}{2(2\pi l^2)^2(l^2-f^2)}}, \tag{2.33}$$

where $l = r + g + d$ is the centre to centre distance, f is the focal length of the NR, α_{nr} is the static dipole polarizability of the NR, and L_l is the static geometric factor of the NS-NR system.

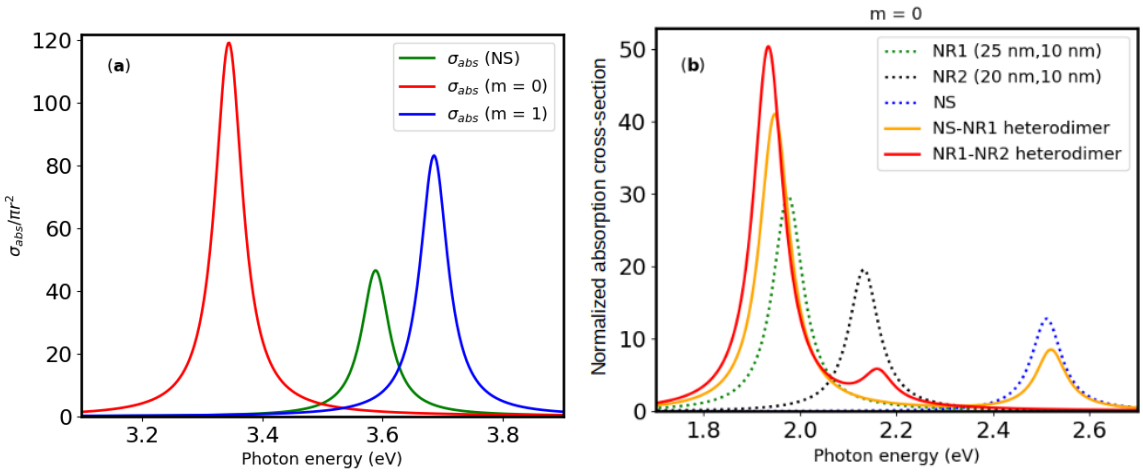

Figure 2.10: (a) Normalized absorption cross-sections of the silver NS homodimer in Fig. 2.8, and (b) Normalized absorption cross-sections of gold NS-NR heterodimer, gold NR heterodimer, and those of the single MNPs, with water, $\varepsilon_m = 1.77$, as the host medium.

In the homodimers in Fig. 2.8(a), only one hybrid dipolar mode is possible for each direction of the incident field (Fig. 2.10(a)), while two hybrid dipolar modes are possible in heterodimers (Fig. 2.10(b)). Fig. 2.10(a) also shows that the absorption cross-section is enhanced when the incident field is parallel to the dimer axis ($m = 0$), as well as when the incident field is perpendicular to the

dimer axis ($m = 1$), but mostly for the former. In addition, the plasmon peak position of the hybrid mode in the case of $m = 0$ is redshifted from that of the isolated NS while the plasmon peak position of the hybrid mode in the case of $m = 1$ is blueshifted from that of the isolated NS. These behaviours have also been reported in Refs.[18,19,65,88]

In Fig. 2.10(b), plasmon coupling between two gold nanorods, NR1 of dimension: (d, c) = (25 nm,10 nm), and NR2 of dimension: (b, a) = (20 nm,10 nm), leads to the formation of two dipolar hybrid modes. The lower-energy hybrid mode is due to a redshift in the plasmon peak position of NR1, while the higher-energy hybrid mode is due to a blueshift in the plasmon peak position of NR2 (Fig. 2.10(b)). Similarly, plasmon coupling between NR1 and a gold NS of radius $r = 20$ nm, leads to the formation of a lower-energy hybrid mode, which is due to a redshift in the plasmon peak position of NR1, and a higher-energy hybrid mode, which is due to a blueshift in the plasmon peak position of the NS (Fig. 2.10(b)). In each of the above cases, the cross-section of the dimer is partly enhanced (due to the redshifted mode) and partly reduced (due the blueshifted mode), compared to the cross-section of the isolated MNP. The regions in the absorption spectra, between 2.1 eV and 2.4 eV for the NS-NR1 dimer, and around 2.1 eV for the NR1-NR2 dimer, where the cross-sections are significantly reduced compared to the rest of the spectra, are known as *plasmon-induced transparency dips*.[89]

2.3.2 *A Nanoegg-Nanorod Dimer* [2]

Reduced-symmetry metal–dielectric nanoparticles such as nanoeggs[13,14] possess great LSPR tunability due to their ability to support the plasmon hybridization of solid and void plasmons with both the same and different angular momentum numbers.[13,14] Engineered primarily by off-setting the core of a concentric nanoshell, this symmetry-breaking property of nanoeggs enables the manifestation of dipole-active modes[15,66] in their extinction spectra. In addition, a typical nanoegg (NE) absorption spectrum, based on the two lowest-order plasmonic modes (the dipole and the quadrupole modes), features a plasmon-induced transparency (PIT) dip,[71] also known as a Fano dip.[17,71] This is a region of reduced or zero absorption as a result of dipole–quadrupole plasmon coupling.[71]

Likewise, the aspect ratio of a nanorod (NR) enables its LSPR to be tuned with great sensitivity along the long axis.[21,22,27,56,91] Both the dipolar LSPR of a NE[66,71] and longitudinal dipolar LSPR of a NR[10,12,27,91] have a common property, namely a redshift in their LSPR with an increase in their respective asymmetry parameters, i.e., the aspect ratio of the NR and the core-offset of the NE. When these two MNPs are spatially separated by a small gap, a NE-NR heterodimer is formed. Although nanoeggs are more complicated to fabricate than concentric nanoshells, they can be synthesized via wet chemistry methods, as demonstrated in Refs.[13,14] Thus, it is feasible to synthesize the proposed dimer. A heterodimer similar to the one proposed here, where a gold nanosphere (NS)

[2] Most of this section is part of the publication in Ref.[90]

was used to modify the optical spectra of a gold NR, was studied in Ref.[17] The

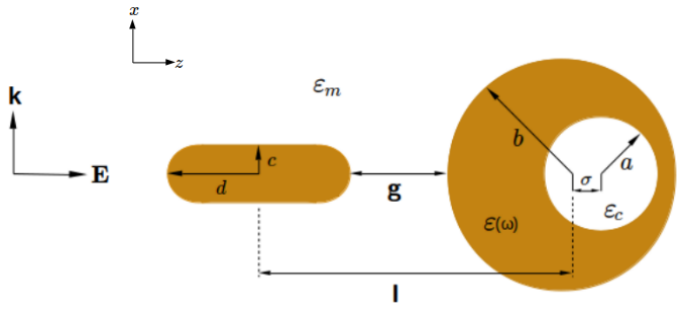

Figure 2.11: Model geometry of the NE–NR dimer. The dimer is surrounded by a homogeneous dielectric medium of dielectric constant ε_m. The NR is modelled as a prolate gold spheroid in the presence of a uniform electric field $\mathbf{E}$ polarized in the z-direction, with a propagation wavevector $\mathbf{k}$ in the x-direction. The NE consists of a gold shell of dielectric constant $\varepsilon(\omega)$, an off-centre silica core of dielectric constant ε_c, and a core-offset σ, in the positive z-direction. The surface-to-surface distance is $\mathbf{g} = g\hat{z}$, and the centre-to-centre distance is $\mathbf{l} = l\hat{z}$.

aim of this study is to investigate the effect of plasmon coupling on the optical properties of a NE-NR heterodimer as the longitudinal LSPR of the NR is tuned via its size. We chose to study a NE since, unlike the concentric nanoshell, the LSPR of a NE can be tuned at constant particle size via its core-offset.[13,14] We studied small nanorods to ensure that only dipolar NR plasmons, which can be fully described via a quasi-static approach, are considered. Likewise, radiation broadening of the scattering and absorption spectra,[22,65] due to radiation of incident light as the particle sizes become comparable to the wavelength of light in the medium, is avoided. The optical properties studied in this work include the effective scattering and absorption spectra of the NE-NR dimer, as well as the characteristics of such hybrid spectra. We approximated the NR to a solid prolate spheroid, a usual practice in analytical models.[77] A uniform electric field, parallel to the dimer axis, polarizes the NR along its long axis in the direction of the core-offset of the NE, as shown in Fig. 2.11. An incident field perpendicular to the dimer axis will polarize the NR along its short axis and the NE across its core-offset. Since these transverse LSPRs have poor tunabilities compared to their longitudinal counterparts,[12–14,91] this incident field direction will not be considered.

For the NE-NR dimer, with $\mathbf{E}_0$ parallel to the dimer axis, as shown in Fig. 2.11, we obtain the effective quasi-static dipole polarizability of the NE, the NR, and that of the dimer as follows:[90]

$$\alpha_{NE}^{eff} = \alpha_{NE}\left[1 + \frac{3\alpha_{NR}[1 - L(v_2)]}{4\pi l(l^2 - f^2)}\right]\left[1 - \frac{3\alpha_{NR}\alpha_{NE}[1 - L(v_2)]}{2(2\pi l^2)^2(l^2 - f^2)}\right]^{-1}, \tag{2.34}$$

$$\alpha_{NR}^{eff} = \alpha_{NR}\left[1 + \frac{\alpha_{NE}}{2\pi l^3}\right]\left[1 - \frac{3\alpha_{NR}\alpha_{NE}[1 - L(v_2)]}{2(2\pi l^2)^2(l^2 - f^2)}\right]^{-1}, \tag{2.35}$$

$$\alpha^{dimer} = \alpha_{NE}^{eff} + \alpha_{NR}^{eff}, \tag{2.36}$$

where $L(v_i) = (v_i^2 - 1)[(v_i \coth^{-1} v_i) - 1], v_1 = (1 - q^{-2})^{-\frac{1}{2}}$, $l = d + g + b$, $v_2 = l/f$, $q = d/c$, $f = \sqrt{d^2 - c^2}$, $\alpha_{NR} = (4\pi dc^2/3)[\varepsilon(\omega) - \varepsilon_m]/[\varepsilon_m + L(v_1)[\varepsilon(\omega) - \varepsilon_m]]$ is the longitudinal static dipole polarizability of the NR, v_1 and v_2 are the radial coordinates of the NR and the NE-NR system, respectively, $L(v_1)$ and $L(v_2)$ are the the longitudinal static geometric factors of the NR and the NE-NR system, respectively, q is the aspect ratio of the NR, f is the focal distance of the NR, and α_{NE} is the quasi-static dipole polarizability of the NE, obtained in Refs.[90,92] as follows:

$$\alpha_{NE} = 4\pi b^3 \left[\frac{9\varepsilon(\omega)\varepsilon_m K_{11} \Big(\varepsilon_c - \varepsilon(\omega)\Big)\kappa_2 + \Big(\varepsilon(\omega) - \varepsilon_m\Big)\Big(\kappa_1\kappa_2 - \kappa_3\Big)}{\Big(\varepsilon(\omega) + 2\varepsilon_m\Big)\Big(\kappa_1\kappa_2 - \kappa_3\Big)} \right], \quad (2.37)$$

where

$$\kappa_0 = \Big(\varepsilon_c - \varepsilon(\omega)\Big)\Big(\varepsilon(\omega) - \varepsilon_m\Big), \quad (2.38a)$$

$$\kappa_1 = 2K_{11}\kappa_0 + M_{11}\Big(\varepsilon_c + 2\varepsilon(\omega)\Big)\Big(2\varepsilon_m + \varepsilon(\omega)\Big), \quad (2.38b)$$

$$\kappa_2 = 6K_{22}\kappa_0 + M_{22}\Big(2\varepsilon_c + 3\varepsilon(\omega)\Big)\Big(3\varepsilon_m + 2\varepsilon(\omega)\Big), \quad (2.38c)$$

$$\kappa_3 = 3K_{12}M_{21}\kappa_0\Big(\varepsilon(\omega) + 2\varepsilon_m\Big)\Big(3\varepsilon(\omega) + 2\varepsilon_c\Big), \quad (2.38d)$$

and

$$K_{11} = \Big(\frac{a}{b}\Big), K_{22} = \Big(\frac{a}{b}\Big)^2, M_{11} = \Big(\frac{b}{a}\Big)^2, M_{22} = \Big(\frac{b}{a}\Big)^3, \quad (2.39a)$$

$$K_{12} = 2\Big(\frac{a}{b^2}\Big)\sigma, M_{21} = -2\Big(\frac{b^2}{a^3}\Big)\sigma. \quad (2.39b)$$

Here, K_{11} and M_{11} are coupling constants of solid and cavity dipole sphere plasmons, respectively, K_{22} and M_{22} are coupling constants of solid and cavity quadrupole sphere plasmons, respectively, and K_{12} and M_{21} are the dipole–quadrupole and quadrupole–dipole coupling constants of solid and cavity sphere plasmons, respectively.

Absorption and Scattering Spectra of the Dimer

In the quasi-static limit, the scattering and absorption cross-sections of the dimer are calculated using Eq. (1.15b), with the polarizability in Eq. (1.15b) replaced with Eq. (2.36). The Drude-Lorentz local dielectric function for gold (Eq. (1.10)), with the model parameters given in Table 1, will be used. We will consider a NE with dimensions $a = 15$ nm and $b = 20$ nm, and the following core-offsets: $\sigma = 0.0, 1.0, 2.0, 3.0$, and 4.0 nm. For a given aspect ratio of the NR, the dipolar LSPR of the NE is tuned via its core-offset to make it resonant or off-resonant with the longitudinal dipolar LSPR of the NR, while the coupling distance is kept constant. The dimer gap, g, will be set to 1.0 nm, a typical gap distance that has been reported experimentally for heterodimers

in aqueous solutions.[17] Likewise, Eqs. (2.34) and (2.35) show that the plasmon coupling terms, which are proportional to $3\alpha_{NR}\alpha_{NE}[1 - L(v_2)]/4\pi l(l^2 - f^2)$, and $\alpha_{NR}\alpha_{NE}/2\pi l^3$, respectively, are strongly dependent on short dimer gaps. Since each of the coupling terms is proportional to α_{NR}/l at constant g and α_{NE}, we will consider several nanorods with different α_{NR} by varying both c and d in order to tune the plasmon coupling strength.

As shown in Fig. 2.12(**a**), the dipolar LSPR of the NE, which we denote as ω_{ne}, undergoes a redshift with increasing core-offset, i.e., from $\omega_{ne} = 615$ nm when $\sigma = 0.0$ nm to $\omega_{ne} = 652$ nm when $\sigma = 4.0$ nm, in agreement with Ref.[71] At large core-offsets, a quadrupole LSPR is also noticeable in Fig. 2.12(**a**) at around 550 nm, due to an increase in the dipole–quadrupole plasmon coupling strength. In the NE-NR dimer, we studied two groups of NR sizes. For the big nanorods, their absorption cross-sections are comparable to those of the isolated NE, i.e., the NR sizes (d, c) are (24 nm, 12 nm), (24 nm, 9.6 nm), and (24 nm, 8 nm), as shown in panel 1 of Fig. 2.12(**b**), while for the small nanorods, their absorption cross-sections are small compared to those of the isolated NE, i.e., the NR half-length and half-width, (d, c), are (15 nm, 7.5 nm), (15 nm, 6 nm), and (15 nm, 5 nm), as shown in panel 2 of Fig. 2.12(**b**). In the quasi-static limit, the dipolar plasmon resonances of the different NR sizes, which we denote as ω_{nr}, are the same when they have the same aspect ratio,[12,22] i.e., $\omega_{nr} = 586$ nm, 625 nm, and 673 nm, corresponding to q = 2.0, 2.5 and 3.0, respectively, while their absorption cross-sections are different, as shown in Fig. 2.12(**b**), panels 1 and 2, respectively). The absorption spectra of the NE-NR dimer are shown in Fig. 2.13

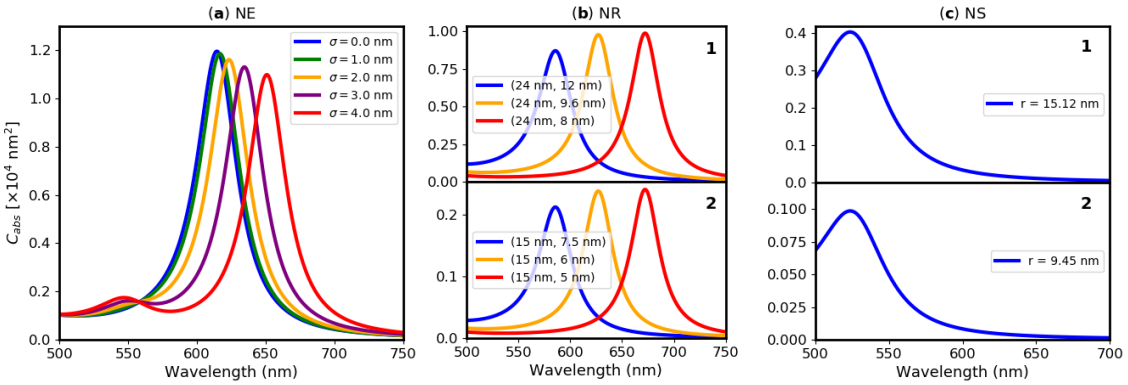

Figure 2.12: Absorption cross-sections of the uncoupled nanoparticles. (**a**) Absorption cross-sections of the NE for each of the core-offsets studied. (**b**) Absorption cross-sections of the big nanorods (panel **1**) and those of the small nanorods (panel **2**), respectively. (**c**) Absorption cross-section of a nanosphere with the same volume as that of the blueshifted big NR (panel **1**) and small NR (panel **2**).

while the scattering spectra are shown in Fig. 2.14 for each of the three plasmon peak positions of the nanorods with respect to those of the NE, respectively.

For the blueshifted nanorods i.e., the nanorods with half-dimensions (24 nm, 12 nm) and (15 nm, 7.5 nm), with a LSPR of 586 nm, the absorption and scattering spectra of the NE-NR dimer in Figs. 2.13((**a**), (**d**)) and 2.14((**a**), (**d**)),

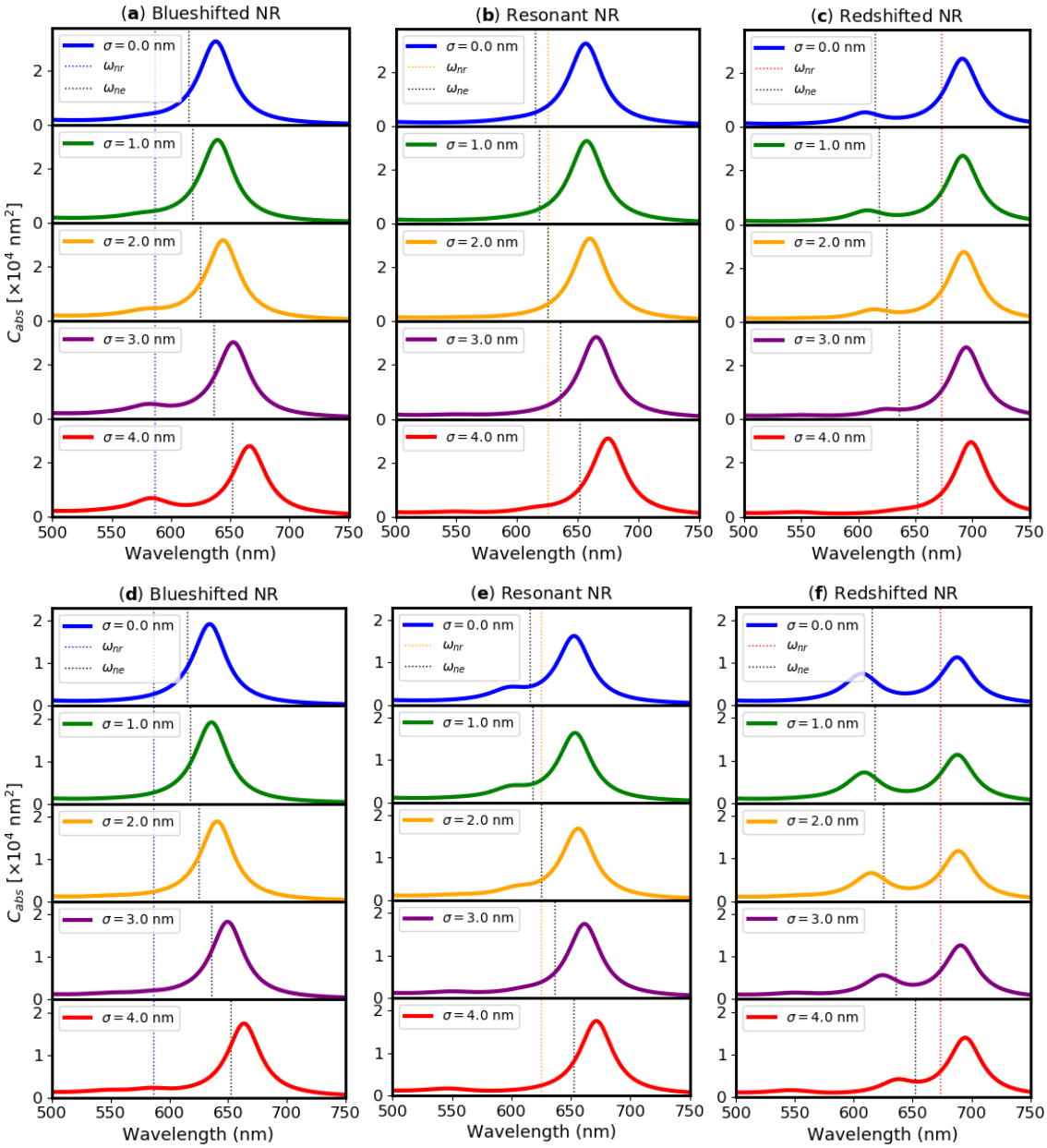

Figure 2.13: Absorption cross-sections of the NE-NR dimer, for the different core-offsets of the NE, in the case of nanorods with different absorption cross-sections and plasmon peak positions, corresponding to NR sizes (d, c): (**a**) (24 nm, 12 nm) NR and (**d**) (15 nm, 7.5 nm) NR (Blueshifted nanorods), (**b**) (24 nm, 9.6 nm) NR and (**e**) (15 nm, 6 nm) NR (Resonant nanorods), and (**c**) (24 nm, 8 nm) NR and (**f**) (15 nm, 5 nm) NR (Redshifted nanorods), with respect to those of the NE. Top row: the big nanorods. Bottom row: the small nanorods. The dotted lines represent the plasmon peak positions of the NR and NE, respectively.

respectively, show a gradual appearance of transparency dips and mode splittings as ω_{ne} redshifts from ω_{nr}. This is due to an increase in the plasmon detuning frequency, $\omega_{ne} - \omega_{nr}$, which leads to mode splitting. However, the big NR, with half-dimensions (24 nm, 12 nm), whose plasmon linewidth and absorption cross-

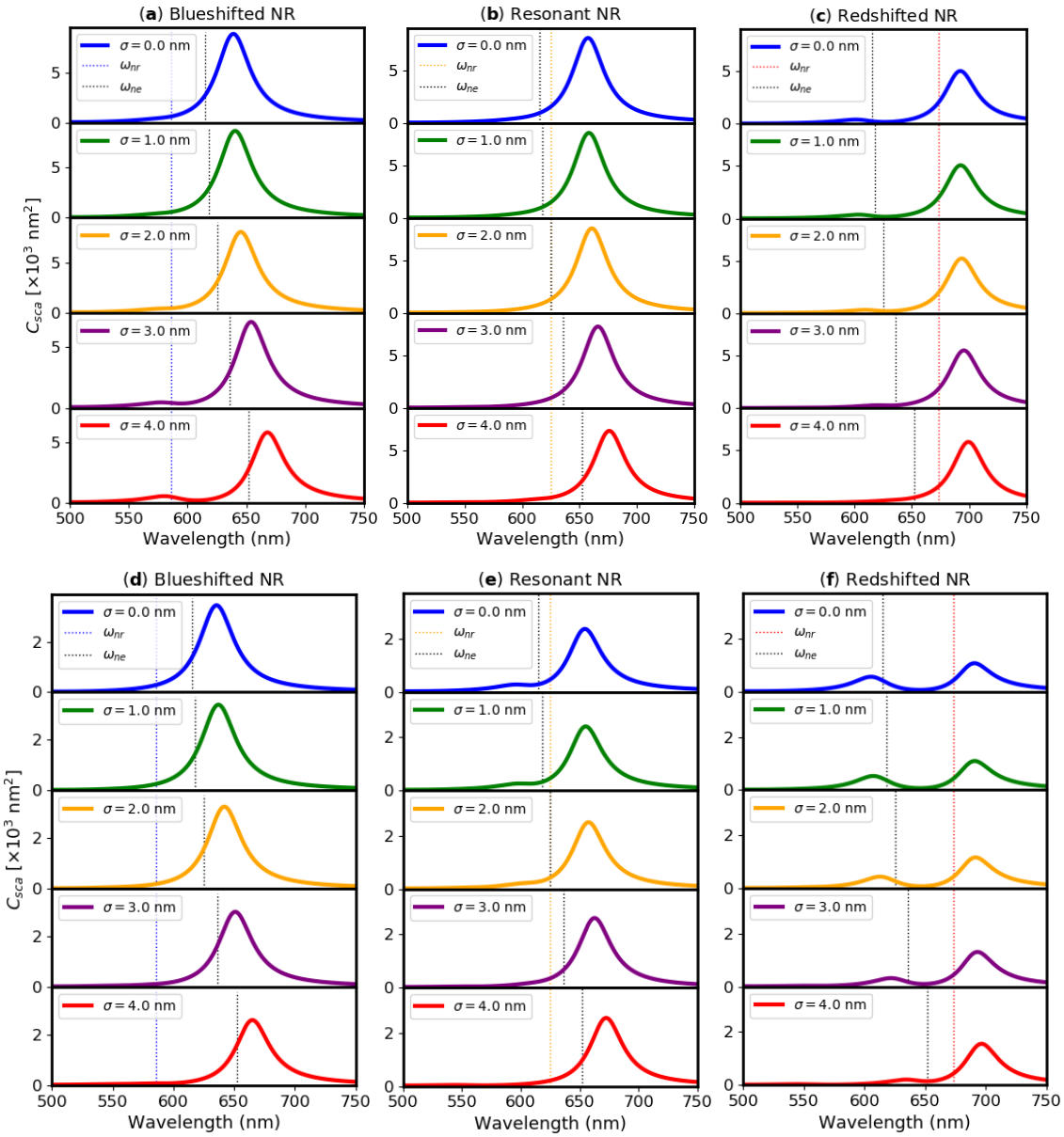

Figure 2.14: Scattering cross-sections of the NE-NR dimer, for the different core-offsets of the NE, in the case of nanorods with different absorption cross-sections and plasmon peak positions, corresponding to NR sizes (d, c): (**a**) (24 nm, 12 nm) NR and (**d**) (15 nm, 7.5 nm) NR (Blueshifted nanorods), (**b**) (24 nm, 9.6 nm) NR and (**e**) (15 nm, 6 nm) NR (Resonant nanorods), and (**c**) (24 nm, 8 nm) NR and (**f**) (15 nm, 5 nm) NR (Redshifted nanorods), with respect to those of the NE. Top row: the big nanorods. Bottom row: the small nanorods. The dotted lines represent the plasmon peak positions of the NR and NE, respectively.

section are comparable to those of the NE (Fig. 2.12), induces more plasmon shifts and some noticeable transparency dips, and leads to more enhanced spectra, as shown in Figs. 2.13(**a**) and 2.14(**a**), due to its large absorption cross-section (Fig. 2.12(**b**), panel 1) compared to that of the small NR with dimensions (15 nm, 7.5 nm) (Fig. 2.12(**b**), panel 2). For the small NR, nearly only plasmon-induced

LSPR shifts occur in the dimer spectra in Figs. 2.13(**d**) and 2.14(**d**), even when the detuning frequency is high. This is because the NR absorption cross-section (Fig. 2.12(**b**), panel 2) is too small compared to those of the NE (Fig. 2.12(**a**)). In addition, the plasmon-induced shifts in the spectra of the NE-NR dimer, i.e., the strong redshifts in ω_{ne} and the weak blueshifts in ω_{nr}, are slightly larger for the big NR due to its large polarizability.

Figs. 2.13(**b**) and 2.14(**b**) show the absorption and scattering spectra of the dimer when the NE is coupled to a big NR, (24 nm, 9.6 nm), with $\omega_{nr} = 625$ nm resonant with the NE at $\sigma = 2.0$ nm, whose absorption cross-section is comparable to that of the NE (Fig. 2.12(**b**), panel 1). The spectra of the NE-NR dimer (Figs. 2.13(**b**) and 2.14(**b**)) only feature plasmon-induced LSPR shifts. This is because the plasmon coupling strength is small, since a long half-length of the NR leads to a longer inter-particle distance, so that plasmon hybridization leads only to a strong redshift in ω_{ne}, even beyond zero detuning ($\omega_{ne} \neq \omega_{nr}$). In addition, the plasmon linewidths of the isolated NE and NR absorption spectra are comparable (Fig. 2.12(**a**) and Fig. 2.12(**b**), panel 1), so that Fano interference does not occur. However, when the NE is coupled to a small NR, (15 nm, 6 nm), whose absorption cross-section is smaller than that of the NE, and also resonant with the NE at $\sigma = 2.0$ nm (Fig. 2.12(**b**), panel 2), both the scattering and absorption spectra of the dimer feature some noticeable induced transparency when $\sigma \leq 2.0$ nm (Figs. 2.13(**e**) and 2.14(**e**)). In this case, the plasmon linewidths of the isolated NE and NR are not comparable and the coupling strength due to the (15 nm, 6 nm) NR is more than that of the (24 nm, 9.6 nm) NR as a result of its short half-length, so that Fano interference can occur, but plasmon hybridization only leads to mode splitting when $\sigma \leq 2.0$ nm. Beyond $\sigma = 2.0$ nm, the NR absorption is too small compared to that of the NE for any significant mode splitting to take place. Similar to the blueshifted NR case, the plasmon-induced LSPR shifts are slightly greater and the spectra of the dimer are more enhanced when the NR is bigger due to its large polarizability.

In the case of redshifted nanorods, the absorption and scattering spectra of the NE-NR dimer in Figs. 2.13(**c**) and 2.14(**f**), respectively, show a gradual decrease in both the induced transparency dips and mode splittings as ω_{ne} approaches ω_{nr}. This is expected since the detuning frequency, $\omega_{nr} - \omega_{ne}$, decreases in this case so that mode splitting becomes more unlikely. However, the small NR, (15 nm, 5 nm), induces significant transparency dips in the dimer spectra (Figs. 2.13(**f**) and 2.14(**f**)) compared to the dimer spectra for the big NR, (24 nm, 8 nm) (Figs. 2.13(**c**) and 2.14(**c**)), irrespective of the detuning frequency. As a result, the smaller NR can enhance or reduce the cross-sections of the NE-NR dimer (Figs. 2.13(**f**) and 2.14(**f**)) depending on the core-offset of the NE. This is partly due to the difference between the plasmon linewidths of the isolated NE (Fig. 2.12(**a**)) and the small NR (Fig. 2.12(**b**, panel 2) compared to that of the big NR (Fig. 2.12(**b**, panel 1), and also due to a stronger coupling strength in the dimer when the NR half-length is short due to a smaller centre-to-centre distance. The plasmon-induced shifts in the dimer spectra, i.e., the weak redshifts in ω_{nr} and the strong blueshifts in ω_{ne}, and the enhancement of the cross-sections for the big NR are greater than those of the small NR due to the large polarizability of

the former. Similar size-dependent spectral shifts and enhancement of optical cross-sections have been reported for other dimers studied in Refs.[17–19] For instance, similar to one of the scattering spectra of the NS-NR dimer studied in Ref.,[17] when the NS is located at the end of the NR and the NR is at a redshifted plasmon peak position with respect to the plasmon peak of the NS, the scattering spectra of the NE-NR dimer (Fig. 2.14(**f**)) also contain two scattering peaks. However, for the NE-NR dimer, a high-energy peak, which is weak and decreases with increasing core-offset, and a low-energy peak, which is strong and increases with decreasing core-offset, are formed.

When $\sigma = 0.0$ nm, i.e., a concentric nanoshell, the transparency dips in both the absorption and scattering spectra of the NE-NR dimer (Fig. 2.13 and Fig. 2.14) are more noticeable in the redshifted small NR case (Fig. 2.13(**f**) and Fig. 2.14(**f**, top panels) compared to those of the blueshifted small NR case (Fig. 2.13(**d**) and Fig. 2.14(**d**, top panels), whereas at large core-offsets, such as $\sigma = 4.0$ nm, the converse is true for the big nanorods (Fig. 2.13(**a**) and Fig. 2.14(**a**, bottom panels). Again, this behaviour is due to the detuning frequency, which can be increased or decreased with respect to the spectral peak position of the NR.

We considered nanospheres with the same volume as the blueshifted nanorods by using the equivalent sphere-volume radius of the NR as the radius of the NS in each case, i.e., $r = \sqrt[3]{dc^2}$, to obtain $r = 15.12$ nm for the (24 nm, 12 nm) NE-NR dimer and $r = 9.45$ nm for the (15 nm, 7.5 nm) NE-NR dimer. Their dipolar LSPR, which is at around 525 nm, as shown in Fig. 2.12(**c**, panels 1 and 2), is the same in the quasi-static limit. To obtain the polarizability of the NE-NS dimer from that of the NE-NR dimer, we set $L(v_1) = L(v_2) = 1/3$, i.e., the static geometric factor of an isotropic sphere,[12,22] $f = 0$, and $l = r + g + b$. As shown in Fig. 2.15, both the absorption and scattering spectra of the NE-NS dimer are less enhanced compared to those of the NE-NR dimer (Figs. 2.13(**a**)-(**f**) and 2.14(**a**)-(**f**), respectively), for the blueshifted NR case. This is due to the smaller polarizability of the NS compared to that of the NR of the same volume. Compared to the NE-NR dimer, the spectra of the NE-NS dimer (Fig. 2.15) are dominated by plasmon-induced LSPR shifts due to the small absorption cross-section of the NS compared to that of the NE. However, the trends that lead to plasmon-induced shifts and induced transparency in the NE-NS dimer are similar to those of the NE-NR dimer for the blueshifted NR case.

In the above discussions, we have attributed the plasmon-induced transparency phenomenon to either plasmon hybridization or Fano interference or both, since the plasmon linewidths of the dipolar modes of the NR and the NE can be comparable or dissimilar, depending on the NR size. As discussed in Refs.,[42,71] and as we have explained above, a difference in the plasmon linewidths also leads to induced transparency as a result of Fano interference between the two plasmon modes. Plasmon coupling in the NE-NR dimer depends on both the plasmon detuning frequency and the NR size. The appearance of transparency dips in the dimer spectra for all NR spectral peak positions studied shows that for a given NE size, the dimer can be strongly coupled depending on the detuning frequency and the NR size. The latter determines the plasmon coupling strength through the half-length of the NR[77] and Fano interference through the

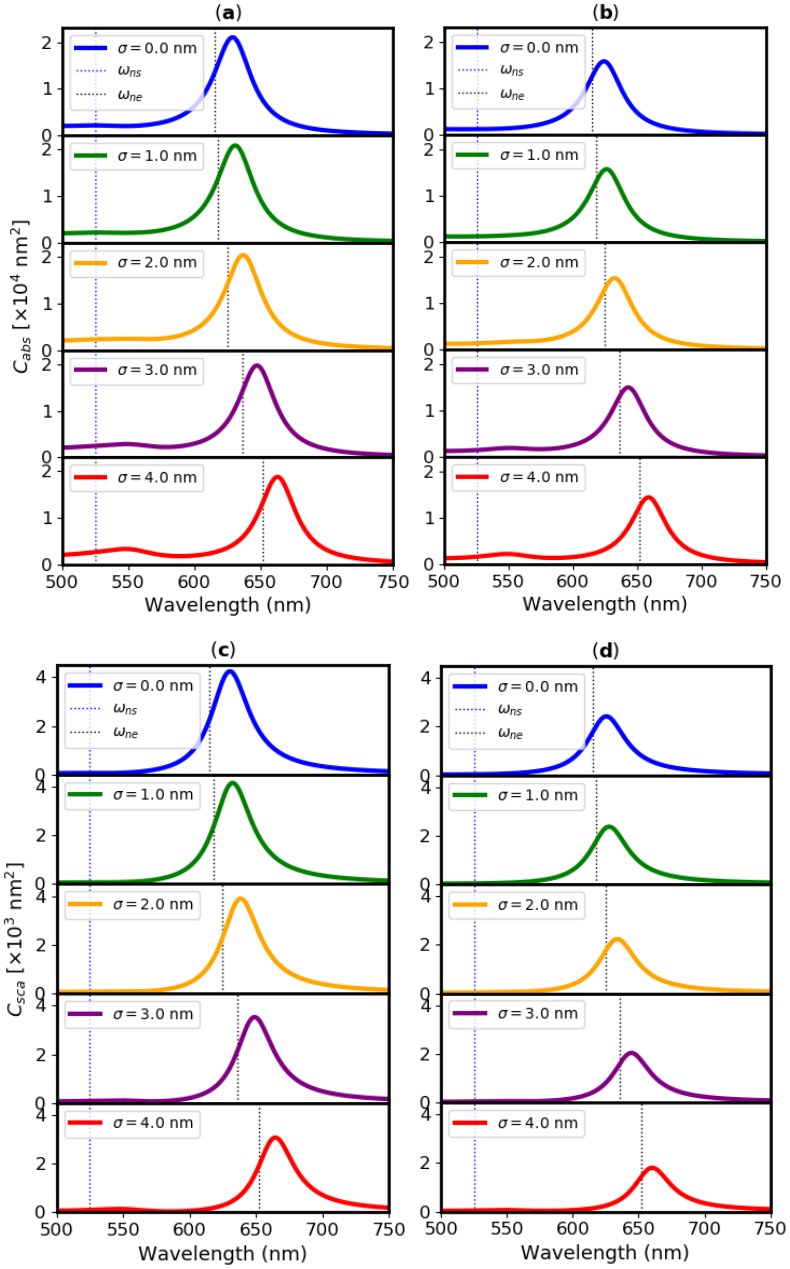

Figure 2.15: Absorption cross-sections of the NE-NS dimer (top row, (**a**) and (**b**)), and scattering cross-sections of the NE-NS dimer (bottom row, (**c**) and (**d**)), respectively, for the different core-offsets of the NE, in the case of nanospheres with the same volume as the blueshifted nanorods: (**a**) and (**c**) (24 nm, 12 nm) NR, r = 15.12 nm, and (**b**) and (**d**) (15 nm, 6 nm) NR, r = 9.45 nm. The dotted lines represent the plasmon peak positions of the NS and NE, respectively.

NR absorption linewidth,[17] while the former determines plasmon hybridization. This is consistent with plasmon coupling in other heterodimers[17,19] where plasmon-induced transparency has been reported.

In addition, the redshifts in the hybrid plasmon modes of the NE-NR dimer and the enhanced spectra of the dimer (Figs. 2.13 and 2.14) are consistent with the trends reported in Ref.[19] for an incident field parallel to the dimer

axis. However, the NE-NR heterodimer is such that decreasing or increasing the detuning frequency at constant NE size can lead to induced transparency, depending on the spectral peak position of the NR. In addition, a small NR whose absorption cross-section is less than that of the NE at a redshifted plasmon peak position tends to induce more transparency dips in the dimer spectra, irrespective of the detuning frequency, compared to a small NR with similar absorption cross-section at a blueshifted or resonant plasmon peak position. This might be related to the direction of the core-offset, which is towards the NR in the redshifted NR case. However, in comparison to the NS-NR dimer studied in Ref.,[17] it could also be due to both the redshifted spectral peak position of the NR and the positioning of the NE along the NR long axis.

Both the absorption and scattering spectra of the NE-NR dimer show a common trend: the emergence of mode splittings and plasmon-induced transparency dips as the detuning frequency is tuned via the core-offset of the NE at a constant NR size, in addition to plasmon-induced LSPR shifts. However, similar to the spectral behaviour of the NR dimer studied in Ref.,[42] the scattering dips are greater than the absorption dips due to their different dependence on the wavelength of light in the medium. For instance, compared to the absorption spectra in Fig. 2.13(**f**), the scattering spectra of the redshifted NR case in Fig. 2.14(**f**) are almost entirely transparent between 630 nm and 670 nm.

Plasmon-Induced LSPR Shifts

Due to plasmon coupling, ω_{ne} and ω_{nr} undergo plasmon hybridization to form new dipolar plasmon modes. Depending on the detuning frequency and the NR size, both plasmon-induced transparency and plasmon-induced LSPR shift will occur or only the latter occurs in the dimer spectra. The spectral peak positions of the NE-NR dimer (Fig. 2.13) correspond to the plasmon resonances of these new modes. As summarized in Table 2 for the small nanorods with $d = 15$ nm, the hybrid plasmon modes of the dimer inherit the intrinsic property of the NE, i.e., they undergo a redshift with increasing core-offset, depending on whether the NR absorption leads to mode splitting in the dimer spectra. A redshift is also expected for an incident field parallel to the dimer axis.[18,19] However, the sensitivities of the hybrid plasmon modes to changes in the core-offset differ due to the different NR polarizabilities.

In Fig. 2.16, the scattering cross-section of the dimer is significantly enhanced in the blueshifted NR case (Fig. 2.16(**a**)), due to a longer half-width of the NR, compared to the other cases (Fig. 2.16(**b**) and (**c**)). When the NR absorption does not lead to a significant induced transparency, the cross-sections of the NE-NR dimer are more enhanced (Fig. 2.16(**a**) and (**b**)) compared to the redshifted NR case (Fig. 2.16(**c**)). Plasmon coupling leads to a strong redshift in ω_{ne} to form a bright, low-energy hybrid plasmon mode, ω_{-}, whose scattering intensity decreases with increasing core-offset (Fig. 2.16(**a**)), compared to Fig. 2.16(**b**) and (**c**), where the intensity of the bright hybrid mode increases with increasing core-offset. However, in the latter two cases, the intensity of the bright mode is affected by induced transparency in the scattering spectra of the dimer since the

NR absorption is reduced further compared to that of the NE. A new, weak, high-energy hybrid plasmon mode, ω_+, is then formed, depending on the plasmon detuning frequency. For the small nanorods, only ω_- is formed in the blueshifted NR case, as shown in Fig. 2.16(a) and in Table 2. In the dispersion curves in Fig. 2.16(**b**) and (**c**), the weak scattering peak is hardly visible in the redshifted NR case (Fig. 2.16(**c**)), while it is completely absent in the resonant NR case (Fig. 2.16(**b**)). For the redshifted NR, ω_+ vanishes gradually as the core-offset is increased (Fig. 2.14(**f**)), due to a decrease in the detuning frequency. Depending on the spectral peak position of the NR and its size, the respective sensitivity of the hybrid plasmon modes to changes in the core-offset differs, i.e., ω_+ is more sensitive in the redshifted NR case, while ω_- is more sensitive in both the blueshifted and resonant NR cases. Also, ω_+ is formed by a plasmon-induced blueshift in ω_{ne} for the redshifted NR. On the other hand, ω_- is formed by a plasmon-induced redshift in ω_{ne} for the blueshifted and resonant nanorods, while it is due to a redshift in ω_{nr} for the redshifted NR. This is depicted in the energy-level diagram in Fig. 2.17.

Isolated NE		NE-NR dimer with a blueshifted NR	NE-NR dimer with a resonant NR		NE-NR dimer with a redshifted NR		
		$c = 7.5$ nm	$c = 6.0$ nm		$c = 5.0$ nm		
		$\omega_{nr} = 586$ nm	$\omega_{nr} = 625$ nm		$\omega_{nr} = 673$ nm		
σ (nm)	ω_{ne} (nm)	ω_- (nm)	ω_- (nm)	ω_+ (nm)	ω_- (nm)	ω_+ (nm)	χ (meV)
0	615	635	653	598	692	606	92.835
1	618	638	654	600	693	609	92.225
2	625	642	657	–	695	615	91.980
3	636	651	662	–	697	625	87.340
4	652	665	671	–	699	636	82.700

Table 2: Dependence of ω_{ne}, ω_-, ω_+, and χ on the core-offset, σ, of the NE, for the small nanorods.

Plasmon coupling in MNP dimers has been described previously using a coupled harmonic oscillator (CHO) model.[17] Here, we adopt the same model in order to determine the plasmon coupling strength in the NE-NR dimer when the NR absorption leads to mode splitting for all the core-offsets studied, i.e., for the small redshifted NR. We seek a relationship between the detuning frequency, the coupling strength, and mode splitting. The CHO model gives the hybrid plasmon modes as[42,43,93,94]

$$\omega_\pm = \tfrac{1}{2}(\omega_{ne} + \omega_{nr}) - \tfrac{i}{4}(\gamma_{nr} + \gamma_{ne}) \pm \tfrac{1}{2}\sqrt{4\chi^2 + \left[(\omega_{ne} - \omega_{nr}) + \tfrac{i}{2}(\gamma_{nr} - \gamma_{ne})\right]^2}, \quad (2.40)$$

where we have rewritten the equation in terms of the model parameters of the NE-NR dimer. Here, ω_{ne} and ω_{nr} are the LSPR of the NE and NR, respectively, γ_{ne} and γ_{nr} are the dipolar plasmon linewidths of the NE and NR, respectively, χ is the dipole–dipole plasmon coupling strength of the NE-NR dimer, ω_+ is the high-energy hybrid plasmon mode, and ω_- is the low-energy hybrid plasmon mode. In Eq. (2.40), the $(\omega_{ne} - \omega_{nr})$ term determines whether plasmon

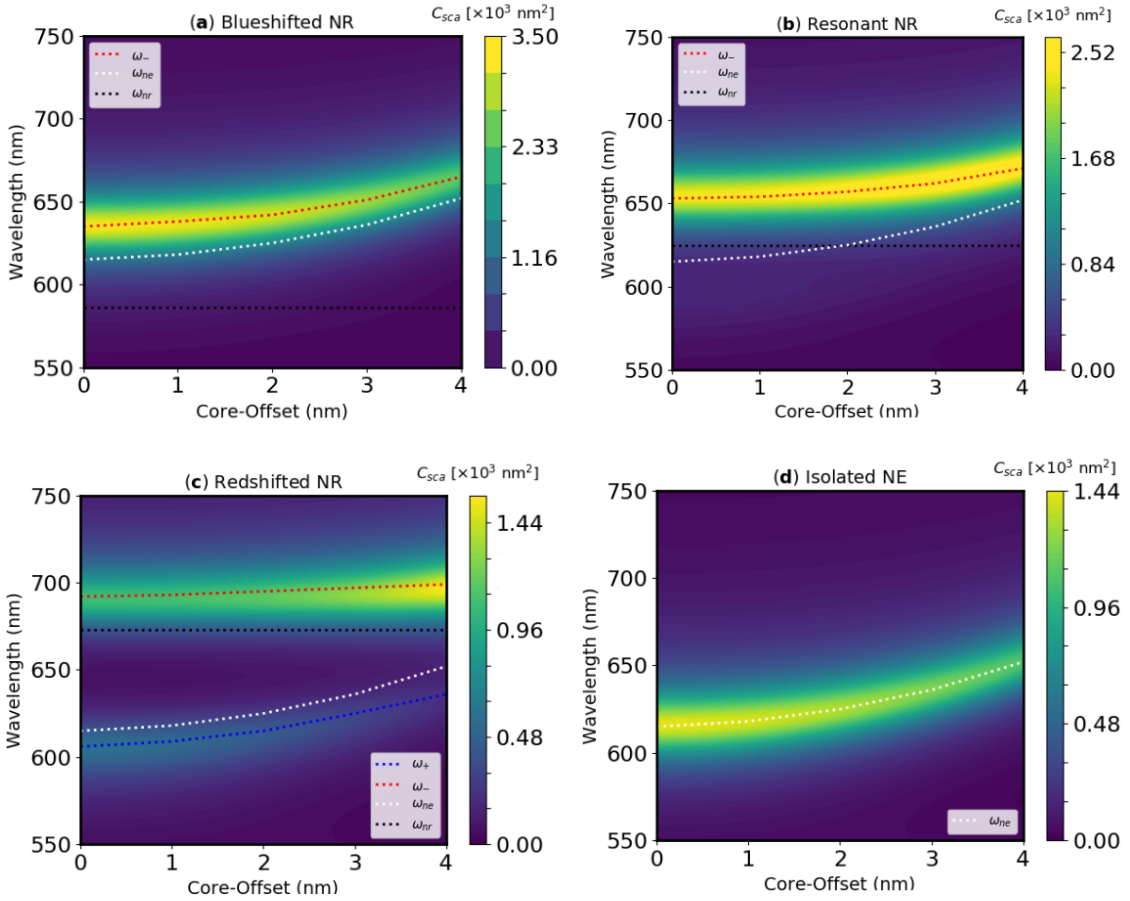

Figure 2.16: Contour plots of the scattering cross-sections of the NE-NR dimer, showing the dispersion curves when the NE is coupled to the (**a**) blueshifted, (**b**) resonant, and (**c**) redshifted, small nanorods, with respect to the plasmon peaks of the isolated NE, and (**d**) contour plot of the scattering cross-section of the isolated NE. The colour bars indicate the maximum value of the scattering cross-section in each case. The line plots represent the dependence of ω_{ne}, ω_+ and ω_- on the core-offset, respectively, with respect to ω_{nr}, while the "smearing" around them is due to their imaginary parts, i.e., the plasmon linewidths.

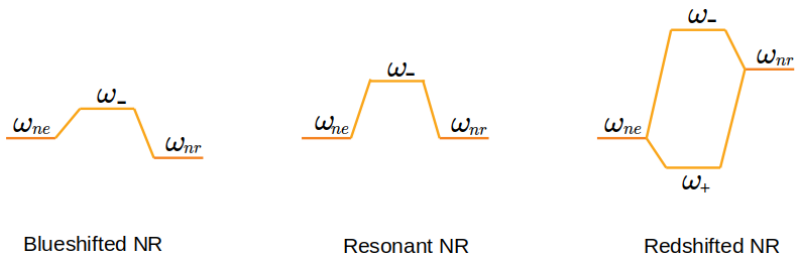

Figure 2.17: Plasmon hybridization diagram showing how the spectral peak positions of the small nanorods in Table 2 and their detuning frequency affect the hybrid plasmon modes and the mode splitting, based on the data for $\sigma = 2.0$ nm.

hybridization will occur, the $(\gamma_{nr} - \gamma_{ne})$ term determines Fano interference, while

a combination of either of these two terms or both, and χ, determines the mode splitting. From Eq. (2.40), we obtain the coupling strength as

$$\chi = \frac{1}{2}\sqrt{\Omega^2 - \Delta^2}, \tag{2.41}$$

where we have assumed that $\gamma_{ne} \approx \gamma_{nr}$, which is only true when the NR absorption is comparable to that of the NE or when absorption losses due to plasmon damping are negligible.[43] However, it allows us to obtain a real χ.[42,43] In Eq. (2.41), $\Omega = \omega_+ - \omega_-$ is the mode splitting,[43,93] and $\Delta = \omega_{ne} - \omega_{nr}$ is the detuning frequency. As shown in Fig. 2.17, Δ determines ω_-, ω_+, and Ω for a given NR absorption cross-section. For each core-offset, we used Eq. (2.40) to determine the coupling strengths shown in energy units in Table 2. The trends in χ indicate that for a given dimer gap and NR size, the coupling strength decreases gradually with a decrease in the detuning frequency for the redshifted NR. This is also expected since once the NR size is kept constant, only the detuning frequency will determine plasmon-induced transparency in the spectra of the NE-NR dimer.

Ref.[71] has shown that the amplitude of the dipolar mode of a NE decreases with increasing core-offset, due to dipole–quadrupole plasmon coupling. The downside of this plasmonic behaviour is that the absorption and scattering cross-sections of the NE decrease with increasing core-offset, as we have shown in Fig. 2.12(**a**). However, by coupling the NE to a NR, the absorption and scattering cross-sections of the NE-NR dimer are significantly enhanced, as shown in Figs. 2.13 and 2.14, respectively. In addition, the PIT regions in the dimer spectra can be used as a sensing parameter in LSPR spectroscopy to distinguish between NR sizes, since the PIT phenomenon in the dimer is very sensitive to changes in the NR size.

3

PLASMON-ENHANCED FLUORESCENCE

3.1 INTRODUCTION

Theoretical models describing the modifications of the decay rate of an excited molecule near a metal layer can be traced back to Chance et al.[95] Similar models were then proposed by Gersten and Nitzan,[52] Ruppin,[96] and Ford and Weber,[62] for metallic nanospheroids and nanospheres respectively. These models predict that the decay rate of an excited molecule near a metal-dielectric interface increases with decreasing metal-molecule separation and decreases with increasing metal-molecule distance.[52,62,95,96] The former is due to the increased rate of non-radiative energy transfer from the excited molecule to the metal, while the latter is due to interference between the incident field on the molecule and the induced field on the molecule as a result of the reflected field at the metal-dielectric boundary.

The enhancement of the radiative decay rate of a molecule near a metal is known as the Purcell effect.[97–99] It has been studied both theoretically and experimentally in the emission stage of the phenomenon of plasmon-enhanced fluorescence (PEF). PEF, the effect of increase in the emission rate of a molecule near a MNP, is characterized by an increase in both the quantum yield[67,100,101] and excitation rate of the molecule.[9,98] PEF reaches its maximum at a wavelength red-shifted from the dipolar localized surface plasmon resonance (LSPR) of the metal nanoparticle (MNP).[99,102] It depends on the excitation wavelength, the optical properties of the molecule, the molecule's dipole orientation, the molecule's position from the MNP, the MNP-molecule distance, the MNP geometry, the material composition of the MNP, polarization of the incident electric field, and the dielectric embedding medium. However, molecule-dependent, plasmon-induced quenching of fluorescence can also occur at short distances between the MNP surface and the molecule.[98]

The dependence of PEF on MNP geometry has been investigated in molecules near metal layers,[95,97,103] metallic spheres,[98–100] metallic nanorods and nanospheroids,[9,11,26,60,67,101] metallic nanoshells,[60,104,105] nanoparticle dimers,[86,87,106] and with MNPs of irregular geometries.[102,107] The molecule-dependence of PEF has been studied with different molecules, including photosynthetic pigments,[11,101,108] where PEF has been shown to be more pronounced in weakly-emitting molecules,[9,100,101] while the material-dependence of PEF has been mostly reported using gold,[11,60,98] silver,[104,109] and aluminum[5] nanoparticles.

3.2 EMISSION RATE OF A MOLECULE NEAR A NANOANTENNA

In this section, we will follow the approach employed by Khatua et al.,[9] to derive the equation used for calculating the emission rate enhancement of an excited molecule near a MNP. However, we will re-write this equation in terms of the emitter's quantum yields, i.e., the quantum yield of the molecule in the absence of the MNP, also known as the *intrinsic quantum yield*, and the quantum yield of the molecule in the presence of the MNP, also known as the *quantum yield enhancement*. This classical approach assumes that the emission occurs at a single frequency, and that the MNP does not alter the intrinsic non-radiative decay rate of the molecule, γ^o_{nrad}.[9,98,99,106] In addition, the model is only valid in the weak-excitation limit, where quantum effects between the ground and excited states of the molecule, and the depletion of the molecule's ground state population, can be neglected.[9,42] In other words, the model is valid at excitation intensities much lower that the saturation intensity of the emitter.[42]

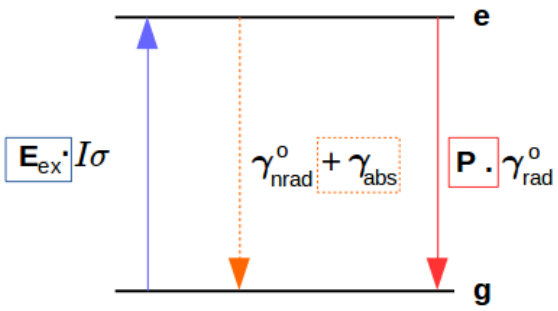

Figure 3.1: A simple two-level system showing the transition rates of the emitter in the absence and presence of a MNP. Here, I is the laser excitation intensity, σ is the absorption cross-section of the molecule, γ^o_{rad} and γ^o_{nrad} are the intrinsic radiative and non-radiative decay rates of the molecule, respectively, $\mathbf{P}$ is the Purcell factor, γ_{abs} is the rate of power absorption by the MNP, and $\mathbf{E}_{ex}$ is the excitation rate enhancement. The modified rates (shown in boxes) are due to the contribution from the MNP. (Adapted from Ref.[9])

For an excited molecule (modelled as a molecular dipole[62,101]) near a MNP, energy conservation requires that the rate of power dissipation by the excited molecule, γ_{diss}, must be equal to the non-radiative energy transfer rate from the molecule to the MNP. This energy is then absorbed by the MNP where it is dissipated as heat due to Ohmic heating in the metal.[52,62,96,104] Also, if we consider the two-way antenna model described in Ref.,[99] where the molecular dipole acts as a transmitter of radiation while the MNP acts as a receiver or vice-versa, as depicted in Fig. 3.2, then the Purcell factor can also be regarded as

the normalized rate of radiative energy transfer, $\gamma_{rad}/\gamma^o_{rad}$, from the MNP to the molecular dipole. In all, we have

$$\text{(Emitter)} \quad \frac{\gamma_{diss}}{\gamma^o_{rad}} = \frac{\gamma_{abs}}{\gamma^o_{rad}} \quad \text{(MNP)}, \tag{3.1a}$$

$$\mathbf{P} = \frac{\gamma_{rad}}{\gamma^o_{rad}}. \tag{3.1b}$$

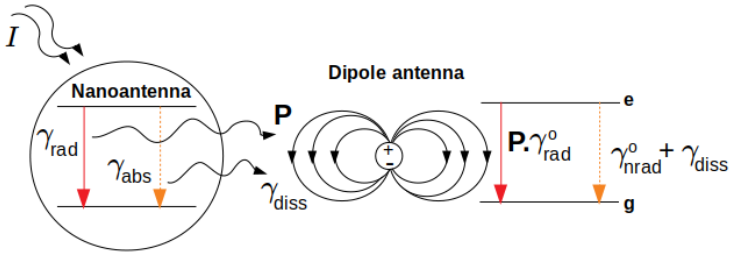

Figure 3.2: A schematic of the two-way antenna model described in Ref.[99] Here, the molecular emitter is a dipole receiver antenna while the MNP is a transmitter nanoantenna.

In Figs. 3.1 and 3.2, γ^o_{rad} and γ^o_{nrad} are the radiative and non-radiative decay rates of the molecule in the absence of the MNP, respectively, and γ_{rad} in Fig. 3.2 is the radiative energy transfer rate from the MNP to the molecular dipole. The MNP absorbs the power dissipated by the molecule (a radiating dipole) at a rate denoted by γ_{abs}, which enters the model as a non-radiative decay channel. The Purcell factor, i.e., the enhancement of the radiative decay rate of the molecule, denoted by $\mathbf{P}$, and defined in Eq. (3.1b), is evaluated at the emission frequency, ω_{em}, while the excitation rate enhancement of the emitter in the presence of the MNP, denoted by $\mathbf{E}_{ex}$, is evaluated at the excitation frequency, ω_{ex}.

In the absence of the MNP, the rate of population change of the excited state, $\dot{\rho}^o_e$, and the emission rate, γ^o_{em}, of the molecule can be written as follows:[9]

$$\dot{\rho}^o_e = I\sigma\rho^o_g - (\gamma^o_{rad} + \gamma^o_{nrad})\rho^o_e, \tag{3.2a}$$

$$\gamma^o_{em} = \rho^o_e\gamma^o_{rad}, \tag{3.2b}$$

σ is the absorption cross-section of the molecule, $\rho^o_g = 1 - \rho^o_e$ and ρ^o_e are the probabilities of finding the molecule in the ground and excited states, respectively, and the superscript "o" denotes the absence of the MNP. In the presence of the MNP, the rate of population change of the excited state, $\dot{\rho}_e$, and the emission rate of the molecule, γ_{em}, are respectively:

$$\dot{\rho}_e = \mathbf{E}_{ex}I\sigma\rho_g - (\mathbf{P}\gamma^o_{rad} + \gamma^o_{nrad} + \gamma_{abs})\rho_e, \tag{3.3a}$$

$$\gamma_{em} = \rho_e\mathbf{P}\gamma^o_{rad}, \tag{3.3b}$$

where $\rho_g = 1 - \rho_e$ and ρ_e are the probabilities of finding the molecule in the ground and excited states, respectively, in the presence of the MNP. Under steady-state conditions: $\dot{\rho}_e^o = 0,\ \dot{\rho}_e = 0$, we obtain

$$\gamma_{em}^o = \frac{I\sigma Y_o \gamma_{rad}^o}{Y_o I\sigma + \gamma_{rad}^o}, \tag{3.4a}$$

$$\gamma_{em} = \frac{\mathbf{E}_{ex} I\sigma \mathbf{P} \gamma_{rad}^o}{\mathbf{E}_{ex} I\sigma + \gamma_{rad}^o \left[\mathbf{P} + \left(\frac{1-Y_o}{Y_o}\right)\right] + \gamma_{abs}}, \tag{3.4b}$$

where $Y_o = \gamma_{rad}^o / (\gamma_{rad}^o + \gamma_{nrad}^o)$ is the intrinsic quantum yield of the molecule. The emission rate enhancement or fluorescence enhancement[9,99] is the ratio of γ_{em} to γ_{em}^o. Assuming weak-excitation: $\gamma_{rad}^o + \gamma_{nrad}^o >> I\sigma,\ \mathbf{P}\gamma_{rad}^o + \gamma_{nrad}^o + \gamma_{abs} >> \mathbf{E}_{ex} I\sigma$, we obtain

$$\frac{\gamma_{em}}{\gamma_{em}^o} \approx \mathbf{E}_{ex} \frac{Y}{Y_o}, \tag{3.5a}$$

$$Y = Y_o \left[\frac{1 - Y_o}{\mathbf{P}} + \frac{Y_o}{\eta}\right]^{-1}, \tag{3.5b}$$

$$\eta = \mathbf{P} \left[\mathbf{P} + \frac{\gamma_{abs}}{\gamma_{rad}^o}\right]^{-1}, \tag{3.5c}$$

where Y denotes the quantum yield enhancement of the molecule, which is evaluated at the emission frequency, ω_{em}, and η denotes the antenna efficiency. Here, Eq. (3.5a) shows that enhancement in the emission rate will always occur provided that $\mathbf{E}_{ex} > 1$ and $Y \geq Y_o$. However, the latter condition is always met once $\eta > Y_o$. On the other hand, $\mathbf{E}_{ex}$ depends only on the local field induced on the molecule by the nanoantenna.[98,99] It does not depend on the photophysical properties of the molecule.[9] Therefore, the PEF phenomenon is characterized by two independent stages: the *excitation stage*, where the phenomenon can be entirely controlled through the optical properties of the MNP, and the *emission stage*, where both the optical properties of the molecule and the MNP determine the occurrence of PEF.

3.3 MOLECULE NEAR A NANOSPHERE

To calculate the enhancement of the excitation and emission rates of a molecule near a nanosphere (NS), we will use the theoretical method proposed by Gersten and Nitzan[52] and Ford and Weber.[62] Their method is based on the electrostatic approximation and the semiclassical theory of radiation. It involves the following: the excited molecule is treated as an oscillating point dipole which provides the source field, both the MNP-molecule distance and the MNP size have to be small compared to the wavelength of light in the medium, the local, longitudinal wavevector-independent, complex dielectric function of the metal is used (Eq. 1.10), the electric potentials are solutions of Laplace equation in each region of interest, the decay rates are obtained from the modified classical power of the

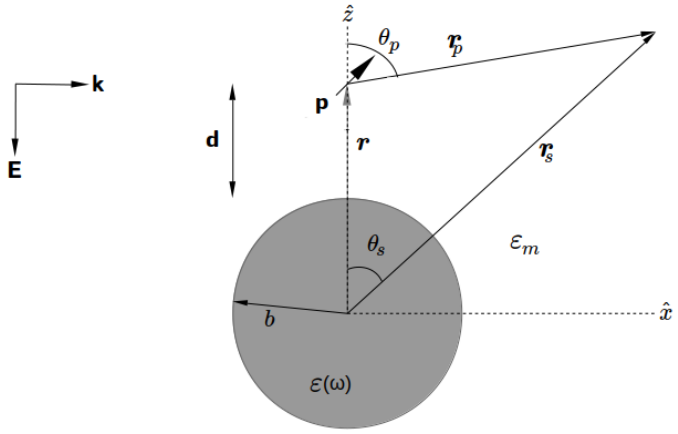

Figure 3.3: Model geometry of the molecule-nanosphere system. The system is surrounded by a homogeneous dielectric medium of dielectric constant ε_m. The nanosphere of radius b, consists of a metal of dielectric constant $\varepsilon(\omega)$. The molecule, modelled as an electric point dipole with a dipole moment $\mathbf{p} = p_z\hat{z} + p_x\hat{x}$, is at a distance $\mathbf{d} = d\hat{z}$ from the metal surface, and oriented at a polar angle θ_p from the z axis. (Adapted from Ref.[62])

molecular dipole via the correspondence principle, and only the dipolar surface plasmon mode contributes to Purcell effect.

In Fig. 3.3, an electric point dipole, which represents the excited molecule, oscillates harmonically above a metallic NS of radius b, at a distance $r = b + d$ from the sphere centre. In the limit where both b and d are small compared to the wavelength of light in the medium, but not so small that non-local effects become important,[3] the electric potentials inside and outside the NS, Φ_{in} and Φ_{out}, respectively, are quasi-static, i.e., they are independent of the propagation wavevector, $\mathbf{k}$, of the electric field. According to Ref.,[62] these potentials can be written as:

$$\Phi_{in} = \sum_{m=0}^{1}\sum_{l=m}^{\infty} A_l \left(\frac{r_s}{b}\right)^l P_{lm}(\cos\theta_s)\cos m\phi, \tag{3.6a}$$

$$\Phi_{out} = \Phi_{dip} + \Phi_{ind}, \tag{3.6b}$$

where

$$\Phi_{dip} = \sum_{m=0}^{1}\left(p_x\delta_{m,1} - p_z\delta_{m,0}\right)\sum_{l=m}^{\infty}\begin{pmatrix} l+1 \\ l+m \end{pmatrix}\frac{r_s^l}{\varepsilon_m r^{l+2}}P_{lm}(\cos\theta_s)\cos m\phi, \tag{3.7a}$$

$$\Phi_{ind} = \sum_{m=0}^{1}\sum_{l=m}^{\infty} B_l \left(\frac{b}{r_s}\right)^{l+1} P_{lm}(\cos\theta_s)\cos m\phi. \tag{3.7b}$$

In Eq. (3.6a), A_l is the complex amplitude of the electric potential inside the NS, where ϕ is the azimuthal angle of the dipole, and l and m are the angular momentum and azimuthal numbers, respectively. Here, $m = 0$ represents the *perpendicular dipole* orientation, while $m = 1$ represents the *parallel dipole* orientation, with respect to the NS surface, respectively. PEF parameters of other dipole orientations are obtained from linear combinations of the above two.[97] In

Eq. (3.7a), the dipole potential due to the molecule, Φ_{dip}, has been re-written in terms of the coordinates: θ_s and r_s, of the NS,[62] Φ_{ind} in Eq. (3.7b) is the induced potential due to the MNP as a result of interacting with the dipole field of the molecule, and P_{lm} is the associated Legendre function of the first kind.

We seek an expression for the complex amplitude, B_l, of the induced potential outside the NS (Eq. (3.7b)), which we can substitute in Eq. (3.7b) to obtain the multipole polarizability of the NS as well as the induced field at the dipole position: $r_s = r, \theta_s = 0$, through $\mathbf{E}_{ind} = -\nabla\Phi_{ind}$. Both the potential and the normal component of the displacement field are continuous at the boundary.[62,71] By applying the boundary conditions at the interface, the orthogonality property of the Legendre polynomial of the first kind, and by eliminating A_l from the resulting equations, the induced multipolar field is obtained as:[62]

$$\mathbf{E}_{ind}(r, \theta_s \to 0) = \sum_{l=1}^{\infty} \frac{\alpha_l(\omega)}{r^3} \frac{(l+1)}{\varepsilon_m r^{2l+1}} \left[p_z(l+1)\hat{z} + \frac{1}{2} l p_x \hat{x} \right], \tag{3.8a}$$

$$\alpha_l(\omega) = a^{2l+1} \frac{l[\varepsilon(\omega) - \varepsilon_m]}{l\varepsilon(\omega) + (l+1)\varepsilon_m}, \tag{3.8b}$$

where $\alpha_l(\omega)$ is the static multipole polarizability of the NS.

Using Eq. (3.8a), the excitation rate enhancement, the Purcell factor, and the normalized rate of power dissipation by the dipole, are obtained respectively from the following equations[9,62,101]

$$\mathbf{E}_{ex} = \frac{|\mathbf{E}_o + \mathbf{E}_{ind}^{l=1}|^2}{|\mathbf{E}_o|^2}, \tag{3.9a}$$

$$\mathbf{P} = \frac{|\mathbf{p} + \mathbf{p}_{ind}|^2}{|\mathbf{p}|^2}, \tag{3.9b}$$

$$\frac{\gamma_{abs}}{\gamma_{rad}^o} = \frac{3\varepsilon_m}{2k^3} \frac{\Im[\mathbf{p}^*.\mathbf{E}_{ind}]}{|\mathbf{p}|^2}, \tag{3.9c}$$

where Eq. (3.9c) was obtained by diving the power dissipated by the point dipole in the presence of the MNP[52,62] by the power radiated by the point dipole in free space. Here, $k = 2\pi\sqrt{\varepsilon_m}/\lambda$ is the wavenumber of light in the medium, λ is the wavelength, $\mathbf{E}_o$ is the source field of the electric dipole, $\mathbf{E}_{ind}^{l=1}$ is the induced dipole field, and $\mathbf{p}_{ind}$ is the induced dipole moment, obtained by comparing Φ_{ind} with Φ_{dip} (see Subsection 3.4.1). Using Eqs. (3.9a)–(3.9c), which hold for different molecule-MNP systems within the QSA, we obtain the following, for the molecule-NS system:

$$\mathbf{E}_{ex} = \left| 1 + \frac{\alpha_1(\omega_{ex})}{r^3}(2\hat{z} - \hat{x}) \right|^2, \tag{3.10a}$$

$$\mathbf{P} = \left| 1 + \frac{\alpha_1(\omega_{em})}{r^3}(2\hat{z} - \hat{x}) \right|^2, \tag{3.10b}$$

$$\frac{\gamma_{abs}}{\gamma_{rad}^o} = \frac{3}{2(kr)^3} \sum_{l=1}^{\infty} \Im[\alpha_l(\omega_{em})] \frac{(l+1)}{r^{2l+1}} \left[(l+1)\hat{z} + \frac{1}{2} l \hat{x} \right]. \tag{3.10c}$$

In the calculation of Purcell factors and excitation rates, we will correct the static dipole polarizability, $\alpha_1(\omega)$, for radiation damping. This correction is necessary for investigating the MNP size-dependence of PEF parameters. Some authors have prescribed a method that takes into account the first-order correction to the quasi-static polarizability due to radiation reaction, as we have demonstrated in Chapter 1. Without this correction, the optical theorem is violated.[66,98,100] However, in the calculation of the normalized dissipation rate of the dipole, we will only correct the dipole term of the static multipole polarizability of the nanoegg for radiation damping. This approach is appropriate for MNPs with radii less than 80 nm.[100,110]

In Refs.,[98,99,111] the enhancement factors were shown to depend on the molecule-NS distance, the NS size, the excitation and emission wavelengths, the intrinsic quantum yield of the molecule, the orientation of the molecular dipole, as well as the antenna efficiency of the NS. Here, we present the major literature results, reproduced using the equations we have presented in this section. Following the approach in Refs.,[99,100,104] we consider a molecule with an arbitrary intrinsic quantum yield. The molecule is at certain distance near a gold nanosphere (AuNS). The host medium is a glass substrate, with $\varepsilon_m = 2.25$.[98] We will assume that the excitation and emission wavelengths are the same, an approach usually adopted in theory work.[67,99,100] However, in calculations involving real molecules,[9,101] this assumption is not used.

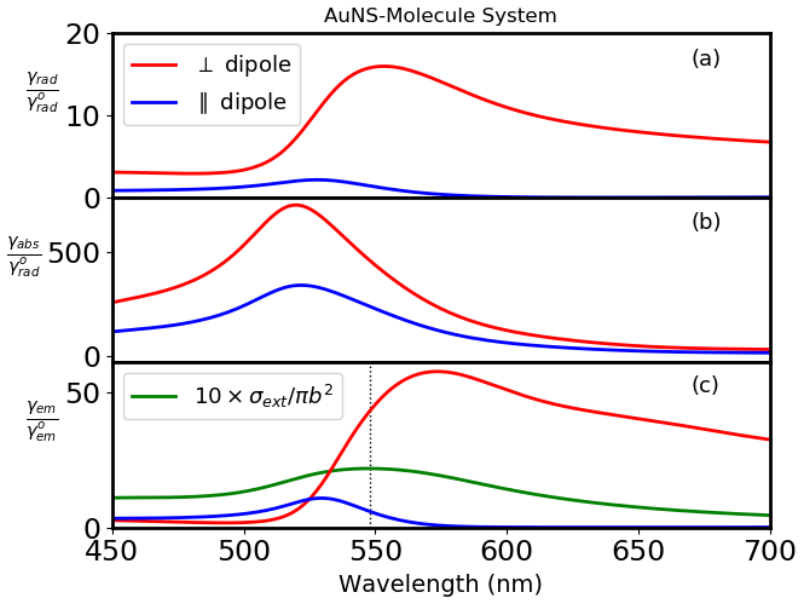

Figure 3.4: Emission wavelength dependence of the: (a) radiative rate enhancement, (b) normalized power dissipation rate, obtained with $l = 20$ multipoles, and (c) emission rate enhancement of a molecular with $Y_o = 0.01$. The molecular dipole is at a distance of 5 nm from a AuNS of radius 20 nm. Red curves: perpendicular dipole orientaion. Blue curves: parallel dipole orientation. Green curve: normalized extinction cross-section of the AuNS.

The rates are more enhanced in the perpendicular dipole orientation of the molecule, as shown in Fig. 3.4. This is because it produces a stronger dipolar

source field compared to the parallel dipole orientation, as we will further show in the next section. The Purcell factor, Fig. 3.4(a), reaches a maximum at an emission wavelength that is either blueshifted (in the case of the parallel dipole) or redshifted (in the case of the perpendicular dipole) from the dipolar LSPR (i.e, the plasmon peak position, indicated by the peak of the green curve in Fig. 3.4(c)) of the NS. The emission rate enhancement (shown in Fig. 3.4(c)), also displays this property. This behaviour is attributed to the different dipole contributions in Eq. (3.10b), i.e., a positive contribution from the perpendicular dipole, and a negative contribution from the parallel dipole. On the other hand, the normalized power dissipation rate (Fig. 3.4(b)) due to either the perpendicular or the parallel dipole orientation, reaches a maximum at an emission wavelength blueshifted from the dipolar LSPR of the NS, although the peak position of the perpendicular case is slightly more blueshifted. This has been referred to as *dissipative resonance*.[99] It is due to the higher-order modes present in the dissipation rate, as shown in Eq. (3.10c). These modes are responsible for plasmon-induced quenching of the enhanced emission.[67,112] As shown in Fig. 3.4(c), the emission rate enhancement is nearly zero at/below the dissipative resonance ($\simeq$ 520 nm for the perpendicular dipole), where the dissipative rate is much greater than the radiative rate. Beyond 520 nm, the dissipative term is decreasing (Fig. 3.4(b)), while the radiative rate is increasing (until it reaches a maximum at $\simeq$ 560 nm, Fig. 3.4(a)), causing the emission rate to increase, until it reaches a maximum at $\simeq$ 575 nm (where the radiative term dominates the dissipative term (Fig. 3.4(c))) . In Fig. 3.4(c), we have set $Y_o = 1\%$ as the intrinsic quantum yield of the molecule. In order to demonstrate the effect of this parameter on the emission rate enhancement, we will revisit this value later in this section.

In Fig. 3.5, we used an emission wavelength of 580 nm, because it is near the wavelength where the emission rate enhancement (Fig. 3.4(c)) is maximum for this arbitrary molecule. In the explanations below, we consider only the contribution from the perpendicular dipole orientation. The excitation rate enhancement, Fig. 3.5(a), decreases gradually as the AuNS-Molecule distance increases, due to an inverse power law behaviour of the induced field (Eq. (3.8a)), that contributes its dipole term to Eq. (3.10a). On the other hand, the dissipative rate is very high at short AuNS-Molecule distances (Fig. 3.5(b)), and approaches zero at long distances, in an inverse power law fashion, due to the nature of Eq. (3.10c). For this reason, the emission rate enhancement (Fig. 3.5(c)) is small at short distances, and reaches a maximum value at $\simeq$ 5 nm, where the radiative term dominates the dissipative term. At long distances, the emission rate enhancement decreases due a decrease in the both the excitation and radiative rate enhancements. When the AuNS radius is varied at constant AuNS-Molecule distance, the dissipation rate (Fig. 3.5(e)) decreases almost linearly with increase in AuNS radius. This is due to the nature of Eq. (3.10c), which is such that larger particles contribute less to the dissipative rate. However, the excitation rate enhancement (Fig. 3.5(d)) reaches a maximum around 33 nm – 35 nm. The emission rate enhancement (Fig. 3.5(f)) follows a similar trend. The size-dependence of PEF in NS-molecule systems has been predicted as $\simeq$ 30 nm,

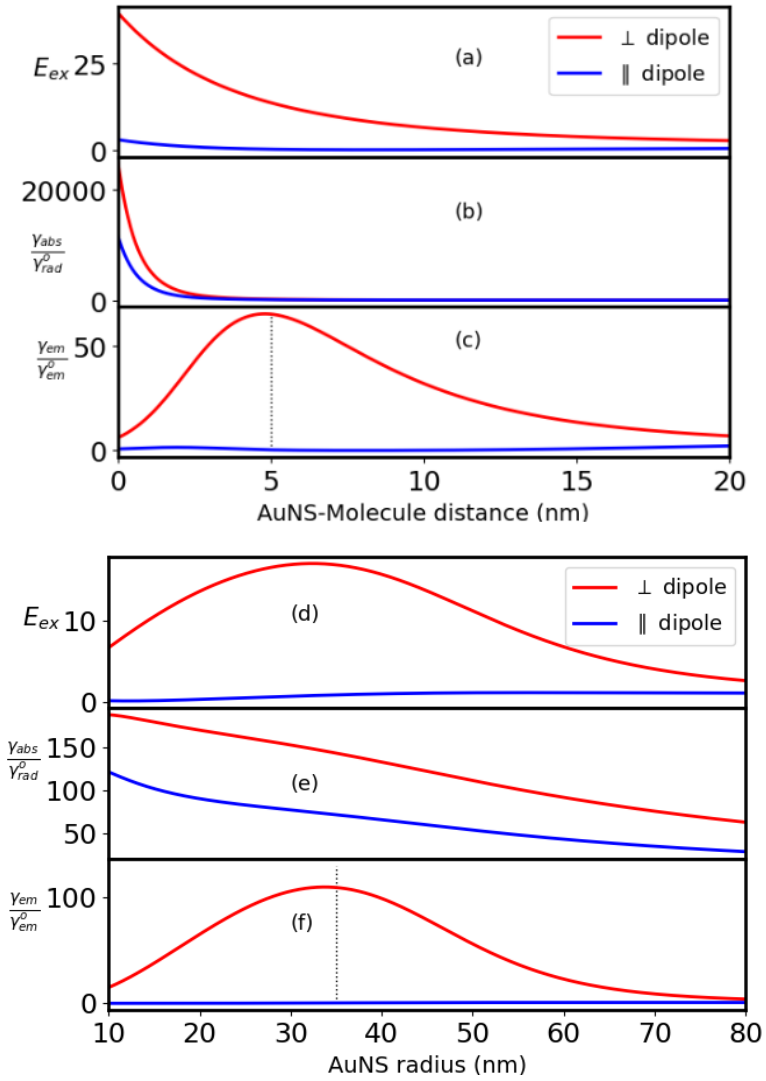

Figure 3.5: (a) Excitation rate enhancement, (b) normalized power dissipation rate, obtained with $l = 20$ multipoles, and (c) emission rate enhancement of a molecular dipole emitting at 580 nm nearby a AuNS of radius 20 nm, as a function of the Molecule-AuNS distance. Dependence of the: (d) excitation rate enhancement, (e) normalized power dissipation rate, obtained with $l = 20$ multipoles, and (f) emission rate enhancement of a molecular dipole emitting at 580 nm at a distance of 5 nm from Au nanospheres of different radii. The dashed line in (c) represents the optimal molecule-NS distance, while the dashed line in (f) represents the optimal NS radius, for a molecule whose $Y_o = 1\%$.

for silver nanospheres, based on full electrodynamic calculations.[111] Hence, the QSA prediction is in good agreement with similar models.

For a molecule with an intrinsic quantum yield of 100% (the dashed line labelled "$Y_o = 1.00$" in Fig. 3.6(a)), the quantum yield enhancement of the molecule (Fig. 3.6(a)) and the antenna efficiency of the AuNS (which corresponds to the black curve labelled "$Y = \eta$" in Fig. 3.6(a)) are equal, i.e., there is no enhancement in quantum yield. This is due to Eq. (3.5b), which is such that when $Y_o \longrightarrow 1$, $Y \longrightarrow \eta$ (Fig. 3.6(a), black curve). Likewise, when $Y_o \longrightarrow \eta$, $Y \longrightarrow Y_o$

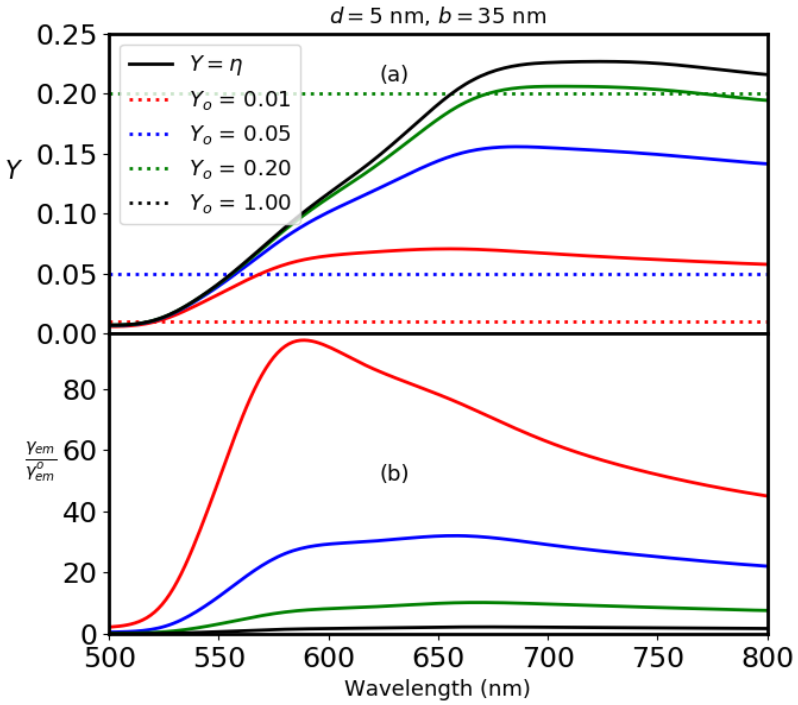

Figure 3.6: Dependence of the: (a) quantum yield enhancement, and (b) emission rate enhancement on the emission wavelength for different intrinsic quantum yields of the molecule. The molecule is at distance of 5 nm from a AuNS of radius 35 nm placed on a glass substrate. For different intrinsic quantum yields (dashed lines, (a)), their corresponding quantum yield enhancements are plotted in (a) (solid lines), and their corresponding emission rate enhancements are plotted in (b) (solid lines).

(Fig. 3.6(a), green curve). Since the antenna efficiency of this AuNS reaches a maximum value of $\simeq 0.22$ between $\simeq 675$ nm and $\simeq 780$ nm (Fig. 3.6(a), black curve), no enhancement in quantum yield occurs for all $Y_o \geq 0.22$. On the other hand, Eq. (3.5b) shows that when $Y_o << \eta$, $Y \longrightarrow \mathbf{P}Y_o$, leading to a significant enhancement in both the quantum yield (Fig. 3.6(a), red and blue curves) and the emission rate of the molecule (Fig. 3.6(b), red and blue curves). This implies that a MNP acts best as a nanoantenna for PEF when its antenna efficiency is greater than the intrinsic quantum yield of the molecule. At long emission wavelengths, away from the dissipative resonance (Fig. 3.5(e)), Y increases dramatically with increase in wavelength, as shown in Fig. 3.6(a), due to a drastic decrease in the dissipation rate of the molecular dipole. The implication of a high of Y_o on the emission rate enhancement of the molecule is shown in Fig. 3.6(b) (black curve), where the $Y_o = 1.00$ molecule leads to nearly-zero enhancement rates for all emission wavelengths.

Fig. 3.7(a) shows that the emission rate enhancement increases with increase in AuNS radius before it peaks around 33 nm at an emission wavelength of $\simeq$ 580 nm. This is accompanied by a corresponding redshift in the dipolar LSPR of the NS, as well as a redshift in the peak emission wavelength. However, in Fig. 3.7(b), the emission rate enhancement increases with decreasing AuNS-Molecule

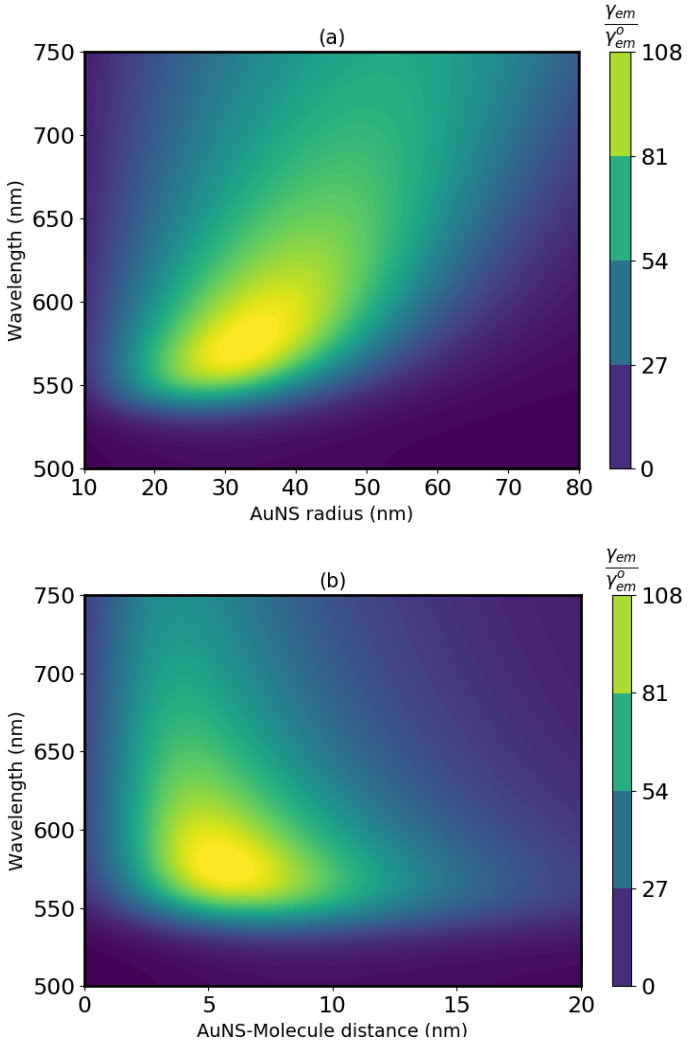

Figure 3.7: Density plots of the emission rate enhancement of a molecule with an intrinsic quantum yield of 0.01. (a) Both the emission wavelength and the AuNS radius are varied at a constant AuNS-Molecule distance of 5 nm. (b) Both the emission wavelength and the AuNS-Molecule distance are varied at a constant AuNS radius of 35 nm.

distance before it reaches a maximum around 5 nm at an emission wavelength of $\simeq$ 580 nm.

3.4 MOLECULE NEAR A NANOEGG [1]

Nanoeggs belong to a group of tunable asymmetric nanostructures capable of supporting multiple LSPR.[13–15,66,71] Their plasmonic behaviour is attributed to the plasmon hybridization of solid and cavity plasmons with different angular momentum numbers, which is symmetry-forbidden in concentric nanoshells.[13,14] A similar description suggests that off-setting the core of a concentric nanoshell causes the dipolar surface plasmon mode to couple to higher-order multi-

[1] this section is part of the publications listed in pp. i.

poles,[66,71] leading to the formation of dipole-active modes. The excitation stage of PEF, which is characterized by local field enhancements, has been investigated for nanoeggs,[14,71] and it was found that their field enhancement factors increase with increasing core-offset. On the other hand, single-particle spectroscopy studies have shown that the LSPR of nanoeggs undergoes a redshift as the core-offset increases.[13,15,66,71]

The emission stage of PEF, which is characterized by enhancement of the intrinsic quantum yield of a molecule, has not been reported previously, for an excited molecule near a nanoegg. The present section focuses on the emission stage of an excited molecule near a dielectric core-metallic shell (DCMS) nanoegg, surrounded by a dielectric medium. The aim of this study is to investigate the impact of the dipole-active modes on the radiative decay rate and quantum yield of the molecule.

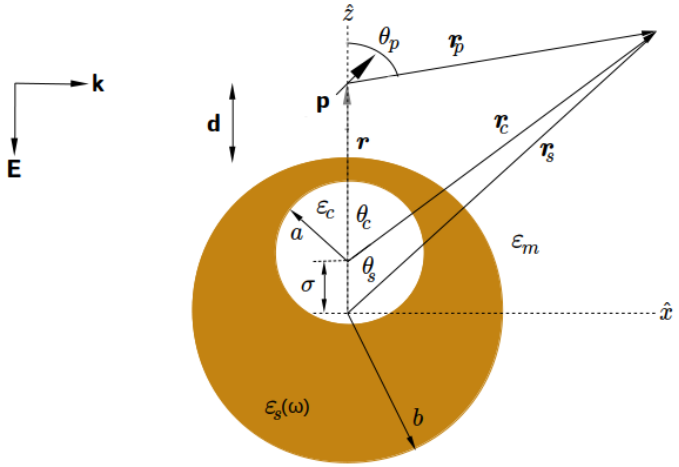

Figure 3.8: Model geometry of the molecule-nanoegg system. The system is surrounded by a homogeneous dielectric medium of dielectric constant ε_m. The nanoegg consists of a metallic shell of dielectric constant $\varepsilon_s(\omega)$, an off-centre core of dielectric constant ε_c, and a core-offset σ. The molecule, modelled as an electric point dipole with a dipole moment $\mathbf{p}$, is at a distance $\mathbf{d} = d\hat{z}$ from the shell surface, and oriented at a polar angle θ_p from the z axis.

In addition to the method used to investigate PEF in the AuNS -Molecule system in the previous section, the solid-harmonic addition theorem (SHAT)[71] will be used to express the shell coordinates in terms of the core coordinates at the core-shell interface of the nanoegg. We will also assume that the molecule is positioned near the surface of the nanoegg in the direction of the core-offset as shown in Fig. 3.8. Two different orientations of the molecular dipole with respect to the nanoegg surface will be considered: the perpendicular orientation, which constitutes the maximum contribution to enhancement factors, often compared to experimental values,[9,101] and the parallel orientation, which gives the minimum contribution.[52,67,110]

3.4.1 *Perpendicular Molecular Dipole*

When the molecular dipole is normal to the surface of the MNP, both the dipole potential and the electric potentials in the core, shell, and medium regions of the MNP, are independent of the azimuth angle ϕ of the dipole.[62,113] For the molecule-nanoegg system, these potentials can therefore be written as[62,71]

$$\Phi_c(r_c,\theta_c) = \sum_{n=1}^{\infty} A_n \left(\frac{r_c}{a}\right)^n P_n(\cos\theta_c), \tag{3.11a}$$

$$\Phi_s(r_s,\theta_s) = \sum_{n=1}^{\infty} \left[B_n \left(\frac{r_s}{b}\right)^n + C_n \left(\frac{b}{r_s}\right)^{n+1}\right] P_n(\cos\theta_s), \tag{3.11b}$$

$$\Phi_m(r_s,\theta_s) = \Phi_{dip}(r_p,\theta_p) + \Phi_{ind}(r_s,\theta_s), \tag{3.11c}$$

where[62,113]

$$\Phi_{dip}(r_p,\theta_p) = \frac{\mathbf{p}.\mathbf{z}}{\varepsilon_m r_p^3} = \frac{\mathrm{p}_z \cos\theta_p}{\varepsilon_m r_p^2} = \sum_{n=1}^{\infty} E_n \left(\frac{r_s}{b}\right)^n P_n(\cos\theta_s), \tag{3.12a}$$

$$E_n = -\frac{\mathrm{p}_z (n+1) b^n}{\varepsilon_m r^{n+2}}, r = b + d, \tag{3.12b}$$

$$\Phi_{ind}(r_s,\theta_s) = \sum_{n=1}^{\infty} D_n \left(\frac{b}{r_s}\right)^{n+1} P_n(\cos\theta_s). \tag{3.12c}$$

Here, r_c and r_s have been normalized with their respective values at the boundaries, and $P_n(u)$ is the Legendre function of the first kind, obtained for the azimuthal number, $m = 0$, which corresponds to the perpendicular dipole orientation. Coefficients A_n, B_n and C_n, and D_n are the complex amplitudes of the electrostatic potential in the core, shell, medium regions of the nanoegg-emitter system respectively, for the normal dipole, and E_n is the amplitude of the source normal dipole potential.

Both the potential and the normal component of the displacement field are continuous at the boundaries.[62,71] By applying the boundary conditions at the core-shell and shell-medium interfaces, the SHAT for $m = 0$[114] at the core-shell interface, the orthogonality property of the Legendre polynomial of the first kind, and by eliminating A_n, B_n and D_n from the resulting equations (see Appendix G), we obtain

$$-\sum_{n=1}^{N} K_{ln} E_n z_n = \sum_{n=1}^{N} K_{ln} C_n y_n + x_l \sum_{n=1}^{N} M_{ln} C_n, \quad l = 1,2,...,N, \tag{3.13}$$

with

$$x_l \equiv \frac{\left[l\varepsilon_c + (l+1)\varepsilon_s(\omega)\right]}{l\left[\varepsilon_c - \varepsilon_s(\omega)\right]}, y_n \equiv \frac{(n+1)\left[\varepsilon_s(\omega) - \varepsilon_m\right]}{\left[n\varepsilon_s(\omega) + (n+1)\varepsilon_m\right]},$$
$$z_n \equiv \frac{(2n+1)\varepsilon_m}{\left[n\varepsilon_s(\omega) + (n+1)\varepsilon_m\right]}, \tag{3.14}$$

and

$$K_{ln} = \begin{pmatrix} n \\ l \end{pmatrix} \frac{a^l \sigma^{n-l}}{b^n} \begin{cases} 1, & n \geq l \\ 0, & n < l \end{cases},$$
$$M_{ln} = (-1)^{l-n} \begin{pmatrix} l \\ n \end{pmatrix} \frac{b^{n+1} \sigma^{l-n}}{a^{l+1}} \begin{cases} 1, & l \geq n \\ 0, & l < n \end{cases}, \tag{3.15}$$

where we have truncated the summation to some finite number N. K_{ln} and M_{ln} are the coupling constants of solid and cavity plasmons with both the same $(l = n)$ and different $(l \neq n)$ angular momentum numbers l and n. Here, Eq. (3.13) forms a system of $N \times N$ simultaneous linear equations with N unknowns, where the C_n terms are the unknowns, since E_n is given by Eq. (3.12b). Given the necessary input parameters, we have written a python code that solves Eq. (3.13) for $N = 15$, which was numerically sufficient to accurately demonstrate the multipolar contributions based on the MNP size we considered.

Finding the C_n terms allows us to obtain the D_n terms. Hence, the induced potential is obtained as

$$\Phi_{ind}(r_s, \theta_s) = \sum_{n=1}^{\infty} \alpha_n(\omega) \frac{\mathrm{p}_z(n+1)}{\varepsilon_m r^{n+2}} \left(\frac{1}{r_s}\right)^{n+1} P_n(\cos\theta_s), \tag{3.16}$$

where

$$\alpha_n(\omega) = b^{2n+1} \left[\frac{(2l+1)\varepsilon_s(\omega)\left[\frac{C_l}{-E_l}\right] + l\left[\varepsilon_s(\omega) - \varepsilon_m\right]}{l\varepsilon_s(\omega) + (l+1)\varepsilon_m} \right], \tag{3.17}$$

is the static multipole polarizability of the nanoegg. From Eq. (3.12c), we obtain the induced dipole potential as

$$\Phi_{ind}(r_s, \theta_s)\Big|_{n=1} = \frac{\mathrm{p}_{z,ind} \cos\theta_s}{\varepsilon_m r_s^2}, \tag{3.18}$$

so that the induced dipole moment in the case of a perpendicular dipole orientation is

$$\mathrm{p}_{z,ind} = \alpha_1(\omega) \frac{2}{r^3} \mathrm{p}_z. \tag{3.19}$$

The induced multipolar field at the dipole position $r_s = r$ and $\theta_s \to 0$ is obtained through $\mathbf{E}_{z,ind}(r_s, \theta_s) = -\nabla \Phi_{z,ind}(r_s, \theta_s)$ as

$$\mathbf{E}_{z,ind}(r_s = r, \theta_s \to 0) = \sum_{n=1}^{\infty} \alpha_n(\omega) \frac{\mathrm{p}_z(n+1)^2}{\varepsilon_m r^{2n+4}} \hat{z}. \tag{3.20}$$

3.4.2 *Parallel Molecular Dipole*

When the molecular dipole is tangential to the surface of the MNP, both the dipole potential and the electric potentials in the core, shell, and medium regions

of the MNP, are dependent on the azimuth angle ϕ of the dipole.[62,113] For the molecule-nanoegg system, these potentials can therefore be written as[62,113]

$$\Phi_c(r_c,\theta_c) = \sum_{n=1}^{\infty} A_n \left(\frac{r_c}{a}\right)^n P_n^1(\cos\theta_c)\cos\phi, \tag{3.21a}$$

$$\Phi_s(r_s,\theta_s) = \sum_{n=1}^{\infty} \left[B_n \left(\frac{r_s}{b}\right)^n + C_n \left(\frac{b}{r_s}\right)^{n+1}\right] P_n^1(\cos\theta_s)\cos\phi, \tag{3.21b}$$

$$\Phi_m(r_s,\theta_s) = \Phi_{dip}(r_p,\theta_p) + \Phi_{ind}(r_s,\theta_s), \tag{3.21c}$$

where[62,113]

$$\Phi_{dip}(r_p,\theta_p) = -\frac{\mathbf{p}.\mathbf{x}}{\varepsilon_m r_p^3} = -\frac{\mathrm{p}_x \sin\theta_p \cos\phi}{\varepsilon_m r_p^2} = \sum_{n=1}^{\infty} E_n \left(\frac{r_s}{b}\right)^n P_n^1(\cos\theta_s)\cos\phi, \tag{3.22a}$$

$$E_n = \frac{\mathrm{p}_x b^n}{\varepsilon_m r^{n+2}}, r = b + d, \tag{3.22b}$$

$$\Phi_{ind}(r_s,\theta_s) = \sum_{n=1}^{\infty} D_n \left(\frac{b}{r_s}\right)^{n+1} P_n^1(\cos\theta_s)\cos\phi. \tag{3.22c}$$

Here, r_c and r_s have been normalized with their respective values at the boundaries, and $P_n^1(u)$ is the associated Legendre function of the first kind, obtained for azimuthal number, $m = 1$, which corresponds to the parallel orientation of the dipole. Coefficients A_n, B_n and C_n, and D_n are the complex amplitudes of the electrostatic potential in the core, shell, medium regions of the nanoegg-molecule system respectively, for the tangential dipole, and E_n is the amplitude of the source tangential dipole potential.

Since the static polarizability of a spherical MNP remains the same for both the perpendicular and parallel dipole orientations,[62,113] we assume that the expression for the polarizability of the nanoegg (Eq. (3.17)) remains the same. Hence, Eqs. (3.13)–(3.15) are retained. However, the coefficients E_l in Eq. (3.12a) and Eq. (3.12b) are now given by Eq. (3.22b), and the induced potential in the case of a parallel dipole becomes (see Appendix G)

$$\Phi_{ind}(r_s,\theta_s) = -\sum_{n=1}^{\infty} \alpha_n(\omega) \frac{\mathrm{p}_x}{\varepsilon_m r^{n+2}} \left(\frac{1}{r_s}\right)^{n+1} P_n^1(\cos\theta_s)\cos\phi. \tag{3.23}$$

From Eq. (3.22c), we obtain the induced dipole potential as

$$\Phi_{ind}(r_s,\theta_s)\Big|_{n=1} = -\frac{\mathrm{p}_{x,ind} \sin\theta_s \cos\phi}{\varepsilon_m r_s^2}, \tag{3.24}$$

so that the induced dipole moment in the case of parallel dipole orientation is

$$\mathrm{p}_{x,ind} = -\alpha_1(\omega)\frac{1}{r^3}\mathrm{p}_x. \tag{3.25}$$

The induced multipolar field at the dipole position $r_s = r$ and $\theta_s \to 0$ is obtained through $\mathbf{E}_{x,ind}(r_s,\theta_s) = -\nabla\Phi_{x,ind}(r_s,\theta_s)$ as

$$\mathbf{E}_{x,ind}(r_s = r, \theta_s \to 0) = \sum_{n=1}^{\infty} \alpha_n(\omega) \frac{\mathrm{p}_x n(n+1)}{2\varepsilon_m r^{2n+4}} \hat{x}. \tag{3.26}$$

3.4.3 *Results and Discussion*

For the perpendicular molecular dipole, the Purcell factor is obtained by substituting Eq. (3.19) into Eq. (3.9b), while for the parallel molecular dipole, it is obtained by substituting Eq. (3.25) into Eq. (3.9b). To obtain the normalized rate of power dissipated by the molecular dipole, we substitute Eq. (3.20) into Eq. (3.9c), for the perpendicular molecular dipole, and Eq. (3.26) into Eq. (3.9c), for the parallel molecular dipole. For each dipole orientation, the emission rate enhancement, the quantum yield enhancement, and the antenna efficiency, are obtained using Eq. (3.5a), Eq. (3.5b), and Eq. (3.5c), respectively.

We will consider a DCMS nanoegg with a gold shell and a silica core of dielectric constant $\varepsilon_c = 2.13$.[104] The gold shell is modelled by the local Drude-Lorentz function given in Eq .(1.10), with the model parameters in table 1. The dimensions of the nanoegg are $a = 15$ nm, $b = 20$ nm, for the following core-offsets $\sigma = 0.0, 0.5, 1.0, 1.5$, and 2.0 nm. The MNP size we have chosen allows us to discuss the enhancement factors of a weak emitter such as crystal violet (CV) near the nanoegg. CV molecules have an intrinsic quantum yield of $Y_o = 2\%$, an intrinsic radiative decay rate $\gamma^o_{rad} = 1.9 \times 10^7$ s^{-1}, and a peak emission wavelength of 640 nm when excited at 633 nm.[9]

As mentioned earlier, we will consider the emission stage of PEF in detail, and mention the overall stage, i.e., excitation and emission, towards the end of this section. The optimal range of MNP-Molecule distance for PEF varies depending on both the MNP geometry and the choice of molecule used. It has been reported as $\sim 3-5$ nm for nanorods,[9,101] $\sim 2-3$ nm for nanospheres,[5,98,100] and $\sim 2-7$ nm for nanoshells.[60,104,115] We have chosen to use a fixed MNP-molecule distance of $d = 5$ nm. The MNP-Molecule system is surrounded by water which has a dielectric constant $\varepsilon_m \approx 1.78$.

Figs. 3.9(**a**) and (**b**) present the normalized rate of non-radiative energy transfer from an excited molecule at $d = 5$ nm for the normal and tangential dipole orientations, respectively. In both plots, the dipolar LSPR undergoes a redshift from 616 nm at $\sigma = 0.0$ nm to 626 nm at $\sigma = 2.0$ nm. For the normal dipole, Fig. 3.9(**a**), at $\sigma > 0.0$ nm, the non-radiative energy transfer rate reaches a maximum at the dipolar LSPR of the nanoegg, while this occurs for the tangential dipole at $\sigma > 1.0$ nm, Fig. 3.9(**b**). This is because the dipolar near-field of the excited molecule is most strongly coupled to the dipolar surface plasmon mode of the nanoegg. A similar behaviour has been reported for spheres[96] and nanorods.[9] However, the energy transfer rate of the normal dipole is more than twice that of the tangential dipole, for the same emission wavelength. The dissipative, blue-shifted peaks in Figs. 3.9(**a**) and (**b**) are due to the coupling of the dipole field of the excited molecule to higher-order ($l \geq 2$) surface plasmon modes of the nanoegg. The impact of the dipole-active modes on the energy transfer rate can be seen in the dramatic increase in the peaks as the core is off-set from $\sigma = 0.0$ nm to $\sigma = 2.0$ nm. For a CV molecule at $d = 5$ nm from the nanoegg, the non-radiative energy transfer rate will therefore increase from $\sim 400 \times \gamma^o_{rad}$ at $\sigma = 0.0$ nm to nearly $1500 \times \gamma^o_{rad}$ at $\sigma = 2.0$ nm, for the normal dipole (Fig.

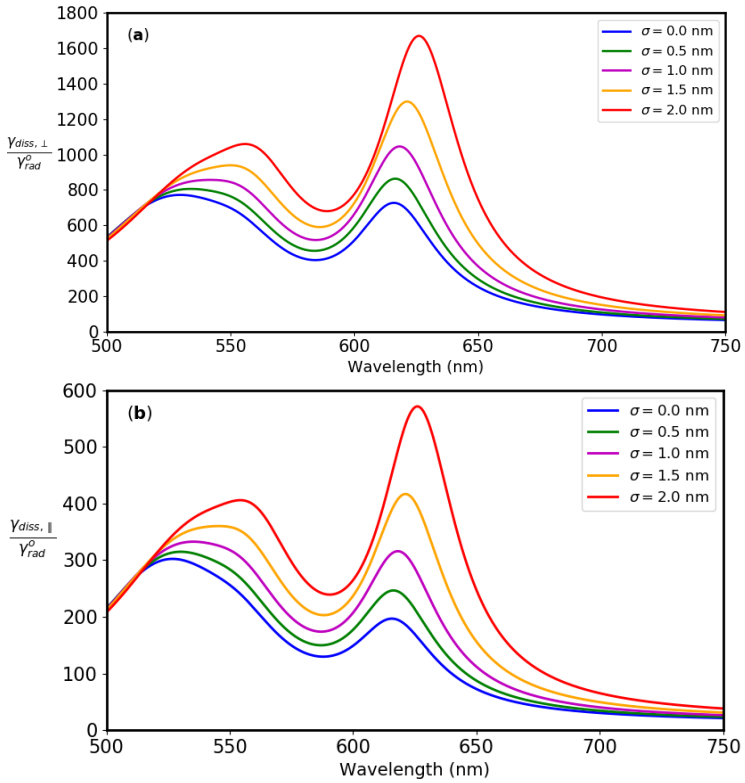

Figure 3.9: Dependence of the normalized rate of power dissipation by the molecular dipole on the core-offset of the nanoegg in the case of (**a**) perpendicular dipole and (**b**) parallel dipole orientations of the molecule near the nanoegg, respectively.

3.9(**a**) at $\lambda = 640$ nm), and from $\sim 100 \times \gamma^o_{rad}$ at $\sigma = 0.0$ nm to nearly $400 \times \gamma^o_{rad}$ at $\sigma = 2.0$ nm, for the tangential dipole (Fig. 3.9(**b**) at $\lambda = 640$ nm).

In Figs. 3.10(**a**) and 3.11(**a**), the Purcell factors of an excited molecular dipole at $d = 5$ nm from the nanoegg are shown for the normal and tangential dipole respectively. As the core-offset increases from $\sigma = 0.0$ nm to $\sigma = 2.0$ nm, both plots show a redshift in the peak emission wavelength at which radiative decay rate enhancement occurs. In comparison to Figs. 3.9(**a**) and (**b**), the peak emission wavelengths for the normal dipole are redshifted from the dipolar LSPR, while the peak emission wavelengths for the tangential dipole are blue-shifted from the dipolar LSPR. The intrinsic radiative decay rate of the molecule is more enhanced for the normal dipole because the induced dipole moment is stronger in the normal orientation of the dipole. For a CV molecule at $d = 5$ nm from the nanoegg, the radiative decay rate will therefore increase from $\sim 40 \times \gamma^o_{rad}$ at $\sigma = 0.0$ nm to nearly $130 \times \gamma^o_{rad}$ at $\sigma = 2.0$ nm, for the normal dipole (Fig. 3.10(**a**) at $\lambda = 640$ nm), and from $\sim 4 \times \gamma^o_{rad}$ at $\sigma = 0.0$ nm to nearly $25 \times \gamma^o_{rad}$ at $\sigma = 2.0$ nm, for the parallel dipole (Fig. 3.11(**a**) at $\lambda = 640$ nm).

When embedded in water, the silica core-gold nanoshell is a passive antenna below 550 nm and an active antenna above 550 nm. This is due to the dependence of the radiative power on the bright mode of the nanoshell, only. The antenna is more efficient in the normal dipole orientation (Fig. 3.10(**b**)) than in the tangential dipole orientation (Fig. 3.11(**b**)). This is because a stronger incident dipole field

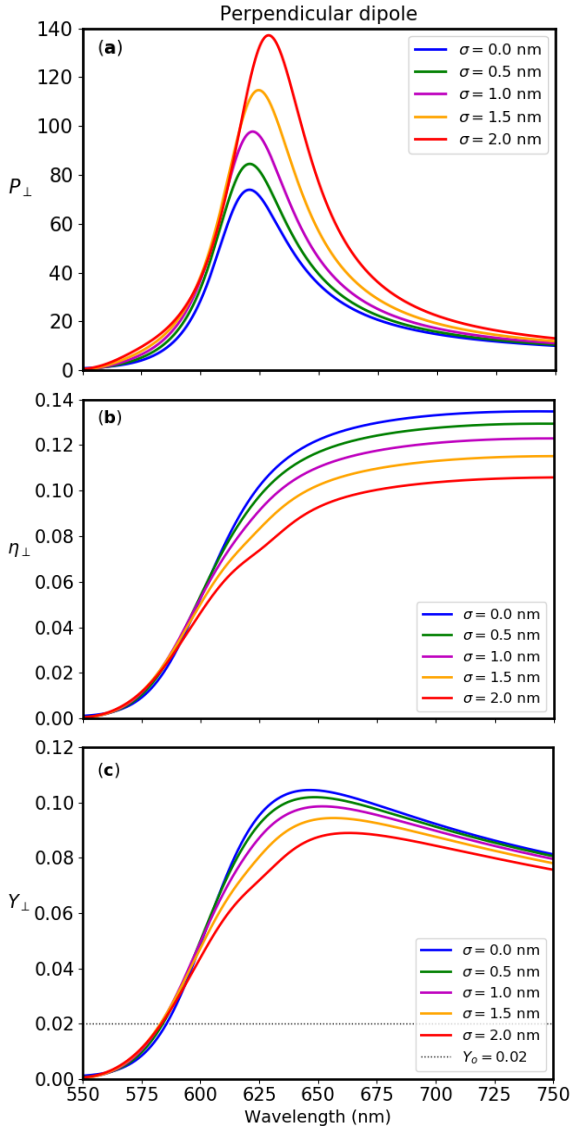

Figure 3.10: Dependence of the (**a**) Purcell factor, (**b**) antenna efficiency, and (**c**) quantum yield of the molecular dipole on the core-offset of the nanoegg, in the case of a perpendicular dipole orientation.

reaches the nanoegg in the normal orientation, causing the antenna to radiate more power. Due to a much higher increase in the absorbed power compared to the increase in radiative power of the nanoegg, as the core-offset increases, the antenna efficiency decreases with increasing core-offset, regardless of the dipole orientation. Beyond the peak emission wavelength, the antenna efficiency plateaus for the normal dipole, because both the radiative and absorptive powers tend towards constant values, while for the tangential dipole, the absorptive power continues to dominate the radiative power.

For the normal dipole, the peak values of the modified quantum yield of the molecule occur at emission wavelengths red-shifted from the dipolar LSPR of the nanoegg (Fig. 3.10(**c**)), while those of the tangential dipole occur at emission wavelengths blue-shifted from the dipolar LSPR (Fig. 3.11(**c**)), due to the different

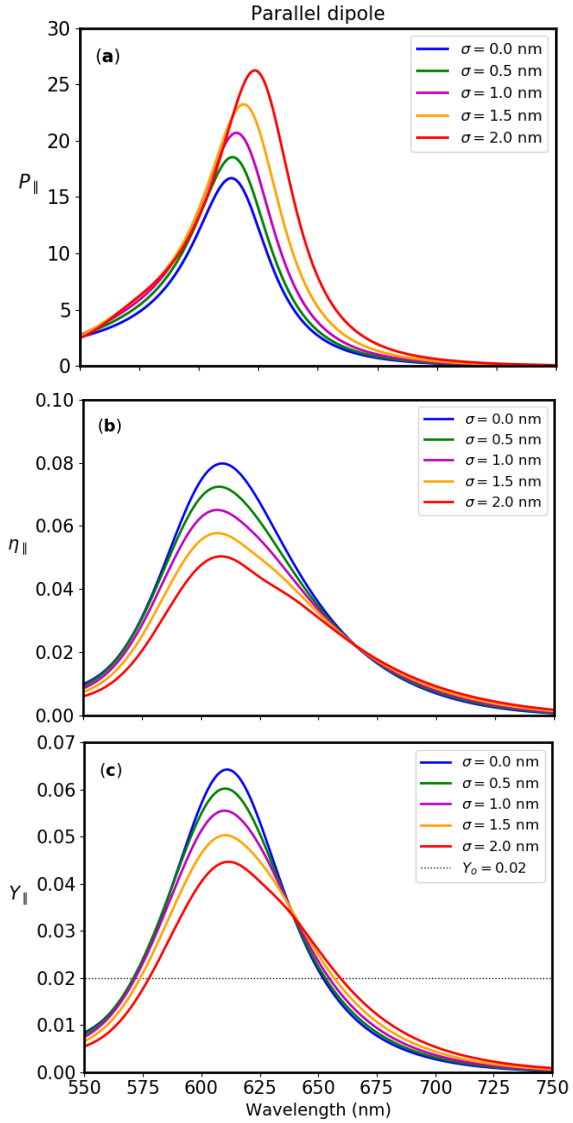

Figure 3.11: Dependence of the (**a**) Purcell factor, (**b**) antenna efficiency, and (**c**) quantum yield of the molecular dipole on the core-offset of the nanoegg, in the case of a parallel dipole orientation.

contributions from the Purcell factor. For a given emission wavelength and MNP-molecule distance, the modified quantum yield of the molecule is always less than the antenna efficiency due to the contribution of the intrinsic non-radiative decay rate of the molecule to the total decay rate of the MNP-molecule system. Although the intrinsic radiative decay rate of the excited molecule is more enhanced near the nanoegg, its intrinsic quantum yield is less enhanced when compared to those of the same molecule near a concentric nanoshell. This is due to the high rate of non-radiative energy transfer from the excited molecule to the nanoegg compared to the nanoshell. The intrinsic quantum yield of the CV molecule emitting at 640 nm increases from 2% to $\sim$ 10% at $\sigma = 0$ nm and from 2% to $\sim$ 8% at $\sigma = 2.0$ nm for the normal dipole (Fig. 3.10 (**c**)), and from 2% to $\sim$ 3.3% at $\sigma = 0$ nm and from 2% to 3% at $\sigma = 2.0$ nm for the tangential dipole (Fig. 3.11(**c**)). Fig. 3.12 shows that for the CV molecule, the quenching of

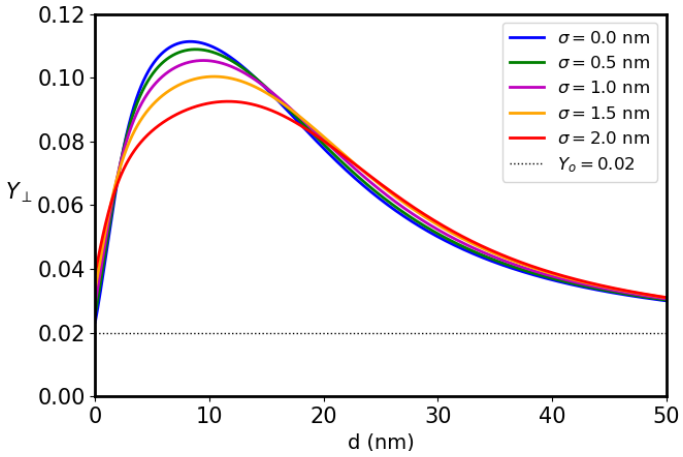

Figure 3.12: Quantum yield enhancement of a CV molecule at the peak emission wavelength $\lambda = 640$ nm, for the core-offsets studied, as a function of its distance from the nanoegg, for a perpendicularly-oriented molecular dipole.

the intrinsic quantum yield which occurs when $Y < Y_o$, is very unlikely, even at short distances ($d \longrightarrow 0$) where the dissipation rate is very high. This is due to the low value of Y_o, so that η is always greater than or equal to Y_o at the peak emission wavelength. At large distances, the strength of the dipolar near-field of the molecule decreases in an inverse power law fashion, causing both the Purcell factor and the dissipation rate to decrease accordingly. As a result, the antenna effect weakens, so that $Y \longrightarrow Y_o$. Likewise, in Fig. 3.12 at $d > 15$ nm, Y approaches the same value regardless of the core-offset. For the core-offsets and MNP size we studied, the optimal range of CV molecule-nanoegg distance for quantum yield enhancement is $\sim 3 - 15$ nm.

We can predict the dependence of the emission rate of the molecule on the core-offset of the nanoegg by using a method proposed in Ref.[99] It makes use of the optical reciprocity theorem, which gives that the Purcell factor and the excitation rate enhancement are identical for the perpendicular dipole.[26,99] Thus, if the molecule is excited at its peak emission wavelength,[99] the Purcell factor is the same as the excitation rate enhancement. The result of this approach is shown in Fig. 3.13. With increasing core-offset, the increase in excitation rate enhancement dominates the decrease in quantum yield enhancement. Hence, the enhanced emission spectrum (Fig. 3.13) of the molecule shows an increase in emission rate with increasing core-offset.

Khatua et al.[9] reported an emission rate enhancement of ~ 1000 for a CV molecule at a distance of 5 nm from the tip of a gold nanorod. In Fig. 3.13(**a**), our theoretical approach shows that at this distance, $\sim 50\%$ of this enhancement factor can be achieved in a CV molecule-DCMS nanoegg system, via small core-offsets in a nanoshell with a radius comparable to the equivalent sphere-volume radius of the nanorod. However, Fig. 3.13(**b**) shows that an emission rate enhancement of ~ 900 can be achieved in the CV molecule-DCMS nanoegg system at shorter distances via a core-offset of $\sigma = 2$ nm. At short distances ($d \longrightarrow 0$), the emission rate enhancement does not decrease to zero because the

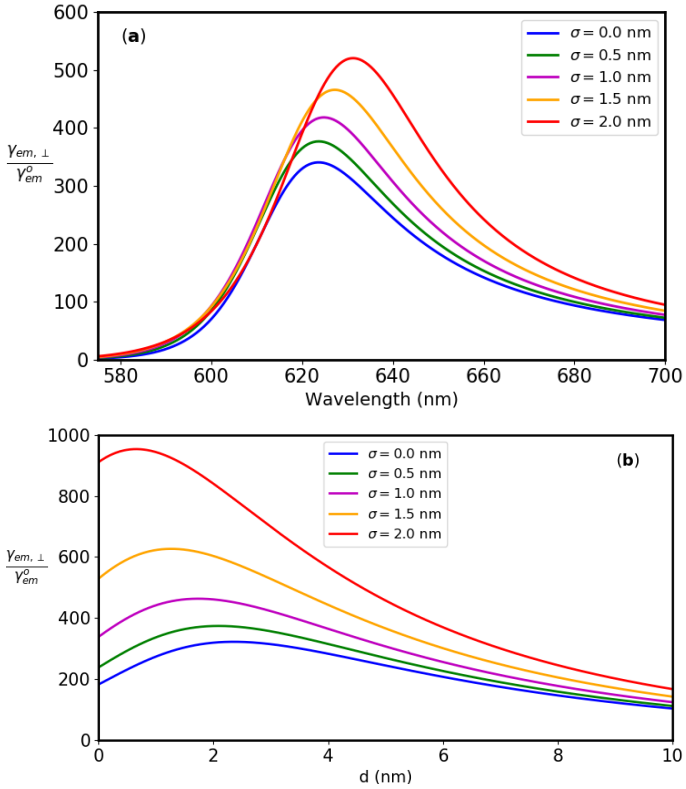

Figure 3.13: Emission rate enhancement of a perpendicularly-oriented CV molecule for the core-offsets studied. (**a**) At $d = 5$ nm from the nanoegg as a function of wavelength assuming that the excitation and emission wavelengths are the same. (**b**) At the peak emission wavelength $\lambda = 640$ nm as a function of its distance from the nanoegg.

excitation rate enhancement is maximum at $d = 0$ and Υ does not decrease to zero (Fig. 3.12), while at large distances, the emission rate enhancement tends to zero because the excitation rate enhancement approaches zero as $\Upsilon \longrightarrow \Upsilon_o$. A similar behaviour has been reported in the nanorod-CV molecule system of Ref.[9]

As we have discussed in Chapter 1, the dependence of the dielectric function of a MNP on the longitudinal propagation wavevector of the incident electric field causes gold nanoparticles to exhibit a size-dependent response, which differs from the bulk response given by Eq. (1.10). This non-local hehaviour places an upper bound on enhancement factors.[55] However, the trends in enhancement factors predicted by both the local and the non-local response remain the same. A major difference exists only in the lower values of enhancement factors and optimal MNP-molecule distances, as well as size-dependent spectral shifts, predicted by the non-local response.[55,104]

4

EXCITON-PLASMON COUPLING

4.1 INTRODUCTION TO CLASSICAL PLEXCITONICS

In hybrid MNP–Molecule systems,[41–43,116–118] molecular excitons – localized or delocalized excitations in molecular aggregates, interact with LSPR of MNPs to from hybrid modes known as *plexcitons*.[116] Plexcitonics is the study of such interactions,[41–43] including the search for molecular resonances that show plasmonic behaviour, which have led to the sub-field of molecular plasmonics.[28] Theoretical methods in classical plexcitonics are borrowed from the classical description of spectroscopy. These methods usually start from a coupled harmonic oscillator (CHO) model (Fig. 4.1), where both the excitonic system and the plasmonic system are treated as damped harmonic oscillators coupled linearly to each other, in the presence of an external driving force. Wu et al.[42] has shown that

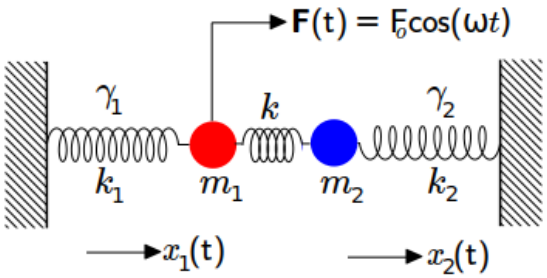

Figure 4.1: A CHO with masses m_1 and m_2 subjected to different damping rates, γ_1 and γ_2, respectively. The oscillators with spring constants $k_1 = m_1\omega_1^2$ and $k_2 = m_2\omega_2^2$, respectively, are coupled linearly through a massless spring of spring constant k. The first oscillator is driving the second oscillator through an external periodic force, $\mathbf{F}(t)$, whose frequency is ω. (Adopted from Ref.[89])

under weak-excitation, where the ground state population of the molecule is not depleted, the extinction cross-section of the MNP is far greater than that of the molecule. As a result, the MNP is the driving oscillator while the molecule is the driven one, since the driving force acting on the molecule is negligible. Hence, the equations of motion of the CHO model of a plexcitonic system are[42] (assuming: $m_1 = m_2 = m = 1$):

$$\ddot{x}_1 + \gamma_1\dot{x}_1 + \omega_1^2 x_1 + k\dot{x}_2 = \Re[F_o e^{-i\omega t}], \tag{4.1a}$$

$$\ddot{x}_2 + \gamma_2\dot{x}_2 + \omega_2^2 x_2 - k\dot{x}_1 = 0, \tag{4.1b}$$

where in the case of exciton-plasmon coupling: $x_1(t) = x_{pl}(t), x_2(t) = x_{ex}(t), \gamma_1 = \gamma_{pl}, \gamma_2 = \gamma_{ex}, \omega_1 = \omega_{pl}$, and $\omega_2 = \omega_{ex}$. Here, ω_{pl} denotes the LSPR of the MNP and ω_{ex} denotes the transition frequency of the molecular exciton, γ_{pl} and γ_{ex}

denote the plasmon and exciton linewidths, i.e., their damping rates, respectively, while k denotes the exciton-plasmon coupling strength. The extinction of the incident radiation applied to the hybrid system is proportional to the power dissipated by the driving oscillator during one period of oscillation.[42,89] With the trial solutions: $x_{pl}(t) = \Re[x^o_{pl}e^{-i\omega t}]$ and $x_{ex}(t) = \Re[x^o_{ex}e^{-i\omega t}]$, this is obtained as follows:

$$C_{ext} \propto \langle F(t)\dot{x}_{pl}(t)\rangle, \tag{4.2a}$$

$$\langle F(t)\dot{x}_{pl}(t)\rangle \propto \omega\Im\left[\frac{\omega^2_{ex} - \omega^2 - i\gamma_{ex}\omega}{(\omega^2 - \omega^2_{pl} + i\gamma_{pl}\omega)(\omega^2 - \omega^2_{ex} + i\gamma_{ex}\omega) - (k\omega)^2}\right]. \tag{4.2b}$$

The interaction of excitons with plasmons leads to different plasmon-induced phenomena, depending on the exciton-plasmon coupling strength. Following the work of Fofang et al.,[116] Antosiewicz et al.[41] have shown that a size-dependent exciton-plasmon coupling in single plexcitonic nanoshells leads to three different coupling regimes: the weak-coupling regime — where the absorption spectrum of the hybrid system is enhanced, the induced transparency regime — where the absorption is partly enhanced and partly reduced, and the strong coupling regime — where no enhancement in the absorption occurs. In Ref.,[118] weak and strong exciton-plasmon coupling regimes were also identified in an MNP-Molecule system, based on a quantum plexcitonics approach. In addition to the MNP-Molecule distance, these coupling regimes also depend on the molecule's dipole oscillator strength and transition linewidth of the ground-state absorption,[42,118] as well as on the MNP size.[119]

4.2 STRONG VERSUS WEAK COUPLING IN PLEXCITONIC SYSTEMS

Resonant interactions between plasmons and excitons occur in plexcitonic systems where some spectral overlap exist between the absorption spectrum of the molecule and the extinction spectrum of the MNP.[9,11,119] In this section, we will present the extinction spectra of a couple of plexcitonic nanoshells, and determine their exciton-plasmon coupling strengths through the CHO model. In addition, we will discuss the MNP-Molecule distance-dependent coupling regimes in a plexcitonic dimer.

When the MNP resonates with the molecule i.e $\omega_{pl} \approx \omega_{ex} \approx \omega_o$, also referred to as zero detuning,[43] the normal modes (plexitonic modes) of the CHO, obtained from the poles of Eq. (4.2b), are two complex frequencies given by:[118]

$$\omega_{\pm} = \omega_o - \frac{i}{4}(\gamma_{pl} + \gamma_{ex}) \pm \sqrt{k^2 - \frac{1}{16}(\gamma_{pl} - \gamma_{ex})^2}, \tag{4.3}$$

whose linewidths are the same. Therefore, the strong coupling regime is reached when $k >> \frac{1}{4}(\gamma_{pl} - \gamma_{ex})$. This leads to a destructive Fano interference between the excitonic and plasmonic modes, which causes the effective absorption spectrum of the hybrid system to split[42] or the splitting of spectral peaks in the emission spectrum of the molecule.[118] This is referred to as *Rabi splitting*, defined

as $\Omega = \omega_+ - \omega_-$.[43] It is an evidence of strong coupling in hybrid optical systems.[43,77,118] In some cases, $\gamma_{pl} >> \gamma_{ex}$, so that $k_o = \frac{1}{4}\gamma_{pl}$ is the critical coupling constant required for the hybrid system to be strongly coupled.[118] On the other hand, the weak coupling regime is reached when $k << \frac{1}{4}(\gamma_{pl} - \gamma_{ex})$. Here, Eq. (4.3) does not lead to new frequencies, instead a constructive Fano interference occurs. This has been referred to as the *energy transfer* regime,[93] where both the absorption and emission spectra of the molecule can be enhanced when it interacts with a MNP.[9,11,41]

4.2.1 *Core-Shell Plexcitons*

Here, we refer to plasmon-exciton resonances formed as a result of strong coupling in core-shell geometries, such as those in Figs. 4.2(a) and (b), as *core-shell plexcitons*. In these geometries, the molecule is usually modelled as the shell, with a certain thickness,[116,119] as shown in Figs. 4.2(a) and (b), respectively, though other configurations exist where a molecular core is used.[41,43]

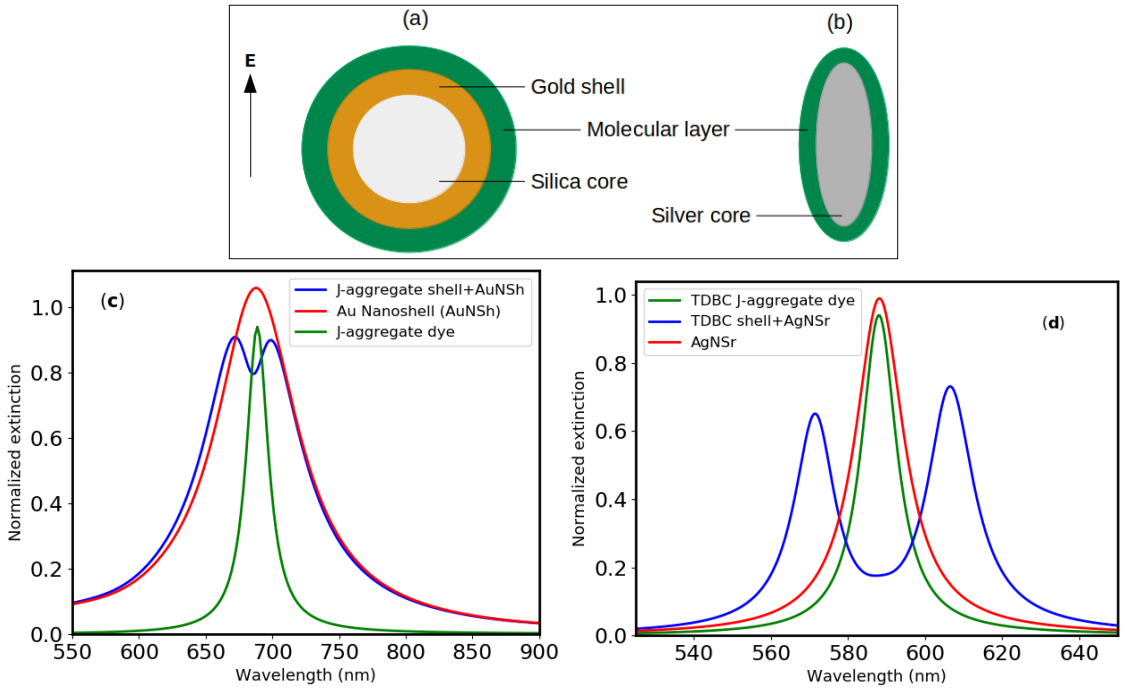

Figure 4.2: (a) and (b): Common model geometries used to investigate exciton-plasmon coupling regimes in classical plexcitonics. An incident electric field **E**, is applied in the direction shown. (c) Normalized extinction spectrum of a J-aggregate dye (2,2'-dimethyl-8-phenyl-5,6,5',6'-dibenzothiacarbocyanine chloride), the gold nanoshell, and the hybrid geometry in (a) based on data from Ref.[116] (d) Normalized extinction spectrum of a TDBC J-aggregate dye, the silver nanospheroid (AgNSr), and the hybrid geometry in (b) based on data from Ref.[119]

In Ref.,[116] a double core-nanoshell made up of a silica core of radius, 45 nm, and a gold shell of thickness, 15 nm, with an external J-aggregate layer of thickness, 4 nm, was used to investigate exciton-plasmon coupling. The

dielectric response of the J-aggregate dye was modelled with a single Lorentzian function of oscillator strength, 0.02, whose transition frequency is such that: $\omega_{ex} \approx \omega_{pl} \approx \omega_0 = 690$ nm, and $\gamma_{ex} \approx 0.052$ eV, $\gamma_{pl} \approx 0.21$ eV, where ω_{pl} corresponds to the LSPR of the gold nanoshell (AuNSh) with a linewidth, γ_{pl}. The plasmon linewidth is the full width at maximum (FWHM) of the extinction spectrum of the AuNSh (Fig. 4.2(c), red curve), while the exciton linewidth is from the data reported in Ref.[116] As shown in Fig. 4.2(c), the plasmon linewidth of the NSh is ≈ 4 times that of the dye. The interaction of the broad NSh spectrum with the narrow dye spectrum, leads to destrucive Fano interference in the extinction spectrum of the hybrid geometry, irrespective of the small extinction of the dye compared to the NSh. The hybrid spectrum therefore splits into two peaks with nearly equal linewidths (Fig. 4.2(c), blue curve). A similar situation is shown in Fig. 4.2(d). In this case, a TDBD J-aggregate dye layer of thickness, 2 nm, and oscillator strength, 0.01, interacts with a prolate AgNSr of half-length, 49 nm, and half-width, 20 nm, such that: $\omega_{ex} \approx \omega_{pl} \approx \omega_0 = 588$ nm, $\gamma_{ex} \approx 0.050$ eV, and $\gamma_{pl} \approx 0.052$ eV (FWHM).[119] Here, the exciton and plasmon linewidths are very close, since the electron damping rates in silver are small compared to those in gold, as we discussed in Chapter 1. Hence, the Rabi splitting in Fig. 4.2(d) (blue curve) was also linked to radiation damping,[119] since electron damping alone could not account for the formation of the plexcitonic resonances and the large exciton induced-transparency dip.

4.2.2 *Plexcitons of a Hybrid Dimer*

In plexcitonic dimers, i.e., a dimer consisting of a molecule and a MNP[77] or a molecule at the gap of a plasmonic dimer,[42] the molecule is often modelled as a dielectric nanoparticle (DNP). This ensures that both the size and shape of the molecule are taken into account.[42,77] In such MNP-DNP systems, strong and weak exciton-plasmon coupling are highly dependent on the MNP–Molecule distance. This approach allows one to employ the CHO model in determining the exciton-plasmon coupling strengths, as well as the plexcitonic resonances in the strong-coupling regime. In addition, Ref.[42] has shown that this approach can reproduce the results of the excitation stage of the point dipole model of PEF which we discussed in Chapter 3, by simply setting the oscillator strength of the molecule to zero. One implication of the plexcitonics approach is that it has revealed that the Gersten-Nitzan model over-predicts the the excitation rate enhancement, as shown in Ref.,[42] during the excitation stage of PEF.

The challenging part of the above approach is the modelling of the dielectric response of the DNP. Though the use of a Lorentzian function is prevalent in plexcitonics literature,[41–43,116,119] it can become quite complicated for complex molecules that have more than one transition frequency, due to the presence of several optical bands, as in the case of light-harvesting complexes.[11,117] Another alternative is to make use of the molecular polarizability,[28,119] but this method is also not straight-forward beyond a single transition. In the following subsection, we present some literature results based on a realistic dielectric function of a

certain semiconductor quantum dot. We will then extend the idea to a plexcitonic system of interest.

A quantum dot at the gap of a silver spheroid dimer

In Fig. 4.3(a), a CdSe nanocrystal centred at the gap of a silver prolate spheroid homodimer is modelled as a spherical DNP — a quantum dot (QD). A single Lorentzian polarizability that reproduces the ground-state absorption of the QD, is proposed as follows:[42]

$$\alpha_{LP}(\omega) = sV\frac{\omega_{ex}^2}{\omega_{ex}^2 - \omega^2 - i\gamma_{ex}\omega}, \tag{4.4}$$

where s denotes the electric dipole oscillator strength of the QD, V is the volume of the QD, ω_{ex} is the transition frequency of the QD exciton, and γ_{ex} is the exciton linewidth. Fig. 4.3(b) shows the uncoupled absorption spectra of the QD and the homodimer, based on a QD of radius, $r = 4$ nm, $s = 0.1$, $\omega_{ex} \approx 2.17$ eV, and $\gamma_{ex} = 0.01$.[42] The surface-to-surface distance of the QD from either spheroid is g, the spheroid dimension is $a = 20$ nm by $b = 5$ nm, and an electric field is applied parallel to the dimer axis, as shown in Fig. 4.3(a).

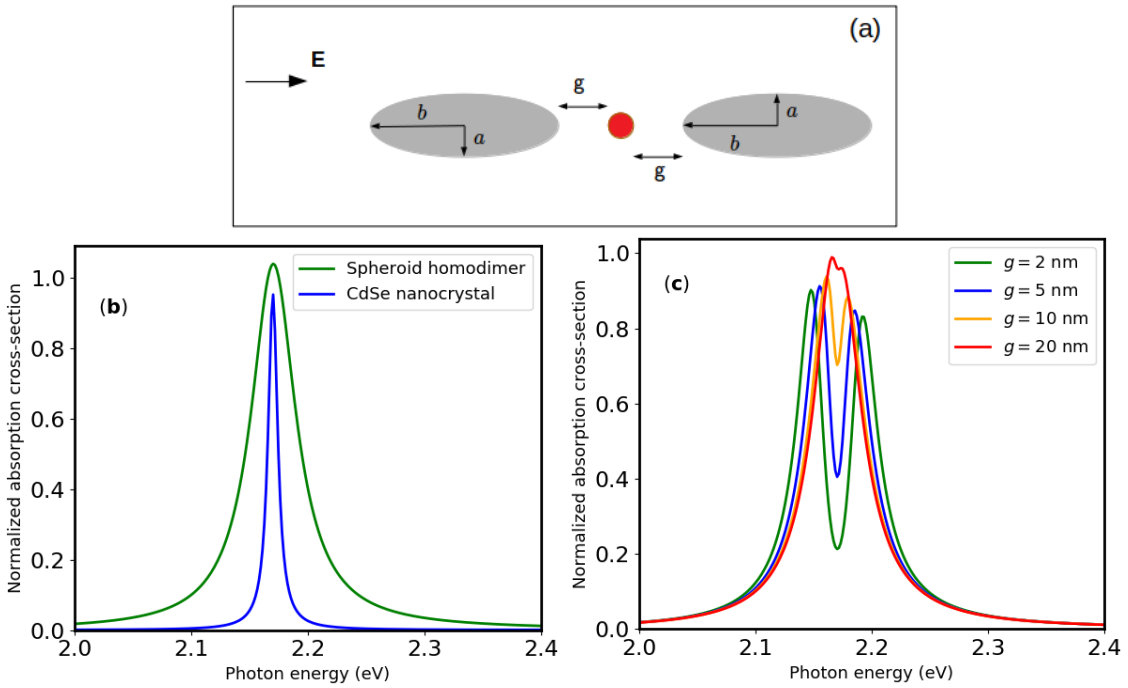

Figure 4.3: (a) Model geometry of a CdSe quantum dot (QD) centred in the gap of a silver spheroid dimer. The QD is treated as a spherical DNP of very small radius. (b) Normalized absorption spectra of the uncoupled LLSPR of the prolate spheroid homodimer and the CdSe QD ground-state transition. Air is taken as the host medium. (Reproduced from Ref.[42]). (c) Normalized absorption spectrum of the coupled system for different values of g.

When $g \approx 2 - 3$ nm, and $s = 0$ (i.e, in the absence of the QD), the LLSPR of the homodimer is: $\omega_{pl} \approx 2.17$ eV, so that the homodimer resonates with

the QD. This leads to destructive Fano interference between the plasmonic and excitonic spectra, which creates a dip in the absorption spectrum of the coupled system (Fig. 4.3(c)). It has already been established in Refs.,[42,119] that for a given plexcitonic system, increasing the oscillator strength or decreasing the exciton linewidth causes the exciton-plasmon coupling strength to increase. This is usually evident from the absorption or scattering spectrum of the coupled system, through an increase in the exciton-induced transparency (EIT) dip.[42] Here, we only present how changes in the value of g affect both the EIT dip and the absorption cross-section. As shown in Fig. 4.3(c), when g increases, the plexcitonic resonances shift towards the EIT dip, causing the two peaks to merge at large values of g. Thus, the Rabi splitting disappears at large g, due to a decrease in the exciton-plasmon coupling strength. This leads to the enhanced spectrum in Fig. 4.3(c).

A single LHCII near the tip of a gold spheroid

In this subsection, we present some preliminary results of an on-going work where we aim to investigate exciton-plasmon coupling in an LHCII-gold nanorod hybrid system. LHCII is the main light-harvesting complex of plants, and certain algae, whose fluorescence quantum yield in a dilute solution is ≈ 0.26.[120] We aim to investigate how exciton-plasmon coupling in a single LHCII-spheroid system affects the quantum yield. In Fig. 4.4(a), a single LHCII is modelled as an electric point dipole at a distance, d, from the tip of a gold prolate spheroid, following the Gersten-Nitzan approach. Since this approach does not take the molecular polarizability into account, the plexcitonics approach used in the excitation stage of PEF in Ref.[42] is adopted here. We hope that this latter approach will enable us to investigate both PEF and strong coupling in the hybrid system. For one of the NR dimensions studied in Ref.,[11] for example, the $a = 44$ nm by $b = 18$ nm NR, $\omega_{pl} \approx 675$ nm, when we approximate the NR to a prolate spheroid. Hence, the LLSPR of the NR will interact resonantly with the excitonic mode of the Q_y absorption band of chlorophyll a (chl a) in LHCII, due to the strong spectral overlap between the uncoupled spectra (Fig. 4.4(b)).

A single Lorenzian polarizability based on Eq. (4.4), that reproduces the absorption spectrum of the Q_y transition of chl a in LHCII is shown in Fig. 4.4(b), with the following model parameters: $\omega_{ex} \approx 675$ nm, $\gamma_{ex} \approx 0.063$ eV, and $s = 0.1$. We treat LHCII as a 3.65 nm$\times$4.5 nm cylindrical DNP, with an equivalent sphere-volume radius of ≈ 3.56 nm, whose volume is accounted for but not its dielectric polarizability, in order to avoid a shape-induced resonance in ω_{ex}. This assumption is reasonable, since the spheroid volume is about 316 times that of a single LHCII. As shown in Fig. 4.4(c), the absorption spectrum of the coupled system does not show any MNP-Molecule distance-dependent Rabi splitting. This is because the interaction is dominated by the contribution from the large dipole polarizability of the spheroid compared to that of LHCII. As explained in Ref.,[119] the exciton-plasmon coupling constant is inversely proportional to the MNP volume. An attempt to investigate this property for the LHCII-spheroid system presents some challenge, since smaller nanorods produce blueshifted

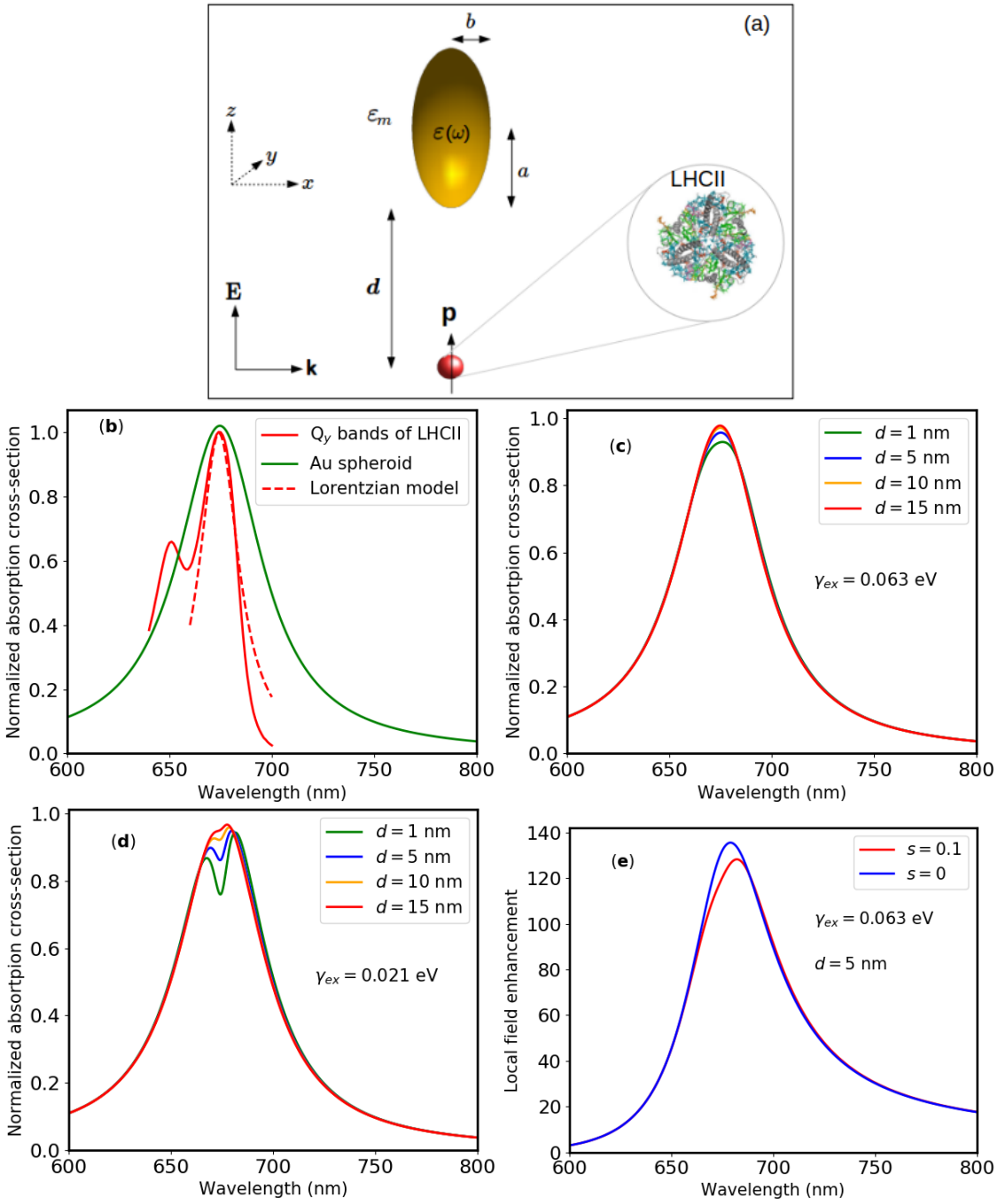

Figure 4.4: (a) Model geometry of a single LHCII-Au spheroid system. In the point dipole model, the single LHCII is modelled as a point dipole with dipole moment **p**, near the tip of the spheroid. In the plexcitonics approach, it is modelled as a DNP with finite dimensions and a Lorentzian polarizability. (b) Normalized absorption spectra of the uncoupled LLSPR of the gold spheroid and the Q_y bands of LHCII. (c) and (d) Normalized absorption cross-sections of the coupled system for two different exciton linewidths. (e) Dependence of the local field near the single LHCII on the excitation wavelength, in both the point dipole model ($s = 0$) and the DNP model ($s = 0.1$).

LLSPR, which will not resonate with the Q_y excitons of chl a in LHCII, and will

involve a different NR size than the experimental data in Ref.,[11] which we intend to reproduce theoretically.

However, in Fig. 4.4(d), some noticeable splitting does occur in the hybrid spectra when the exciton linewidth is decreased from 0.063 eV to 0.021 eV. This shows that our Lorentzian model might have been inadequate, since it is too broad towards the bottom of the spectrum. Therefore, a Gaussian model of the molecular polarizability of the Q_y transition of chl a in LHCII is a better alternative that we intend to investigate in the near future. Fig. 4.4(e) shows that the enhanced local field near the molecule, at the LLSPR of the NR, is less enhanced when the molecule is absorbing i.e when $s = 0$. In addition, the DNP model leads to a slightly more redshifted peak position of the enhanced dipole field. However, away from their peak values (i.e, peak values of the $s = 0$ and $s = 0.1$ curves in Fig. 4.4(e)), the enhancement factors based on both models are the same. Nevertheless, an inclusion of the Q_y transition of chl b in LHCII in a Lorentzian or Gaussian model of the molecular polarizability might lead to a different trend in the two models at short excitation wavelengths, since the Q_y transition of chl b occurs around 650 nm, where some spectral overlap does exist between the NR spectrum and LHCII absorption (Fig. 4.4(b)).

5

CONCLUSION

In Chapter 1, we started by introducing some theoretical background for this thesis, while presenting an overview of the interdisciplinary field of plasmonics. Having adopted the QSA, within the LRA, some of its shortcomings were mentioned alongside some approaches used in literature to improve the theory. These improvements allowed us to investigate the size-dependence of the dipolar LSPR of silver and gold spheres and prolate spheroids, which helped to clarify the issue of aspect ratio versus size-dependent dipolar LSPR in nanorods (nanospheroids).

We started Chapter 2 by introducing different kinds of plasmons. Of particular interest to us were surface plasmons, were we investigated some of the plasmonic behaviour of both propagating and localized surface plasmons. While the former propagate as surface waves along metal-dielectric interfaces, the latter are particle-confined oscillations whose resonances depend on particle geometry and size, as well as on the dielectric environment and light polarization. We have identified and discussed some important relationships between the LSPR of the most common plasmonic nanostructures. We believe that these relationships extend to other plasmonic nanostructures, especially to nanostructures where hybrid plasmons are present. However, we have limited our discussion to nanostructures with smooth corners in the Rayleigh regime, where both an analytical approach and a quasistatic description are possible. We derived their dipolar and multipolar LSPR using a combination of the Drude model, the Rayleigh approximation, and the Fröhlich condition. Our results have shown that the LSPR depends strongly on the geometric factors of the nanostructures, which emphasizes the shape dependence of the LSPR. The approach we adopted led us to several formulas for calculating the LSPR of the most common nanostructures in plasmonics literature. Some of these formulas have not been reported previously (such as the dipolar and multipolar LSPR of a nanorice) especially in the manner in which we have simplified them using geometric factors and the mutual relationships between nanostructures. Beside LSPR, these relationships also exist in other optical properties of the nanostructures, such as the polarizability. Some of the formulas we have derived are handy (those for the dipolar resonances), and can easily be used for estimating the LSPR of single metallic nanostructures in different environments. Also discussed in Chapter 2 is the plasmonic behaviour in dimers, were we investigated plasmon coupling in both homo and hetero dimers. Our results show that the OSA captures most of the interesting optical properties of plasmonic dimers, which enabled us to extend the theory to a NE-NR heterodimer. We have studied the effect of dipole–dipole plasmon coupling on the scattering and absorption cross-sections of the NE-NR heterodimer. The dimer consists of a silica core–gold shell NE and a gold NR. By using a dipolar quasi-static approach, and considering only the case of an incident electric field parallel to the dimer axis, at constant NE size, we found

that plasmon coupling in the NE-NR dimer is dependent on both the absorption cross-section of the NR and the plasmon detuning frequency. This is regardless of whether the NR is at a blueshifted, resonant, or redshifted plasmon peak position with respect to the plasmon peaks of the NE. When the parameters in the plasmon coupling terms — the NR and NE sizes, their non-interacting polarizabilities, and the dimer gap — are kept constant, plasmon-induced transparency and mode splitting occur in both the absorption and scattering cross-sections of the dimer as the detuning frequency is tuned via the core-offset of the NE. However, the plasmon-induced LSPR shifts increase slightly with increasing NR size. In all NR sizes and plasmon peak positions studied, the absorption and scattering spectra of the dimer are enhanced compared to the spectra of the non-interacting NE or NR, respectively. However, larger nanorods lead to more enhanced spectra due to their large polarizabilities. Compared to a NE-NS dimer, the NE-NR dimer features more enhanced spectra but the trends that lead to induced transparency are similar in both dimers.

Chapter 3 focuses on some theory behind one of the most fascinating applications of plasmonics — plasmon-enhanced fluorescence. The theory was independently developed by Gersten-Nitzan and Ford-Weber, within the QSA, though some improvements have been made on theory by several authors in recent years. The background equations used for calculating PEF parameters are entirely dependent on MNP size, geometry, and composition, the molecule's intrinsic quantum yield, and the host medium. PEF parameters change dramatically when any of the above factors is altered. By reviewing some of the literature on PEF, we presented the PEF parameters of an arbitrary molecule near a gold nanosphere, where the effect of varying the NS size, the NS-Molecule distance, and the molecule's intrinsic quantum, on PEF, were investigated. This concept was then extended to a nanoegg-molecule system, where we calculated PEF parameters for a DCMS nanoegg-CV molecule system. Off-setting the core of the DCMS nanoparticle, embedded in a dielectric medium and placed near an excited molecule, causes both the dipolar near-field of the molecule and the dipolar surface plasmon mode to couple to all surface plasmon modes of the nanoshell. This process leads to the formation of dipole-active modes in the nanoshell, which increases the induced dipole moment on the molecule. As a result, the Purcell factor of the molecule increases with increasing core-offset. Likewise, the non-radiative energy transfer rate from the molecule to the nanoegg also increases, reaching a maximum at the dipolar LSPR of the nanoegg. Within the quasistatic limit, we have investigated the impact of these dipole-active modes on the radiative decay rate and quantum yield of a CV molecule placed near the nanoegg. The theoretical model we adopted shows that the nanoegg ($\sigma > 0$ nm) is a more efficient antenna for enhancement of the radiative decay rate compared to the concentric nanoshell ($\sigma = 0$ nm), while the concentric nanoshell is a more efficient antenna for enhancement of quantum yield. However, a method based on optical reciprocity, has shown that the emission rate of the molecule is more enhanced near the nanoegg due to the dominant contribution from the excitation rate enhancement. We have considered both the normal and tangential orientations of the dipole moment of the CV molecule with respect to the nanoegg

surface. We found that the tangential dipole is less enhanced. In addition, the peak wavelengths of the optimal enhancement factors are redshifted from the dipolar LSPR of the nanoegg. This result is consistent with PEF calculations in other plasmonic nanostructures within the LRA. Compared to a nanorod-emitter system, our theoretical model also shows that by using a nanoegg whose size is comparable to the nanorod, it is possible to achieve similar enhancement factors, via large core-offsets in a nanoegg-emitter system.

In Chapter 4, we have briefly reviewed the concept of strong versus weak exciton-plasmon coupling in certain plexcitonic systems, based on the CHO model. Previous studies have already established that PEF and enhanced absorption are plasmon-induced phenomena associated with weak exciton-plasmon coupling, while Rabi splitting is an evidence of strong coupling. Also discussed include the point dipole model versus the DNP model of PEF, in the excitation stage, were we used the former to investigate exciton-plasmon coupling. Here, we presented only a couple of preliminary results, and mentioned the challenges and future directions of an on-going project. Our ultimate goal is to extend the DNP model to the emission stage of PEF in an LHCII-AuNR system, and compare the PEF parameters obtained to those of the point dipole model and experimental data. The proposed model will include only the Q_y optical band of chl a in LHCII. We therefore hope that Occam's razor will play out, else a model that also considers the Q_y optical band of chl b in LHCII will be required.

F

APPENDIX A: STATIC POLARIZABILITIES

FROM NANORICE TO NANOSPHERE POLARIZABILITIES

Following the results of Refs.,[73,74] the multipole polarizability of the nanorice in Fig. 2.3(a) is:

$$\alpha_{lm}(\omega) = f_s^{2l+1} N_{lm} \frac{\varepsilon_s(\omega) y_{lm} P'_{lm}(v_s) P_{lm}(v_s) - \varepsilon_m x_{lm} P_{lm}(v_s) P'_{lm}(v_s)}{\varepsilon_s(\omega) y_{lm} P'_{lm}(v_s) Q_{lm}(v_s) - \varepsilon_m x_{lm} P_{lm}(v_s) Q'_{lm}(v_s)}, \tag{A.1}$$

with

$$x_{lm} = 1 + \left[\frac{\frac{Q_{lm}(v_s)}{P_{lm}(v_s)} [\varepsilon_s(\omega) - \varepsilon_c]}{\varepsilon_c \frac{Q_{lm}(v_c)}{P_{lm}(v_c)} - \varepsilon_s(\omega) \frac{Q'_{lm}(v_c)}{P'_{lm}(v_c)}} \right] \tag{A.2}$$

and

$$y_{lm} = 1 + \left[\frac{\frac{Q'_{lm}(v_s)}{P'_{lm}(v_s)} [\varepsilon_s(\omega) - \varepsilon_c]}{\varepsilon_c \frac{Q_{lm}(v_c)}{P_{lm}(v_c)} - \varepsilon_s(\omega) \frac{Q'_{lm}(v_c)}{P'_{lm}(v_c)}} \right], \tag{A.3}$$

where the respective symbols retain their usual meanings as defined in Chapter 2.

In the sphere limit, $v_c = a/f_c$ and $v_s = b/f_s$, (where $f_s = f_c$ for confocal spheroids) we make use of Eq. 2.16 to obtain the following equations:

$$\alpha_l(\omega) = b^{2l+1} \frac{l[\varepsilon_s(\omega) x_l - \varepsilon_m y_l] b^{2l+1}}{\varepsilon_s(\omega) l x_l + \varepsilon_m (l+1) y_l} \tag{A.4}$$

with

$$x_l = 1 - \frac{(l+1)[\varepsilon_s(\omega) - \varepsilon_c]}{l\varepsilon_c + (l+1)\varepsilon_s(\omega)} q^{2l+1} \tag{A.5}$$

and

$$y_l = 1 + \frac{l[\varepsilon_s(\omega) - \varepsilon_c]}{l\varepsilon_c + (l+1)\varepsilon_s(\omega)} q^{2l+1}, \tag{A.6}$$

where $q = a/b$ is the aspect ratio of the nanoshell, and $\alpha_l(\omega)$ is the multipole polarizability of the concentric nanoshell in Fig. 2.3(b).

The multipole polarizability of the solid prolate spheroid is obtained by setting: $\varepsilon_s(\omega) = \varepsilon_c$, in Eqs. (A.2) and (A.3). This leads to

$$\alpha^s_{lm}(\omega) = f_s^{2l+1} N_{lm} \frac{\varepsilon(\omega) - \varepsilon_m}{\varepsilon(\omega) \frac{Q_{lm}(v_s)}{P_{lm}(v_s)} - \varepsilon_m \frac{Q'_{lm}(v_s)}{P'_{lm}(v_s)}}. \tag{A.7}$$

The multipole polarizability of the cavity prolate spheroid is obtained by changing ε_m to ε_c as well as v_s to v_c in Eq. A.7 and reversing the positions of $\varepsilon(\omega)$ and ε_c in the resulting equation. This leads to

$$\alpha_{lm}^{c}(\omega) = f_c^{2l+1} N_{lm} \frac{\varepsilon_c - \varepsilon(\omega)}{\varepsilon_c \frac{Q_{lm}(v_c)}{P_{lm}(v_c)} - \varepsilon(\omega) \frac{Q'_{lm}(v_c)}{P'_{lm}(v_c)}}, \tag{A.8}$$

where[74]

$$N_{lm} = i^m \frac{(l-m)!(l+m)!}{(2l-1)!!(2l+1)!!}, \quad \text{(prolate)} \tag{A.9a}$$

$$N_{lm} = (-1)^{l+m} i^{-(m+1)} \frac{(l-m)!(l+m)!}{(2l-1)!!(2l+1)!!}, v \to iv, \quad \text{(oblate)}. \tag{A.9b}$$

Similar steps as above (for example, setting $q = 0$ in Eqs. (A.5) and (A.6), and reversing the positions of the dielectric constants in Eq. (A.4)) are used to obtain the multipole polarizability of the solid and cavity sphere, respectively, as follows:

$$\alpha_l^s(\omega) = b^{2l+1} \frac{l[\varepsilon(\omega) - \varepsilon_m]}{l\varepsilon(\omega) + (l+1)\varepsilon_m} \tag{A.10}$$

and

$$\alpha_l^c(\omega) = a^{2l+1} \frac{l[\varepsilon_c - \varepsilon(\omega)]}{l\varepsilon_c + (l+1)\varepsilon(\omega)}, \tag{A.11}$$

where a is the cavity sphere radius and b is the solid sphere radius.

DIPOLE POLARIZABILITIES OF CERTAIN PLASMONIC DIMERS

Nanosphere Heterodimer

Consider two nearby nanospheres of radii r_1 and r_2, respectively, with a surface to surface distance given by g. The centre to centre distance is therefore $l = g + r_1 + r_2$. Following the dipolar-quasistatic approach described in Chapter 2, the local electric field on each nanosphere, due to an incident field, E_0, applied to the dimer, can be written respectively as:

$$E_{1m}^{loc} = E_0 + (-1)^m 2^{1-m} \frac{\alpha_2 E_{2m}^{loc}}{4\pi l^3}, \tag{A.12a}$$

$$E_{2m}^{loc} = E_0 + (-1)^m 2^{1-m} \frac{\alpha_1 E_{1m}^{loc}}{4\pi l^3}, \tag{A.12b}$$

where $m = 1$ corresponds to the case of a field applied perpendicular to the dimer axis, and $m = 0$ corresponds to a field applied parallel to the dimer axis, and α_1 and α_2 are the respective effective dipole polarizabilities of the nanospheres. Solving Eqs. (A.12a) and (A.12b) simultaneously leads to:

$$E_{1m}^{loc} = E_0 \frac{1 + (-1)^m 2^{1-m} \frac{\alpha_2}{4\pi l^3}}{1 - 2^{2(1-m)} \frac{\alpha_1 \alpha_2}{(4\pi l^3)^2}}, \tag{A.13a}$$

$$E_{2m}^{loc} = E_0 \frac{1 + (-1)^m 2^{1-m} \frac{\alpha_1}{4\pi l^3}}{1 - 2^{2(1-m)} \frac{\alpha_2 \alpha_2}{(4\pi l^3)^2}}, \tag{A.13b}$$

so that the effective dipole polarizability of the dimer is:

$$\alpha_m^{dimer} = \frac{\alpha_1 + \alpha_2 + \alpha_1\alpha_2\frac{(-1)^m 2^{1-m}}{2\pi l^3}}{1 - 2^{2(1-m)}\frac{\alpha_2\alpha_2}{(4\pi l^3)^2}}. \tag{A.14}$$

In the homodimer case, $r_1 = r_2 = r$, and $\alpha_1 = \alpha_2$, Eq. (A.14) therefore reduces to Eq. (2.30).

Nanorod Heterodimer

We can obtain the longitudinal dipole polarizability of the prolate spheroid dimer described in Chapter 2 by writing the local field on each of the prolate spheroids, due to an accident field, E_0, parallel to the dimer axis, as follows:

$$E_1^{loc} = E_0 + E_2^{loc}\frac{3\alpha_2(1 - L_{\mu 2})}{4\pi l(l^2 - f_2^2)}, \tag{A.15a}$$

$$E_2^{loc} = E_0 + E_1^{loc}\frac{3\alpha_1(1 - L_{\mu 1})}{4\pi l(l^2 - f_1^2)}, \tag{A.15b}$$

where the symbols retain their usual meanings as defined in Chapter 2. Solving Eqs. (A.15a) and (A.15b) simultaneously leads to the following:

$$E_1^{loc} = E_0\frac{1 + \frac{3\alpha_2(1-L_{\mu 2})}{4\pi l(l^2-f_2^2)}}{1 - \frac{9\alpha_1\alpha_2(1-L_{\mu 1})(1-L_{\mu 2})}{(4\pi l)^2(l^2-f_1^2)(l^2-f_2^2)}}, \tag{A.16a}$$

$$E_2^{loc} = E_0\frac{1 + \frac{3\alpha_1(1-L_{\mu 1})}{4\pi l(l^2-f_2^2)}}{1 - \frac{9\alpha_1\alpha_2(1-L_{\mu 1})(1-L_{\mu 2})}{(4\pi l)^2(l^2-f_1^2)(l^2-f_2^2)}}, \tag{A.16b}$$

from which we obtain the following effective dipole polarizabilties:

$$\alpha_1^{eff} = \alpha_1\frac{1 + \frac{3\alpha_2(1-L_{\mu 2})}{4\pi l(l^2-f_2^2)}}{1 - \frac{9\alpha_1\alpha_2(1-L_{\mu 1})(1-L_{\mu 2})}{(4\pi l)^2(l^2-f_1^2)(l^2-f_2^2)}}, \tag{A.17a}$$

$$\alpha_2^{eff} = \alpha_2\frac{1 + \frac{3\alpha_1(1-L_{\mu 1})}{4\pi l(l^2-f_2^2)}}{1 - \frac{9\alpha_1\alpha_2(1-L_{\mu 1})(1-L_{\mu 2})}{(4\pi l)^2(l^2-f_1^2)(l^2-f_2^2)}}, \tag{A.17b}$$

$$\alpha^{dimer} = \alpha_1^{eff} + \alpha_2^{eff}, \tag{A.17c}$$

where α^{dimer} is the dimer polarizability given by Eq. (2.32).

APPENDIX B: MOLECULE NEAR A NANOEGG

PERPENDICULAR MOLECULAR DIPOLE

At the boundaries, both the potential and the normal component of the displacement field must be continuous, leading to the following boundary conditions:[71]

$$\Phi_c\Big(r_c,\theta_c\Big)\Big|_{r_c=a} = \Phi_s\Big(r_s,\theta_s\Big)\Big|_{r_c=a}, \tag{B.1}$$

$$\Phi_s\Big(r_s,\theta_s\Big)\Big|_{r_s=b} = \Phi_m\Big(r_s,\theta_s\Big)\Big|_{r_s=b}, \tag{B.2}$$

$$\varepsilon_c\frac{\partial\Phi_c\Big(r_c,\theta_c\Big)}{\partial r_c}\Big|_{r_c=a} = \varepsilon_s(\omega)\frac{\partial\Phi_s\Big(r_s,\theta_s\Big)}{\partial r_c}\Big|_{r_c=a}, \tag{B.3}$$

$$\varepsilon_s(\omega)\frac{\partial\Phi_s\Big(r_s,\theta_s\Big)}{\partial r_s}\Big|_{r_s=b} = \varepsilon_m\frac{\partial\Phi_m\Big(r_s,\theta_s\Big)}{\partial r_s}\Big|_{r_s=b}. \tag{B.4}$$

Setting $u_c \equiv \cos\theta_c$ and $u_s \equiv \cos\theta_s$, and combining Eqs. (3.11a-3.12c) and Eqs. (B.1-B.4), we obtain:

$$\sum_{n=1}^{\infty} A_n P_n(u_c) = \sum_{n=1}^{\infty}\Big[B_n\Big(\frac{r_s}{b}\Big)^n + C_n\Big(\frac{b}{r_s}\Big)^{(n+1)}\Big]P_n(u_s)\Big|_{r_c=a}, \tag{B.5}$$

$$\sum_{n=1}^{\infty}[B_n + C_n]P_n(u_s) = \sum_{n=1}^{\infty}[E_n + D_n]P_n(u_s), \tag{B.6}$$

$$\varepsilon_c\sum_{n=1}^{\infty} nA_nP_n(u_c) = a\varepsilon_s(\omega)\sum_{n=1}^{\infty}\frac{\partial}{\partial r_c}\Big[B_n\Big(\frac{r_s}{b}\Big)^n + C_n\Big(\frac{b}{r_s}\Big)^{(n+1)}\Big]P_n(u_s)\Big|_{r_c=a}, \tag{B.7}$$

$$\varepsilon_s(\omega)\sum_{n=1}^{\infty}[nB_n - (n+1)C_n]P_n(u_s) = \varepsilon_m\sum_{n=1}^{\infty}[nE_n - (n+1)D_n]P_n(u_s). \tag{B.8}$$

Multiplying both sides of Eqs. (B.6 & B.8) each by $P_l(u_c)$ and Eqs. (B.5 & B.7) each by $P_l(u_s)$, and integrating each one respectively via

$$\beta_l\int_{-1}^{1} P_l(u)P_n(u)du = \delta_{ln}, \quad \beta_l = l + \frac{1}{2}, \tag{B.9}$$

we obtain

$$A_l = \sum_{n=1}^{\infty} K_{ln}B_n + \sum_{n=1}^{\infty} M_{ln}C_n, \tag{B.10}$$

$$B_l + C_l = E_l + D_l, \tag{B.11}$$

$$\varepsilon_c l A_l = \varepsilon_s(\omega)\Big[\sum_{n=1}^{\infty} L_{ln}B_n + \sum_{n=1}^{\infty} N_{ln}C_n\Big], \tag{B.12}$$

$$\varepsilon_s(\omega)[lB_l - (l+1)C_l] = \varepsilon_m[lE_l - (l+1)D_l], \tag{B.13}$$

where

$$K_{ln} = \frac{\beta_l}{b^n} \int_{-1}^{1} r_s^n P_n(u_s)\Big|_{r_c=a} P_l(u_c) du_c, \tag{B.14}$$

$$M_{ln} = \beta_l b^{n+1} \int_{-1}^{1} \frac{P_n(u_s)}{r_s^{n+1}}\Big|_{r_c=a} P_l(u_c) du_c, \tag{B.15}$$

$$L_{ln} = \frac{\beta_l a}{b^n} \int_{-1}^{1} \frac{\partial}{\partial r_c}\Big[r_s^n P_n(u_s)\Big]_{r_c=a} P_l(u_c) du_c, \tag{B.16}$$

$$N_{ln} = \beta_l a b^{n+1} \int_{-1}^{1} \frac{\partial}{\partial r_c}\left[\frac{P_n(u_s)}{r_s^{n+1}}\right]_{r_c=a} P_l(u_c) du_c. \tag{B.17}$$

In order to evaluate Eqs. (B.14-B.17), we need to make use of the SHAT in spherical coordinates. This theorem allows us to express the integrands in Eqs. (B.14-B.17) in terms of the core coordinates (r_c, u_c) and the core-offset σ. The SHAT theorem states that given two off-centre spherical harmonic coordinates $\mathbf{r}$ and $\mathbf{r}'$, then for $m = 0$[114]

$$R_n(\mathbf{r} + \mathbf{r}') = \sum_{k=0}^{n} \begin{pmatrix} n \\ k \end{pmatrix} R_k(\mathbf{r}) R_{n-k}(\mathbf{r}'), \tag{B.18}$$

$$S_n(\mathbf{r} + \mathbf{r}') = \sum_{k=n}^{\infty} (-1)^{k-n} \begin{pmatrix} k \\ n \end{pmatrix} S_k(\mathbf{r}) R_{k-n}(\mathbf{r}'), \tag{B.19}$$

where $R_n(\mathbf{r})$ and $S_n(\mathbf{r})$ are the interior and exterior solutions of the Laplace equation in spherical coordinates, given as[62,114]

$$R_n(\mathbf{r}) = r^n P_n(u), \tag{B.20}$$

$$S_n(\mathbf{r}) = \frac{1}{r^{n+1}} P_n(u), \tag{B.21}$$

where $\mathbf{r} = (r, u)$ and $u = \cos\theta$. From Fig. 1.1, we have $\mathbf{r}_s = \mathbf{R} + \mathbf{r}_c$, where $\mathbf{r}_s = (r_s, u_s), \mathbf{r}_c = (r_c, u_c)$, and $\mathbf{R} = (\sigma, 1)$, since the core-offset lies along the vertical. Then, setting $\mathbf{r} = \mathbf{r_c}$, and $\mathbf{r}' = \mathbf{R}$ in Eqs. (B.18 & B.19), and making use of Eqs. (B.20 & B.21) and $P_n(1) = 1$, we obtain

$$r_s^n P_n(u_s) = \sum_{k=0}^{n} \begin{pmatrix} n \\ k \end{pmatrix} r_c^k P_k(u_c) \sigma^{n-k}, \tag{B.22}$$

$$\frac{P_n(u_s)}{r_s^{n+1}} = \sum_{k=n}^{\infty} (-1)^{k-n} \begin{pmatrix} k \\ n \end{pmatrix} \frac{1}{r_c^{k+1}} P_k(u_c) \sigma^{k-n}. \tag{B.23}$$

Substituting Eq. (B.22) into Eqs. (B.14 & B.16), and substituting Eq. (B.23) into Eqs. (B.15 & B.17) respectively, leads to

$$L_{ln} = l K_{ln}, \tag{B.24}$$

$$N_{ln} = -(l+1) M_{ln}, \tag{B.25}$$

where K_{ln} and M_{ln} are given in Eq. (3.15). Substituting Eq. (B.24) into Eq. (B.12), and Eq. (B.25) into Eq. (B.12), Eqs. (B.10-B.13) can be re-written as:

$$A_l = \sum_{n=1}^{N} K_{ln} B_n + \sum_{n=1}^{N} M_{ln} C_n, \tag{B.26}$$

$$B_l + C_l = E_l + D_l, \tag{B.27}$$

$$\varepsilon_c l A_l = \varepsilon_s(\omega)\Big[l \sum_{n=1}^{N} K_{ln} B_n - (l+1) \sum_{n=1}^{N} M_{ln} C_n\Big], \tag{B.28}$$

$$\varepsilon_s(\omega)[l B_l - (l+1) C_l] = \varepsilon_m[l E_l - (l+1) D_l], \tag{B.29}$$

where we have truncated the summation to some finite number N.

To obtain the static multipole polarizability of the nanoegg, we need to express the amplitude of the induced potential D_l in terms of the amplitude of the incident potential E_l. Eliminating B_l using Eq. (B.27) and Eq. (B.29), we obtain

$$D_l = -E_l \left[\frac{(2l+1)\varepsilon_s(\omega)\left[\frac{C_l}{-E_l}\right] + l\Big[\varepsilon_s(\omega) - \varepsilon_m\Big]}{l\varepsilon_s(\omega) + (l+1)\varepsilon_m} \right]. \tag{B.30}$$

Next, we eliminate A_l using Eq. (B.26) and Eq. (B.28), to obtain

$$0 = \sum_{n=1}^{N} K_{ln} B_n + \frac{\Big[l\varepsilon_c + (l+1)\varepsilon_s(\omega)\Big]}{l\Big[\varepsilon_c - \varepsilon_s(\omega)\Big]} \sum_{n=1}^{N} M_{ln} C_n. \tag{B.31}$$

Then we eliminate D_l using Eq. (B.27) and Eq. (B.29), to find

$$B_l = \frac{(2l+1)\varepsilon_m E_l + C_l(l+1)\Big[\varepsilon_s(\omega) - \varepsilon_m\Big]}{l\varepsilon_s(\omega) + (l+1)\varepsilon_m}. \tag{B.32}$$

Now we substitute B_l for B_n (by changing l to n) in Eq. (B.31), and rearrange terms to finally obtain Eq. (3.13). Substituting Eq. (B.30) in Eq. (3.12c), and making use of Eq. (3.12b), we obtain Eqs. (3.16 & 3.17).

The induced multipolar field is calculated through $\mathbf{E}_{z,ind}(r_s, \theta_s) = -\nabla\Phi_{z,ind}(r_s, \theta_s)$ as follows:

$$\begin{aligned}\mathbf{E}_{z,ind}(r_s, \theta_s) &= -\frac{\partial\Phi_{ind}}{\partial r_s}\hat{r}_s - \frac{1}{r_s}\frac{\partial\Phi_{ind}}{\partial\theta_s}\hat{\theta}_s \\ = \sum_{n=1}^{\infty} \alpha_n(\omega) &\frac{\mathrm{p}_z(n+1)}{\varepsilon_m r_s^{n+2} r^{n+2}}\Big[(n+1)P_n(\cos\theta_s)\hat{r}_s - \\ &\frac{d}{d\theta_s}\Big[P_n(\cos\theta_s)\Big]\hat{\theta}_s\Big],\end{aligned} \tag{B.33}$$

and using the properties of the Legendre function of the first kind:

$$\frac{P_n(\cos\theta_s)}{\cos\theta_s}\Big|_{\theta_s\to 0} = 1, \quad \frac{d}{d\theta_s}\Big[P_n(\cos\theta_s)\Big]\Big|_{\theta_s\to 0} = 0,$$

we obtain the induced field at the dipole position $r_s = r$ and $\theta_s \to 0$ as

$$\mathbf{E}_{z,ind}(r_s = r, \theta_s \to 0) = \sum_{n=1}^{\infty} \alpha_n(\omega)\frac{\mathrm{p}_z(n+1)^2}{\varepsilon_m r^{2n+4}}\hat{z}, \qquad \hat{z} = \cos\theta_s\hat{r}_s. \tag{B.34}$$

PARALLEL MOLECULAR DIPOLE

Setting $u_c \equiv \cos\theta_c$ and $u_s \equiv \cos\theta_s$, and combining Eqs. (3.21a-3.22c) and Eqs. (B.1-B.4), we obtain:

$$\sum_{n=1}^{\infty} A_n P_n^1(u_c) = \sum_{n=1}^{\infty} \left[B_n \left(\frac{r_s}{b}\right)^n + C_n \left(\frac{b}{r_s}\right)^{(n+1)} \right] P_n^1(u_s)\Big|_{r_c=a}, \quad \text{(B.35)}$$

$$\sum_{n=1}^{\infty} [B_n + C_n] P_n^1(u_s) = \sum_{n=1}^{\infty} [E_n + D_n] P_n^1(u_s), \quad \text{(B.36)}$$

$$\varepsilon_c \sum_{n=1}^{\infty} n A_n P_n^1(u_c) = a\varepsilon_s(\omega) \sum_{n=1}^{\infty} \frac{\partial}{\partial r_c} \left[B_n \left(\frac{r_s}{b}\right)^n + C_n \left(\frac{b}{r_s}\right)^{(n+1)} \right] P_n^1(u_s)\Big|_{r_c=a}, \quad \text{(B.37)}$$

$$\varepsilon_s(\omega) \sum_{n=1}^{\infty} [nB_n - (n+1)C_n] P_n^1(u_s) = \varepsilon_m \sum_{n=1}^{\infty} [nE_n - (n+1)D_n] P_n^1(u_s). \quad \text{(B.38)}$$

Multiplying both sides of Eqs. (B.35 & B.37) each by $P_l^1(u_c)$ and Eqs. (B.36 & B.38) each by $P_l^1(u_s)$, and integrating each one respectively via

$$\rho_l \int_{-1}^{1} P_l^1(u) P_n^1(u) du = \delta_{ln}, \;\; \rho_l = \frac{2l+1}{2l(l+1)}, \quad \text{(B.39)}$$

we obtain

$$A_l = \sum_{n=1}^{\infty} K_{ln} B_n + \sum_{n=1}^{\infty} M_{ln} C_n, \quad \text{(B.40)}$$

$$B_l + C_l = E_l + D_l, \quad \text{(B.41)}$$

$$\varepsilon_c l A_l = \varepsilon_s(\omega) \Big[\sum_{n=1}^{\infty} L_{ln} B_n + \sum_{n=1}^{\infty} N_{ln} C_n \Big], \quad \text{(B.42)}$$

$$\varepsilon_s(\omega)[lB_l - (l+1)C_l] = \varepsilon_m [lE_l - (l+1)D_l], \quad \text{(B.43)}$$

where

$$K_{ln} = \frac{\rho_l}{b^n} \int_{-1}^{1} r_s^n P_n^1(u_s)\Big|_{r_c=a} P_l^1(u_c) du_c, \quad \text{(B.44)}$$

$$M_{ln} = \rho_l b^{n+1} \int_{-1}^{1} \frac{P_n^1(u_s)}{r_s^{n+1}}\Big|_{r_c=a} P_l^1(u_c) du_c, \quad \text{(B.45)}$$

$$L_{ln} = \frac{\rho_l a}{b^n} \int_{-1}^{1} \frac{\partial}{\partial r_c} \Big[r_s^n P_n^1(u_s) \Big]_{r_c=a} P_l^1(u_c) du_c, \quad \text{(B.46)}$$

$$N_{ln} = \rho_l a b^{n+1} \int_{-1}^{1} \frac{\partial}{\partial r_c} \left[\frac{P_n^1(u_s)}{r_s^{n+1}} \right]_{r_c=a} P_l^1(u_c) du_c. \quad \text{(B.47)}$$

Here, we assume that the interior and exterior solutions of the Laplace equation for the parallel dipole also obey the SHAT in a similar manner as that of the perpendicular dipole (although for $m = 1$, the SHAT is slightly different, see Ref.[114]), so that the polarizability of the nanoegg remains the same. Hence, the values of Eqs. (B.44-B.47) are the same as those of the perpendicular case, so that Eqs. (B.30-B.32) and Eqs. (3.13-3.15,3.17) are retained. However, the coefficients E_l are now given by Eq. (3.22b).

Substituting Eq. (B.30) into Eq. (3.22c), making use of Eq. (3.22b), we obtain Eq. (3.23). The induced multipolar field in this case is calculated via $\mathbf{E}_{x,ind}(r_s,\theta_s) = -\nabla\Phi_{x,ind}(r_s,\theta_s)$ as follows

$$\begin{aligned}\mathbf{E}_{x,ind}(r_s,\theta_s) &= -\frac{\partial\Phi_{ind}}{\partial r_s}\hat{r}_s - \frac{1}{r_s}\frac{\partial\Phi_{ind}}{\partial\theta_s}\hat{\theta}_s - \frac{1}{r_s\sin\theta_s}\frac{\partial\Phi_{ind}}{\partial\phi}\hat{\phi}_s \\ &= \sum_{n=1}^{\infty}\alpha_n(\omega)\frac{\mathrm{p}_x}{\varepsilon_m r_s^{n+2} r^{n+2}}\Big[-(n+1)P_n^1(\cos\theta_s)\cos\phi\hat{r}_s \\ &+\frac{d}{d\theta_s}\Big[P_n^1(\cos\theta_s)\Big]\cos\phi\hat{\theta}_s - \frac{P_n^1(\cos\theta_s)}{\sin\theta_s}\sin\phi\hat{\phi}_s\Big], \end{aligned} \tag{B.48}$$

and using the properties of the associated Legendre function of the first kind:

$$P_n^1(\cos\theta_s)\Big|_{\theta_s\to 0} = 0,\ \frac{1}{\cos\theta_s}\frac{d}{d\theta_s}\Big[P_n^1(\cos\theta_s)\Big]\Big|_{\theta_s\to 0} = \frac{n(n+1)}{2},$$
$$\frac{P_n^1(\cos\theta_s)}{\sin\theta_s}\Big|_{\theta_s\to 0} = \frac{n(n+1)}{2},$$

we obtain the induced field at the dipole position $r_s = r$ and $\theta_s \to 0$ as

$$\mathbf{E}_{x,ind}(r_s = r,\theta_s\to 0) = \sum_{n=1}^{\infty}\alpha_n(\omega)\frac{\mathrm{p}_x n(n+1)}{2\varepsilon_m r^{2n+4}}\hat{x},$$
$$\hat{x} = \cos\theta_s\cos\phi\hat{\theta}_s - \sin\phi\hat{\phi}. \tag{B.49}$$

BIBLIOGRAPHY

[1] S. A. Maier. *Plasmonics: fundamentals and applications.* Springer science & Business media, 2007.

[2] G. Barbillon. Plasmonics and its applications. *Materials*, 12:1502, 2019.

[3] S. Raza, S. I. Bozhevolnyi, M. Wubs, and N. A. Mortensen. Nonlocal optical response in metallic nanostructures. *J. Phys. Condens. Matter.*, 27:183204, 2014.

[4] K. D. Sattler. *Handbook of Nanophysics: Nanoparticles and Quantum dots.* CRC Press., 2016.

[5] M. H. Chowdhury, K. Ray, S. K. Grey, J. Pond, and J. R. Lakowicz. Aluminum nanoparticles as substrate for metal-enhanced fluorescence in the ultraviolet for the label-free detection of biomolecules. *Anal. Chem.*, 81:1397–1403, 2009.

[6] M. Notarianni, K. Vernon, A. Chou, M. Aljada, J. Liu, and N. Motta. Plasmonic effect of gold nanoparticles in organic solar cells. *Sol. Energy*, 106:23–37, 2013.

[7] W. L. Barnes. Particle plasmons: Why shape matters. *Am. J. Phys.*, 84:593–601, 2016.

[8] C. F. Bohren and D. R. Huffman. *Absorption and scattering of light by small particles*. John Wiley and Sons, Inc., 2008.

[9] S. Khatua, P. M. R. Paulo, A. Gupta H. Yuan, P. Zijlstra, and M. Orrit. Resonant plasmonic enhancement of single-molecule fluorescence by individual gold nanorods. *ACS Nano*, 8:4440–4449, 2014.

[10] M. Yorulmaz, S. Khatua, P. Zijlstra, A. Gaiduk, and M. Orrit. Luminescence quantum yield of single gold nanorods. *Nano Lett.*, 12:4385–4391, 2012.

[11] F. Kyeyune, J. L. Botha, B. van Heerden, P. Malý, R. van Grondelle, M. Diale, and T. P. J. Kruger. Strong plasmonic fluorescence enhancement of individual plant light-harvesting complexes. *Nanoscale*, 11:15139–15146, 2019.

[12] L. C. Ugwuoke, T. Mančal, and T. P. J. Kruger. Localized surface plasmon resonances of simple tunable plasmonic nanostructures. *Plasmonics*, 15:189–200, 2020.

[13] H. Wang, Y. Wu, B. Lassiter, C. L. Nehl, J. H. Hafner, P. Nordlander, and N. J. Halas. Symmetry breaking in individual plasmonic nanoparticles. *PNAS*, 103:10856–10850, 2006.

[14] Y. Wu and P. Nordlander. Plasmon hybridization in nanoshells with a nonconcentric core. *J. Chem. Phys.*, 12:124708, 2006.

[15] M. W. Knight and N. J. Halas. Nanoshells to nanoeggs to nanocups: optical properties of reduced symmetry core-shell nanoparticles beyond the quasistatic limit. *New J. Phys.*, 10:105006, 2008.

[16] J. Liu, A. I. Maaroof, L. Wieczorek, and M. B. Cortie. Fabrication of hollow metal Nanocaps and their red-shifted optical absorption spectra. *Adv. Mater.*, 17:1276–1281, 2005.

[17] L. Shao, C. Fang, H. Chen, Y. C. Man, J. Wang, and H-Q. Lin. Distinct plasmonic manifestation on gold nanorods induced by the spatial perturbation of small gold nanospheres. *Nano Lett.*, 12:14241430, 2012.

[18] L. V. Brown, H. Sobhani, J. B. Lassiter, P. Nordlander, and Naomi J. Halas. Heterodimers: Plasmonic properties of mismatched nanoparticle pairs. *ACS Nano.*, 4:819–832, 2010.

[19] A. Lombardi, M. P. Grzelczak, A. Crut, P. Maioli, I. Pastoriza-Santos, L. M. Liz-Marzn, N. D. Fatti, and F. Valle. Optical response of individual Au-Ag@SiO_2 heterodimers. *ACS Nano*, 7:2522–2531, 2013.

[20] S. A. Maier, M. L. Brongersma, P. G. Kik, S. Meltzer, A. A. Requicha, and H. A. Atwater. Plasmonics–a route to nanoscale optical devices. *Adv. Mater.*, 15:562–562, 2011.

[21] V. Myroshnychenko, J. Rodrguez-Fernández, I. Pastoriza-Santos, A. M. Funston, C. Novo, P. Mulvaney, and F. J. G. de Abajo. Modelling the optical response of gold nanoparticles. *Chemical Society Reviews*, 37:1792–1805, 2008.

[22] A. Moroz. Depolarization field of spheroidal particles. *J. Opt. Soc. Am. B*, 26:517–527, 2009.

[23] L. J. Sherry, R. Jin, C. A. Mirkin, G. C. Schatz, and R. P. Van Duyne. Localized surface plasmon resonance spectroscopy of single silver triangular nanoprisms. *Nano Lett.*, 6:2060–2065, 2006.

[24] C. L. Nehl, H. Liao, and J. H. Hafner. Optical properties of star-shaped gold nanoparticles. *Nano Lett.*, 6:683–688, 2006.

[25] Q. Wei, G. Acuna, S. Kim, C. Vietz, D. Tseng, J. Chae, D. Shir, W. Luo, P. Tinnefeld, and A. Ozcan. Plasmonics enhanced smartphone fluorescence microscopy. *Sci. Rep.*, 7:2124, 2017.

[26] A. Mohammadi, V. Sandoghdar, and M. Agio. Gold nanorods and nanospheroids for enhancing optical emission. *New J. Phys.*, 10:105015, 2008.

[27] S. L. Smitha, K. G. Gopchandran, N. Smijesh, and R. Philip. Size-dependent optical properties of Au nanorods. *Progress in Natural Science: Materials International*, 23:36–43, 2013.

[28] A. Cacciola, C. Triolo, O. D. Stefano, A. Genco, M. Mazzeo, R. Saija, S. Patan, and S. Savasta. Subdiffraction light concentration by j-aggregate nanostructures. *ACS Photonics*, DOI: 10.1021/acsphotonics.5b00197, 2015.

[29] M. Enders, S. Mukai, T. Uwada, and S. Hashimoto. Plasmonic nanofabrication through optical heating. *J. Phys. Chem. C*, DOI: 10.1021/acs.jpcc.5b11762, 2016.

[30] P. Nordlander, C. Oubre, E. Prodan, K. Li, and M. I. Stockman. Plasmon hybridization in nanoparticle dimers. *Nano Lett.*, 4:899–903, 2004.

[31] M. Staffaroni, J. Conway, S. Vedantam, J. Tang, and E. Yablonovitch. Circuit analysis in metal-optics. *Photonics and Nanostructures - Fundamentals and Applications*, 10:166–176, 2012.

[32] B. Willingham and S. Link. A kirchhoff solution to plasmon hybridization. *Appl. Phys. B - Lasers and Optics*, DOI 10.1007/s00340-013-5501-7, 2013.

[33] D. Zhu, M. Bosman, and J. K. W. Yang. A circuit model for plasmonic resonators. *Optics Express*, 22:9890–9819, 2014.

[34] R. Marty, A. Mlayah, A. Arbouet, C. Girard, and S. Tripathy. Plasphonics: local hybridization of plasmons and phonons. *Optics Express*, 21:4551–4559, 2013.

[35] C. Huck, J. Vogt, T. Neuman, T. Nagao, R. Hillenbrand, J. Aizpurua, A. Pucci, and F. Neubrech. Strong coupling between phonon-polaritons and plasmonic nanorods. *Optics Express*, 24:25528–25539, 2016.

[36] J. B. Herzog, M. W. Knight, and D. Natelson. Thermoplasmonics: Quantifying plasmonic heating in single nanowires. *Nano Lett.*, 14:499–503, 2014.

[37] J. B. Gonzlez-Daz, A. Garca-Martn, J. M. Garca-Martn, A. Cebollada, G. Armelles, B. Sepffllveda, Y. Alaverdyan, and M. Kll. Plasmonic Au/Co/Au nanosandwiches with enhanced magneto-optical activity. *Small*, 4:202–205, 2008.

[38] D. Bossini, V. I. Belotelov, A. K. Zvezdin, A. N. Kalish, and A. V. Kimel. Magnetoplasmonics and femtosecond optomagnetism at the nanoscale. *ACS Photonics*, 3:1385–1400, 2016.

[39] A. J. Wilson and K. A. Willets. Molecular plasmonics. *Annual Review of Analytical Chemistry*, 9:27–43, 2016.

[40] M. Guerrini, A. Calzolari, D. Varsano, and S. Corni. Quantifying the plasmonic character of optical excitations in a molecular j-aggregate. *J. Chem. Theory Comput.*, 15:3197–3203, 2019.

[41] T. J. Antosiewicz, S. P. Apell, and T. Shegai. Plasmon-Exciton interactions in a core-shell geometry: From enhanced absorption to strong coupling. *ACS Photonics*, 1:454–463, 2014.

[42] X. Wu, S. K. Gray, and M. Pelton. Quantum-dot-induced transparency in a nanoscale plasmonic resonator. *Optics Express*, 18:23633–23645, 2010.

[43] C. Tserkezis, M. Wubs, and N. A. Mortensen. Robustness of Rabi splitting under nonlocal corrections in plexcitonics. *ACS Photonics*, 5:133–142, 2018.

[44] S. D. Standridge, G. C. Schatz, and J. T. Hupp. Distance dependence of plasmon-enhanced photocurrent in dye-sensitized solar cells. *J. Am. Chem. Soc.*, 131:8407–8409, 2009.

[45] B. Ding, M. Yang, B. J. Lee, and J. Lee. Tunable surface plasmons of dielectric core-metal shell particles for dye sensitized solar cells. *RSC Advances*, 3:9690–9697, 2013.

[46] Y. Yang, H. B. Gobeze, F. D. Souza, R. Jankowiak, and J. Li. Plasmonic enhancement of biosolar cells employing light-harvesting complex II incorporated with core-shell metal@tio$_2$ nanoparticles. *Adv. Mater. Interfaces*, 3:1600371, 2016.

[47] L. Ferrari, J. S. T. Smalley, H. Qian, A. Tanaka, D. Lu, S. Dayeh, Y. Fainman, and Z. Liu. Design and analysis of blue InGaN/GaN plasmonic LED for high-speed, high-efficiency optical communications. *ACS Photonics*, 5:3557–3564, 2018.

[48] G. Lozano, S. R. K. Rodriguez, M. A. Verschuuren, and J. G. Rivas. Metallic nanostructures for efficient LED lighting. *Light: Science and Applications*, 5:16080, 2016.

[49] N. Muhammad, Z. Ouyang, Z-L. Deng, A. D. Khan, Q. Liu, and X. Tang. Sensitive label-free sensor with high figure of merit based on plasmonic metasurface with unit cell of double two-split nanorings. *J. Mater. Sci.*, 54:6301–6309, 2019.

[50] X. Wu, P. Jiang, G. Razinskas, Y. Huo, H. Zhang, M. Kamp, A. Rastelli, O. G. Schmidt, B. Hecht, K. Lindfors, and M. Lippitz. On-chip single-plasmon nanocircuit driven by a self-assembled quantum dot. *Nano Lett.*, 17:4291–4296, 2017.

[51] U. Kreibig and L. Genzel. Optical absorption of small metal particles. *Surface Science*, 156:678–700, 1985.

[52] J. Gersten and A. Nitzan. Spectroscopic properties of molecules interacting with small dielectric particles. *J. Chem. Phys.*, 75:1139, 1981.

[53] R. Esteban, A. G. Borisov, P. Nordlander, and J. Aizpurua. Bridging quantum and classical plasmonics with a quantum-corrected model. *Nature Communications*, 3:825, 2012.

[54] N. A. Mortensen, S. Raza, M. Wubs, T. Sondergaard, and S. I. Bozhevolnyi. A generalized non-local response theory for plasmonic nanostructures. *Nature Communications*, 5:3809, 2014.

[55] C. Ciraci, R. T. Hill, J. J. Mock, Y. Urzhumov, A. I. Fernández-Domíniguez, S. A. Maier, J. B. Pendry, A. Chilkoti, and D. R. Smith. Probing the ultimate limits of plasmonic enhancement. *Science*, 337:1072–1074, 2012.

[56] J. Zuloaga, E. Prodan, and P. Nordlander. Quantum plasmonics: optical properties and tunability of metallic nanorods. *ACS nano*, 4:5269–5276, 2010.

[57] E. Prodan and P. Nordlander. Structural tunability of the plasmon resonances in metallic nanoshells. *Nano Lett.*, 3:543–547, 2003.

[58] A. Vial, A-S. Grimault, D. Macas, D. Barchiesi, and M. L. Chapelle. Improved analytical fit of gold dispersion: Application to the modeling of extinction spectra with a finite-difference time-domain method. *Phys. Rev.*, 71:085416, 2005.

[59] D. Barchiesi and T. Grosges. Fitting the optical constants of gold, silver, chromium, titanium, and aluminum in the visible bandwidth. *Journal of Nanophotonics*, 8:083097, 2014.

[60] R. Bardhan, N. K. Grady, J. R. Cole, A. Joshi, and N. J. Halas. Fluorescence enhancement by Au nanostructures: nanoshells and nanorods. *ACS Nano*, 3:744–752, 2009.

[61] K. L. Kelly, E. Coronado, L. L. Zhao, and G. C. Schatz. The optical properties of metal nanoparticles: the influence of size, shape, and dielectric environment. *J. Phys. Chem. B*, 107:668–677, 2003.

[62] G. W. Ford and W. H. Weber. Electromagnetic interactions of molecules with metal surfaces. *Phys. Rep.*, 113:195–287, 1984.

[63] A. R. Gazizov, S. S. Kharintsev, and M. K. Salakhov. Longitudinal polarizability and enhancement factor of a tapered optical gold nanoantenna. *J. Phys.: Conf. Ser.*, 714:012011, 2016.

[64] E. Prodan and P. Nordlander. Plasmon hybridization in spherical nanoparticles. *J. Chem. Phys.*, 120:5444–5454, 2004.

[65] A. Aubry, D. Y. Lei, S. A. Maier, and J. B. Pendry. Conformal transformation applied to plasmonics beyond the quasistatic limit. *Phys. Rev. B*, 82:205109, 2010.

[66] J. Zhang and A. Zayats. Multiple Fano resonances in single-layer nonconcentric core-shell nanostructures. *Optics Express*, 21:8426–8436, 2013.

[67] H. Mertens and A. Polman. Strong luminescence quantum-efficiency enhancement near prolate metal nanoparticles: Dipolar versus higher-order modes. *J. Appl. Phys.*, 105:044302, 2009.

[68] H. T. M. C. M. Baltar, K. Drozdowicz-Tomsia, and E. M. Goldys. Propagating surface plasmons and dispersion relations for nanoscale multilayer metallic-dielectric films. *InTech Open Science*, http://dx.doi.org/10.5772/51218:135–156, 2012.

[69] H. Wang, D. W. Brandl, F. Le, P. Nordlander, and N. J. Halas. Nanorice: A hybrid plasmonic nanostructure. *Nano Lett.*, 6:827–832, 2006.

[70] F. P. Schmidt, H. Ditlbacher, U. Hohenester, A. Hohenau, F. Hofer, and J. R. Krenn. Dark plasmonic breathing modes in silver nanodisks. *Nano Lett.*, 12:5780–5783, 2012.

[71] S. J. Norton and T. Vo-Dinh. Optical Fano resonances in a nonconcentric nanoshell. *Appl. Opt.*, 10:2611–2618, 2016.

[72] N. Kalyaniwalla, J. W. Haus, R. Inguva, and M. H. Birnboim. Intrinsic optical bistability for coated spheroidal particles. *Phys. Rev. A*, 42:5613, 1990.

[73] B. K. P. Scaife. The dielectric spheroid revisited. *J. Mol. Struct.*, 479:285–297, 1999.

[74] H. Y. Chung, P. T. Leung, and D. P. Tai. Dynamic modifications of polarizability of large metallic spheroidal nanoshells. *J. Chem. Phys.*, 131:124122, 2009.

[75] P. Pramod and K. G. Thomas. Plasmon coupling in dimers of Au nanorods. *Adv. Mater.*, 20:4300–4305, 2008.

[76] S. Campione, L. K. Warne, and L. I. Basilio. Dipole approximation to predict the resonances of dimers composed of dielectric resonators for directional emission. *Radio Science*, 52:1235–1241, 2017.

[77] M-T. Cheng, S-D. Liu, H-J. Zhou, Z-H. Hao, and Q-Q. Wang. Coherent exciton-plasmon interaction in the hybrid semiconductor quantum dot and metal nanoparticle complex. *Optics Letters*, 32:2125–2127, 2007.

[78] B. Khlebtsov, A. Melnikov, V. Zharov, and N. Khlebtsov. Absorption and scattering of light by a dimer of metal nanospheres: comparison of dipole and multipole approaches. *Nanotechnology*, 17:1437–1445, 2006.

[79] I. Romero, J. Aizpurua, G. W. Bryant, and F. J. Garca de Abajo. Plasmons in nearly touching metallic nanoparticles: singular response in the limit of touching dimers. *Optics Express*, 14:9988–9999, 2006.

[80] T. J. Davis, D. E. Gómez, and K. C. Vernon. Simple model for the hybridization of surface plasmon resonances in metallic nanoparticles. *Nano Letters*, 10:2618–2625, 2010.

[81] P. K. Jain, S. Eustis, and M. A. El-Sayed. Plasmon coupling in nanorod assemblies: Optical absorption, discrete dipole approximation simulation, and exciton-coupling model. *J. Phys. Chem. B*, 110:18243–18253, 2006.

[82] C. G. Khoury, S. J. Norton, and T. Vo-Dinh. Plasmonics of 3-d nanoshell dimers using multipole expansion and finite element method. *Nano Letters*, 3:2776–2788, 2009.

[83] J.-W. Liaw, J.-H. Cheng, C.-S. Chen, and M.-K. Kuo. Purcell effect of nanoshell dimer on single molecule's fluorescence. *Optics Express*, 17:13532, 2009.

[84] Y-F. C. Chau, J-C. Jiang, C-T. C. Chao, H-P. Chiang, and C. M. Lim. Manipulating near field enhancement and optical spectrum in a pair-array of the cavity resonance based plasmonic nanoantennas. *J. Phys. D: Appl. Phys.*, 49:475102, 2016.

[85] A. Moradi. Plasmon hybridization in parallel nano-wire systems. *Physics of Plasmas*, 18:064508, 2011.

[86] I. Kaminska, J. Bohlen, S. Mackowski, P. Tinnefeld, and G. P. Acuna. Strong plasmonic enhancement of a single peridinin-chlorophyll a-protein complex on DNA origami-based optical antennas. *ACS Nano*, 12:1650–1655, 2018.

[87] L. Xin, M. Lu, S. Both, M. Pfeiffer, M. J. Urban, C. Zhou, H. Yan, T. Weiss, N. Liu, and K. Lindfors. Watching a single a fluorophore molecule walk into a plasmonic hotspot. *ACS Photonics*, 6:985–993, 2019.

[88] J.-L. Wu, F.-C. Chen, Y.-S. Hsiao, F.-C. Chien, P. Chen, C.-H. Kuo, M. H. Huang, and C.-S. Hsu. Surface plasmonic effects of metallic nanoparticles on the performance of polymer bulk heterojunction solar cells. *ACS Nano*, 5:959–967, 2011.

[89] V. Krivenkov, S. Goncharov, I. Nabiev, and Y. P. Rakovich. Induced transparency in plasmon-exciton nanostructures for sensing applications. *Laser Photonics Rev.*, 13:1800176, 2019.

[90] L. C. Ugwuoke, T. Mančal, and T. P. J. Kruger. Optical properties of a nanoegg-nanorod heterodimer: a quasi-static analysis. *J. Opt. Soc. Am. B*, 37:A293–A303, 2020.

[91] S. Link and M. A. El-Sayed. Shape and size dependence of radiative, nonradiative and photothermal properties of gold nanocrystals. *Int. Reviews in Physical Chemistry*, 19:409–453, 2000.

[92] L. C. Ugwuoke, T. Mančal, and T. P. J. Kruger. Plasmonic quantum yield enhancement of a single molecule near a nanoegg. *J. Appl. Phys.*, 127:203103, 2020.

[93] L. Novotny. Strong coupling, energy splitting, and level crossings: A classical perspective. *Am. J. Phys.*, 78:1199–1202, 2010.

[94] N. Liu, L. Langguth, T. Weiss, J. Kstel, M. Fleischhauer, T. Pfau, and H. Giessen. Plasmonic analogue of electromagnetically induced transparency at the Drude damping limit. *Nat. Mater.*, 8:158–762, 2009.

[95] R. R. Chance, A. Prock, and R. Silby. Molecular fluorescence and energy transfer near interfaces. *Adv. Chem. Phys.*, 37:1–65, 1978.

[96] R. Ruppin. Decay of an excited molecule near a small metal sphere. *J. Chem. Phys.*, 76:1681, 1982.

[97] C. D. Geddes and J. R. Lakowickz. Metal-enhanced fluorescence. *J. Fluoresc.*, 12:121129, 2002.

[98] P. Anger, P. Bharadwaj, and L. Novotny. Enhancement and quenching of single molecule fluorescence. *Phys. Rev. Lett.*, 96:113002, 2006.

[99] P. Bharadwaj and L. Novotny. Spectral dependence of single molecule fluorescence enhancement. *Optics Express*, 15:14266–14274, 2007.

[100] H. Mertens, A. F. Koenderink, and A. Polman. Plasmon-enhanced luminescence near noble-metal nanospheres: Comparison of exact theory and an improved Gersten and Nitzan model. *Phys. Rev. B*, 76:115123, 2007.

[101] E. Wientjes, J. Renger, A. G. Curto, R. Cogdell, and N. F. van Hulst. Strong antenna-enhanced fluorescence of a single light-harvesting complex shows photon antibunching. *Nat. Commun.*, 5:4236, 2014.

[102] M. Thomas, J.-J. Greffet, R. Carminati, and J. R. Arias-Gonzalez. Single-molecule spontaneous emission close to absorbing nanostructures. *J. Appl. Phys.*, 85:3863–3865, 2004.

[103] S. Mackowski, S. Wormke, A. J. Maier, T. H. P. Brotosudarmo, H. Harutyunyan, A. Hartschuh, A. O. Govorov, H. Scheer, and C. Brauchle. Metal-enhanced fluorescence of chlorophylls in single light-harvesting complexes. *Nano Lett.*, 8:558–564, 2008.

[104] C. Tserkezis, N. Stefanou, M. Wubs, and N. A. Mortensen. Molecular fluorescence enhancement in plasmonic environments: exploring the role of non-local effects. *Nanoscale*, 8:17532–17541, 2016.

[105] Y. Fu, J. Zhang, and J. R. Lakowicz. Large enhancement of single molecule fluorescence by coupling to hollow silver nanoshells. *Chem. Commun.*, 48:9726–9728, 2012.

[106] O. L. Muskens, V. Giannini, J. A. Sanchez-Gil, and J. Gómez Rivas. Strong enhancement of the radiative decay rate of emitters by single plasmonic nanoantennas. *Nano Lett.*, 7:2871–2875, 2007.

[107] A. M. Kern, A. J. Meixner, and O. J. F. Martin. Molecule-dependent plasmonic enhancement of fluorescence and Raman scattering near realistic nanostructures. *ACS Nano*, 6:9828–9836, 2012.

[108] L. Bujak, M. Olejnik, T. H. P. Brotosudarmo, M. K. Schmidt, N. Czechowski, D. Piatkowski, J. Aizpurua, R. J. Cogdell, W. Heiss, and S. Mackowski. Polarization control of metal-enhanced fluorescence in hybrid assemblies of photosynthetic complexes and gold nanorods. *Phys. Chem. Chem. Phys.*, 16:9015, 2014.

[109] Y. Fu, J. Zhang, and J. R. Lakowicz. Plasmonic enhancement of single-molecule fluorescence near a silver nanoparticle. *J. Fluoresc.*, 17:811–816, 2007.

[110] A. Moroz. Superconvergent representation of the Gersten-Nitzan and Ford-Weber nonradiative rates. *J. Phys. Chem. C*, 115:19546–19556, 2011.

[111] D. V. Guzatov, S. V. Vaschenko, V. V. Stankevich, A. Y. Lunevich, Y. F. Glukhov, and S. V. Gaponenko. Plasmonic enhancement of molecular fluorescence near silver nanoparticles: theory, modelling, and experiment. *J. Chem. Phys.*, 116:10723–10733, 2012.

[112] G. Sun, J. B. Khurgin, and C. C. Yang. Impact of high-order surface plasmon modes of metal nanoparticles on enhancement of optical emission. *Appl. Phys. Lett.*, 95:171103, 2009.

[113] M. R. A. Majić, B. Auguié, and E. C. Le Ru. Spheroidal harmonic expansion for the solution of Laplace's equation for a point source near a sphere. *Phys. Rev. E*, 95:033307, 2017.

[114] M. J. Caola. Solid harmonics and their addition theorems. *J. Phys. A: Math. Gen.*, 11:L23–L26, 1978.

[115] R. Bardhan, N. K. Grady, and N. J. Halas. Nanoscale control of near-infrared fluorescence enhancement using Au nanoshells. *Small*, 4:1716–1722, 2008.

[116] N. T. Fofang, T-H. Park, Oara Neumann, N. A. Mirin, P. Nordlander, and N. J. Halas. Plexcitonic nanoparticles: plasmon–exciton coupling in nanoshell–J-aggregate complexes. *Nano. Lett.*, 8:3481–3487, 2008.

[117] A. Tsargorodska, M. L. Cartron, C. Vasilev, G. Kodali, O. A. Mass, J. J. Baumberg, P. L. Dutton, C. N. Hunter, P. Torma, and G. J. Leggett. Strong coupling of localized surface plasmons to excitons in light-harvesting complexes. *Nano. Lett.*, 16:6850–6856, 2016.

[118] A. Trúgler and U. Hohenester. Strong coupling between a metallic nanoparticle and a single molecule. *Phys. Rev. B*, 77:115403, 2008.

[119] G. Zengin, G. Johannson, T. J. Antosiewicz, M. Káll, and T. Shegai. Approaching the strong coupling limit in single plasmonic nanorods interating with J-aggregates. *Scientific Reports*, 3:3074, 2013.

[120] C. D. P. Duffy, A. V. Ruban, and W. Barford. Theoretical investigation of the role of strongly coupled chlorophyll dimers in photoprotection of LHCII. *J. Phys. Chem. B*, 112:12508–12515, 2008.